NOVEL TECHNIQUES FOR FRACTURE MONITORING IN CRYSTALLINE ROCK

BY

GABRIEL MISHAAN LILIENTHAL

THESIS

Submitted in partial fulfillment of the requirements
for the degree of Master of Science in Civil Engineering
in the Graduate College of the
University of Illinois at Urbana-Champaign, 2019

Urbana, Illinois

Adviser:

Assistant Professor Roman Y. Makhnenko

ABSTRACT

The study of fracture is necessary in geotechnical engineering for the safe design of structures and application of engineering principles. Fracture plays a significant role in the behavior of rock and structures during failure. Often times, fracture processes observed in the laboratory do not accurately represent what occurs in the field due to the effect that specimen size and loading conditions have on fracture properties, namely, fracture toughness and the size of the fracture process zone. The fracture toughness increases with specimen size until it reaches a limiting value when the material is large enough to exhibit brittle behavior. In a similar manner, the size of the fracture process zone is observed to grow with specimen size until a limiting value is reached for a large enough specimen. In this study, experiments were performed on granitic specimens of different sizes and under two different loading conditions, three-point and four-point bending. Digital Image Correlation (DIC) was used to identify and calculate the dimensions of the fracture process zone. The study of fracture and fracture processes in granitic specimens through DIC is challenging due to the extremely small displacements, in the order of microns, that are associated with fracture in granite. The results from experiments performed on Adelaide Black granite under three-point bending are compared to data obtained using acoustic emission on the same rock and were shown to be in good agreement. It was observed that in Charcoal granite specimens of sizes that that are typically used in the laboratory, the fracture process zone is larger under four-point bending compared to three-point bending conditions. However, it is predicted that for a large enough specimen, the dimensions of the fracture process zone are similar for both loading conditions. In addition, in the appendix, the use of ultrasonic measurements to study and determine the geometry of a propagating hydraulic fracture in granite is described.

TABLE OF CONTENTS

CHAPTER 1: INTRODUCTION

The study of fracture and fracture propagation in geomaterials is crucial for design and safe application of engineering principles in geotechnical and geological design. Fracture processes have a significant influence on the overall behavior of rock. Quasibrittle materials such as concrete and rock contain naturally occurring structural defects such as preexisting cracks, pores, and inherent imperfections throughout the solid matrix that act as points of stress concentration and potential points of fracture initiation (Ingraffea 1987, Bazant and Planas 1998).

An important challenge in the study of fracture processes in geomaterials is the observed dependence of fracture properties on specimen size, which has resulted in numerous studies (Bazant and Kazemi 1990, Labuz and Biolzi 1998, Bazant and Planas 1998). The behavior of rock during fracturing processes observed in the laboratory is significantly different of what takes place in the field. This phenomenon is a result of the effect of specimen size on fracture in quasibrittle materials such as rock (Le et al. 2011). The size effect causes important parameters such as the fracture toughness, the size of the fracture process zone, and the fracture energy determined in the laboratory to be smaller than those that are observed on the field scale (Bazant and Planas 1998). As a result, parameters obtained experimentally may not be an accurate indicator of the real mechanical response of structures in the field.

The fracture process zone is a localized damage zone that precedes fracture propagation and influences the overall strength and stability of the rock structure. In the fracture process zone, micro-cracking and energy dissipation take place, and as the load increases, the microcracks coalesce into a fracture (Horri and Nemat-Nasser 1986). The fracture process zone plays an important role in the size effect observed in quasibrittle materials. The properties of the fracture

process zone are dependent on the size of the specimen or structure (Bazant and Planas 1998, Biolzi et al. 2011). The assumptions of classical linear elastic fracture mechanics (LEFM) are considered valid only when the size of the fracture process zone is negligible compared to the specimen size. In other words, when the energy dissipation in the process zone is negligible compared to the total dissipated energy, the non-linear processes can be disregarded (Ouchterlony 1990, Matsuki et al. 1991, Kuruppu et al. 2014, Wegs et al. 2015). When the size of the fracture process zone is small compared to the specimen size, the specimen behaves more closely to the LEFM prediction, in the limiting case as the fracture process zone size can be neglected, the material behavior is according to what is predicted by LEFM (Bazant and Planas 1998, Parisio et al. 2019).

The most dominant factors responsible for causing variation in the properties of the fracture process zone are the geometry of the specimen (Zietlow and Labuz 1998, Otsuka and Date 2000, Tarokh et al. 2017) and grain size (Barton 1982, Brook et al 2012, Tarokh and Fakhimi 2014). The width of the process zone is observed to be strongly affected by the grain or aggregate size (Mihashi et al. 1991, Wang et al. 1990). The length of the fracture process zone is heavily influenced by the geometric proportions of the specimen (Wu et al. 2011). Figure 1.1 shows a schematic representation of the fracture process zone and its dimensions.

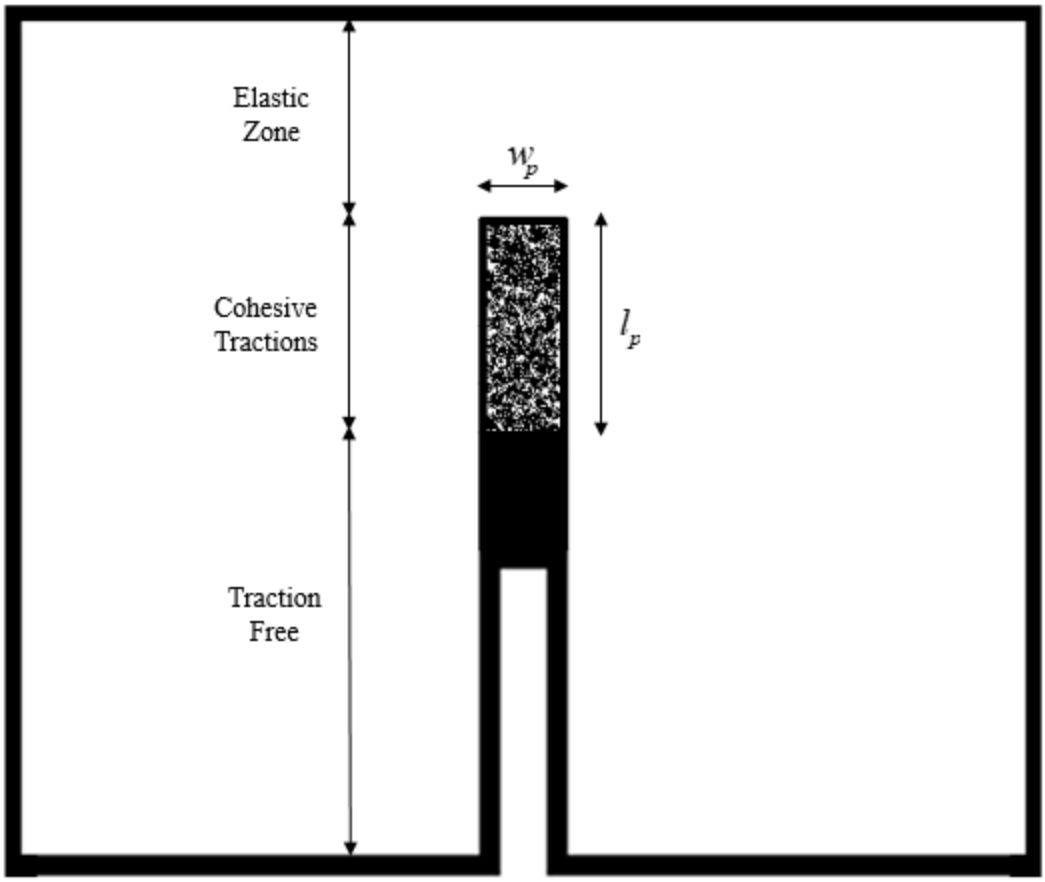

Figure 1.1: Schematic representation of the fracture process zone near the fracture tip and its dimensions.

Zietlow and Labuz (1998) tested different rock types with different grain sizes and found that the width of the process zone increases as grain size increases. Otsuka and Date (2000) reported that the size of the process zone to increases with grain size and that in experiments performed with materials with identical aggregate size, the size of the fracture process zone increased with specimen size as well. Hu and Duan (2004) also observed that the size of the fracture process zone is dependent on the grain size and concluded that the reason for this is that bigger grains increase the tortuosity of the crack, thus increasing the width of the process zone as

well. Zhang and Wu (1999) observed that the fracture process zone length increased along with specimen size.

Other fracture properties such as fracture toughness have been observed to be dependent on the specimen size and geometry as well (Bazant and Planas 1998). The fracture toughness describes the ability of a material to resist fracture and is of great importance in design applications and understanding the behavior of rock masses and structures. There have been contradicting observations in an ongoing debate of whether the fracture toughness of quasibrittle materials is a material property or if it is dependent on specimen size. Peng and Johnson (1972) measured the fracture toughness of Chelmsford granite and Schmidt and Luts (1979) of Westerly granite, both studies indicated constant values for the fracture toughness regardless of size, leading them to the conclusion that the fracture toughness is a material property. Kobayashi et al. (1986) tested specimens of Ogino tuff with different widths and reported the fracture toughness to be independent of specimen width. Schmidt (1976) performed three-point bending tests on sandstones and found that the fracture toughness increases with size until it reached a limiting value for very large specimen sizes. He argued that the specimen's behavior deviated from linear elastic fracture mechanics due to the presence of the fracture process zone. Shylapobersky (1985) observed that the pressure needed for an hydraulic fracture to propagate in the field was much higher than that predicted by LEFM using laboratory results. Li (1986) and Chong and Einstein (1989) observed a size dependence on the fracture toughness and stated that to directly obtain realistic field values from laboratory experiments, impractically large specimens would be needed. They observed that the fracture toughness increases with specimen size until a limiting value is reached. Higgins and Bailey (1976) concluded that the assumptions of linear elastic fracture mechanics are valid only

for specimen sizes beyond a certain critical size, thus the fracture toughness calculated for smaller specimens is not the true fracture toughness but the apparent fracture toughness.

Bazant and Planas (1998) provide a comprehensive guide of size effect in quasibrittle materials; they explain that the most important source of size effect is related to the release of stored energy into the fractured front. Bazant's size effect law (Bazant and Planas 1998) captures the size dependent behavior of quasibrittle materials such as rock and concrete.

Different Methods to Identify Fracture and Fracture Properties

Different experimental techniques have been used to study fracture processes and their dependence on the specimen size and geometry yielding promising results in quasibrittle materials such as concrete and rock. These methods include acoustic emission (Lockner & Byerlee 1977, Stewart 1992, Ishida 2001, Miyahsi et al. 1991), laser speckle interferometry (Wang et al. 1991), environmental scanning electron microscopy (Brooks et al. 2013), X-ray micro-computed tomography (Skarynski and Tejchman 2016), electronic speckle pattern interferometry (ESPI) (Haggerty et. al. 2010) and others. In this study, the use of Digital Image Correlation (DIC) and ultrasonic measurements (see appendix) will be discussed.

DIC belongs to the family of image tracking techniques; these are different techniques that use digital images to track motion and displacements. Image tracking techniques share the following characteristics: the use of digital images, the capability of calculating displacement or/and velocity in a large number of points simultaneously, and high resolution results (Sutton 2009).

Different image tracking techniques such as holographic interferometry, speckle photography, laser speckle interferometry, and electronic speckle pattern interferometry (ESPI)

were developed on the principle of using the phenomenon of laser speckles. These techniques were used as the base for the development of DIC. The origin of these this techniques comes from Rigden and Gordon (1962) and Langmiur (1963) observing laser speckles or interference fringes when a laser was reflected from a relatively smooth surface. The source of this random pattern was attributed to irregularities and randomness in the reflecting surface, and it was possible to extract important information from of the specimen using these speckles. Collier et al. (1965) and Powell and Stetsin (1965) introduced Holographic Interferometry, where the light scattered before and after the object deformation is superposed and the phase change in the scattered light is detected and used to report the deformation. For these methods, the recorded data in photographs implied an inherent difficulty in locating interference fringes with high accuracy, so instead the center of the fringes for only a few points were calculated (Sutton 2009).

The high computational cost and experimental difficulty of processing data from photographs motivated the development of digital imaging technology. New imaging methods were developed that could record the data digitally and automate the data extraction process using algorithms. Peters and Ranson (1982) proposed a computer based image acquisition to measure deformations. Sutton et al. (1983) showed the feasibility of DIC by developing numerical algorithms and performing experiments using optically recorded images. Chu et al. (1985) measured planar translations and rotations using DIC. Sutton et al. (1986) showed that with DIC, displacement measurements could be calculated at a sub-pixel accuracy. With the continuous evolution of digital imaging technology and more efficient algorithms, DIC continued to be developed and became a more widely used tool.

As DIC has become more widespread, its popularity in geotechnical engineering has increased. Rechenmacher and Finno (2003) used DIC in the evaluation of shear bands in dilative

sands. Liu and Iskander (2004) used DIC to calculate soil deformation beneath footings. Bhandari and Inoue (2005) and Kodaka et al. (2007) analyzed strain localization in artificial rock and clays. Zhang et al. (2012) and Arshad and Salgado (2017) studied the failure mechanism of sandstones under indentation and geosynthetics using DIC. Stainer et al. (2016) discusses how improvements in DIC make it an attractive choice for monitoring in different applications in geotechnical engineering.

Research in fracture mechanics using DIC has been ongoing since the 1980s. McNeill et al. (1989) estimated stress intensity factors using DIC. It has also been used to measure the crack opening displacement (Dawick and Sutton 1994 and Sutton 1999). Roux (2006) used DIC to locate the tip of a propagating fracture. Lin and Labuz (2013) and Lin et al. (2019) utilized DIC to locate the fracture tip and to calculate the length of the fracture process zone in sandstone. Einstein (2013) utilized DIC to observe the fracture process zone in Barre granite. Wu et al. (2011) and Alam et al. (2015) used DIC to study the properties of the fracture process zone in concrete.

Study of Fracture Processes in Granite

Granite is the most abundant intrusive igneous rock in the continental crust, which makes it relevant in a wide range of applications and it has been widely studied for this reason (Lockner et al. 1991, Wantanabe et al. 2017, Parisio et al. 2019). Fracture is a critical component in the behavior of granite; fracture systems in granite are responsible for enhancing mass and energy transport properties since the permeability in fractures and fracture systems is notably higher than in the rock matrix (Watanabe 2017). The propensity of granite towards fracture initiation and propagation plays a deterministic role in its physical behavior. As a result, understanding fracture

processes is of outmost importance when attempting to study the structural integrity and behavior of granite.

In some applications it necessary to induce or promote fracture propagation. These applications include petroleum exploration (Lecampion and Desroches 2015), hard rock excavation (Young 1999), quarrying (Pollard and Holzhazhuaen 1979), controlled generation of goafing events in mines (Jeffrey and Mills 2000), environmental remediation (Murdoch 2002), and enhanced geothermal systems (Barbier 2002). In contrast, in some applications, it is necessary to avoid fracture or minimize the conditions that lead to it. These include applications where granite formations serve as barriers for nuclear waste storage (McCathy et al. 1978) and geological carbon sequestration (Metz et al. 2015). In addition, Vilarrasa and Carrera (2015) show that crystalline basements such as granite formations are often times critically stressed, therefore induced seismicity events are commonly originated in these formations, and their fracture properties need to be studied.

Objectives

The main objective of this work is to study the fracture properties of granite through the use of Digital Image Correlation. Detecting and studying fracture in granite with DIC is a challenging task due to the extremely small displacements (order of microns) that the material experiences during fracturing, meaning that high resolution imaging is needed. The achievement of the objective is done through the following steps:

- The design and preparation of an experimental system to study fracture propagation in specimens of different geometries and in varying loading conditions.
- Detection of the propagating fracture and the fracture process zone in granite using Digital Image Correlation.

- Study of the effect of dimensions of the granite specimen on the size of the fracture process zone and the fracture toughness.
- Study of the effect of loading conditions (three versus four-point bending) on the size of the fracture process zone and the fracture toughness.
- Characterization of the geometry of a propagating hydraulic fractures in granite using ultrasonic wave measurements (shown in Appendix).

CHAPTER 2: THEORETICAL BACKGROUND

Linear Elastic Fracture Mechanics

The study of fracture and fracture processes and propagation is crucial in understanding the mechanical behavior of materials and their response at failure. The foundation for the field of Linear Elastic Fracture Mechanics (LEFM) was established by the pioneering work of Inglis (1913) and Griffith (1921). Inglis analyzed the state of stress at the tip of an elliptical hole in an infinite solid, and observed that as the elliptical hole got thinner, or more resembling of a crack, the stress concentration at the tip became more significant. Griffith (1921) expanded on Inglis' work by describing crack growth in brittle materials (glass) by providing a mathematical formulation based on stress analysis and energy balance. Griffith introduced the concept of energy balance: a crack will propagate when the energy required to extend the unit area of the crack is equal to the available energy. This threshold energy value for fracture propagation became known as the specific fracture energy G_f.

Irwin (1957) expanded on previous work and introduced the concept of the stress intensity factor, known as K_I, in order to quantify the stress field near the crack tip. The propagation of a crack begins when the stress intensity factor reaches a critical value, K_{IC} – referred to as the fracture toughness of a material. The fracture toughness is the critical stress intensity factor under Mode I, or tensile fracture. The fracture toughness and specific fracture energy were needed as more appropriate methods to predict failure because strength could not be used as a criterion for failure when a sharp crack is present in an elastic continuum as it is done in the absence of a crack. Griffith also introduced a relationship between the fracture toughness and the specific fracture energy.

$$G_f = \frac{K_{IC}^2}{E'} \tag{2.1}$$

Where E is the material's Young's modulus and $E'=E$ for plane stress and $E'=E/(1-\nu)^2$ for plane strain conditions.

Non-Linear Fracture Mechanics

Linear elastic fracture mechanics predicts that the stress tends to infinity on the fracture tip. Since this is not physically possible, it follows that there must be an inelastic region present near the crack tip where energy is dissipated. This region is assumed negligible in LEFM and is known as the fracture process zone and plays an important role in the size dependent behavior of fracture. When the fracture process zone is small enough compared to the specimen size, the behavior of the specimen can be predicted by LEFM. However, often times the facture process zone cannot be neglected and it has a significant influence on the strength and stability of the specimen or structure.

In quasibrittle materials such as rock and concrete, for specimens in the size range that is generally used in laboratory experiments, the size of the process zone is significant compared to the specimen size and thus cannot be neglected. A consequence of this is that results obtained in the laboratory will vary from those in the field if size effect is not taken into account.

When the size of the fracture process zone is not negligible relative to the dimensions of the specimen the problem becomes non-linear. Irwin (1961) linearized the problem of a non-linear zone by introducing a plastic zone correction, which came to be known as the equivalent crack model. This correction is performed through the assumption of equilibrium by a constant stress redistribution ahead of the crack tip. The length of the plastic zone, r_p, is estimated through Equation 2.2 and illustrated in Figure 2.1:

$$r_p = \frac{\eta + 1}{\pi} \cdot \left(\frac{K_{IC}}{f_t'} \right)^2 \tag{2.2}$$

where f'_t is the tensile strength of the material and η is a dimensionless empirical constant. While the assumption of a constant stress redistribution ahead of the crack tip is reasonable for a ductile material, it is not valid in the case of quasibrittle materials such as rock.

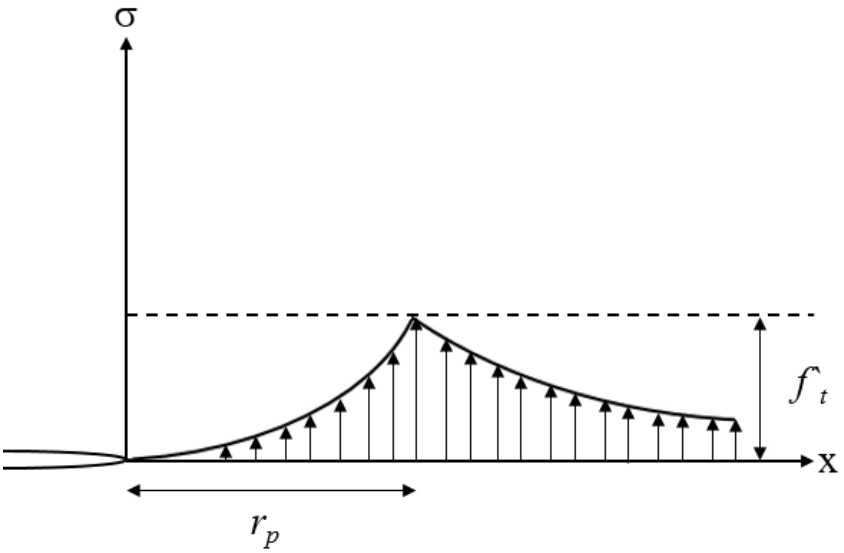

Figure 2.1: Length of the plastic zone in the equivalent crack model (adopted form Bazant and Planas 1998)

Non-Linear Fracture Mechanics in Quasibrittle Materials

Quasibrittle materials such as rock and concrete exhibit significant micro-cracking prior to fracture initiation. As the load and displacement increase, the intensity and frequency of the micro-cracks increases and it is observed that microcracks localize around the fracture tip in what is known as the fracture process zone. Eventually, the microcracks coalesce leading to the initiation of a fracture. Figure 2.2 shows the localization of acoustic emission (AE) events near the fracture tip in an experiment prior to fracture propagation in sandstone tested under three-point bending

loading conditions (Labuz and Biolzi 1997). The damage is localized in the fracture process zone and the fracture process zone precedes fracture propagation.

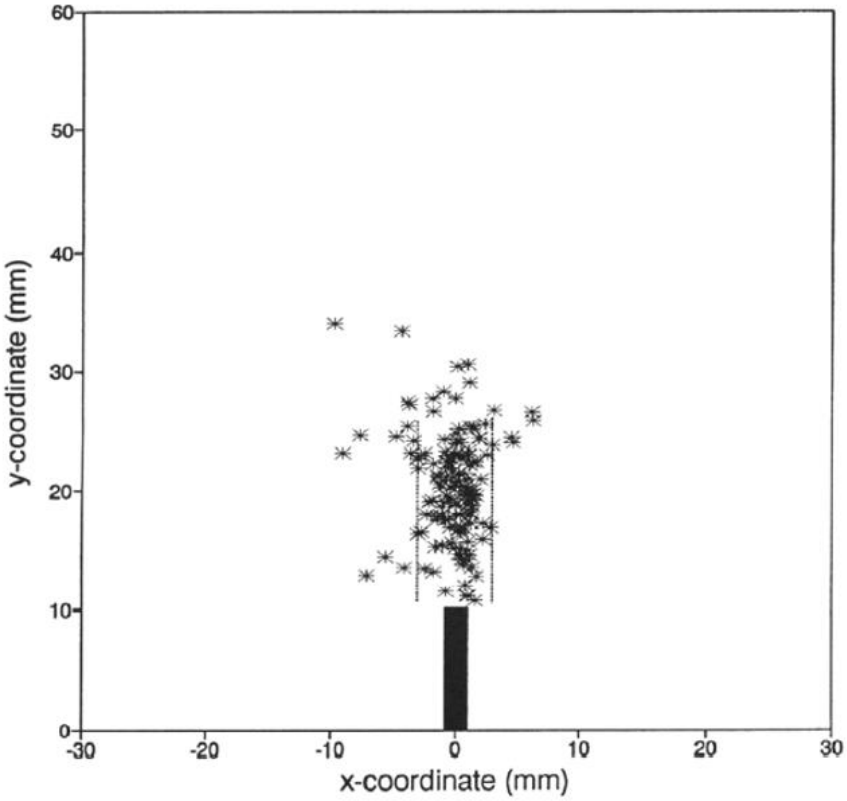

Figure 2.2: Localization of Acoustic Emission events in the fracture process zone before fracture propagation in sandstone under three-point bending (Labuz and Biolzi 1997).

The fracture process zone is characterized by processes such as micro-cracking, void formation, and interface breakage. While the fracture is traction free, the process zone retains some traction due to unbroken bonds and ligaments. The fracture process zone is modeled as a cohesive zone (Elices et al. 2002). Figure 2.3 shows a schematic representation of the fracture and the fracture process zone.

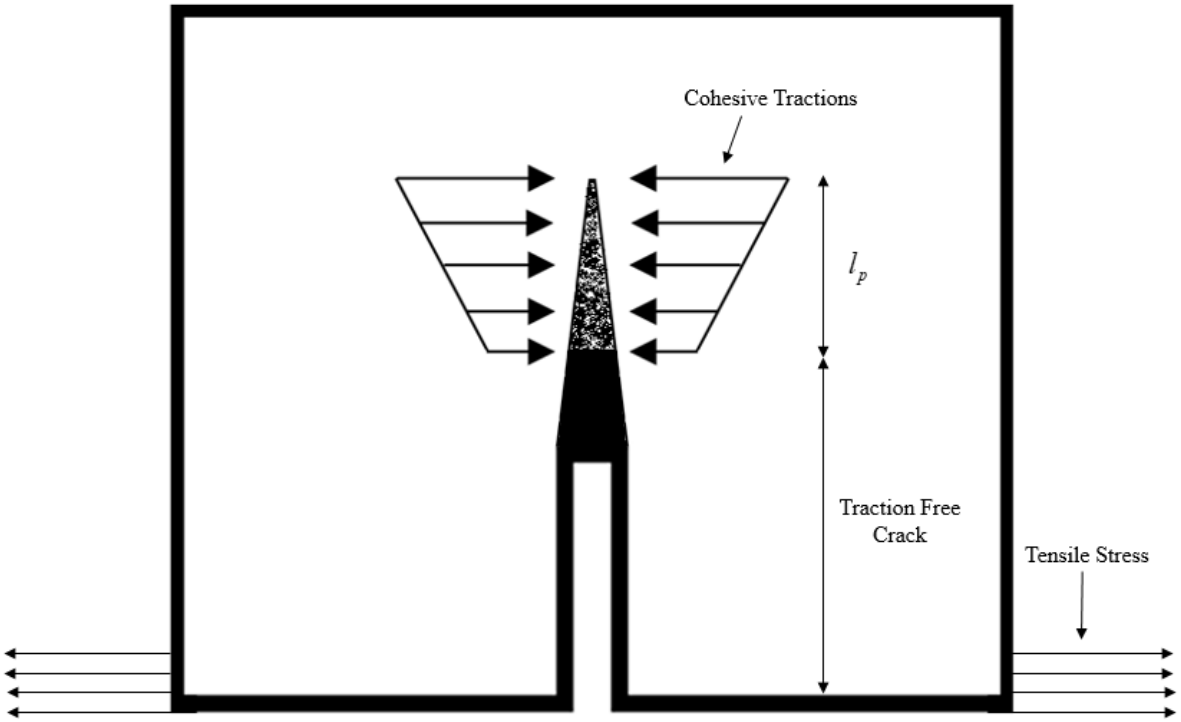

Figure 2.3: Diagram showing the fracture process zone as a cohesive zone capable of carrying cohesive tractions unlike the traction free crack.

The length of the fracture process zone is given by (Bazant and Planas 1998):

$$l_p = \eta \cdot \left(\frac{K_{IC}}{f_t'} \right)^2 \tag{2.3}$$

The size of the fracture process zone is observed to be dependent on the geometry of the specimen and is studied experimentally for specimens of different geometries throughout this study.

The non-constant stress redistribution ahead of the crack tip in quasibrittle materials generates a larger fracture process zone, which is generally assumed to be proportional to the characteristic length, l_{ch} (Hillerborg 1976):

$$\ell_{ch} = \left(\frac{K_{IC}}{f_t'} \right)^2 = \frac{E' G_f}{f_t'} \tag{2.4}$$

The parameter c_f is defined as the effective length of the process zone and it represents the equivalent length of an LEFM crack extension Δa_{ec}. The equivalent LEFM crack extension is only defined when the specimen size is large enough such that the fracture process zone can be neglected as shown in Equation 2.5, where D is a characteristic dimension of the specimen that is representative of its size:

$$c_f = \lim_{D \to \infty} \Delta a_{ec} \tag{2.5}$$

Fakhimi and Tarokh (2013) formulated a set of approximate theoretical equations based on Bazant's size effect law to predict the length and width of the fracture process zone in specimens of quasibrittle materials of different sizes. As the specimen sizes get bigger, the length and width of the process zone size will reach a limiting value in a large enough specimen. When the specimen is large enough, the dimensions of the process zone are no longer size dependent and become constants given by l_∞ for the length and W_∞ for the width. The subscript "∞" signifies that the specimen is large enough that size dependence does not longer play a role.

Equations 2.6 and 2.7 (Fakhimi and Tarokh 2013) can be used to predict length and width of the process zone at different sizes:

$$l = \frac{l_\infty D}{D_{ol}\left(1 + \frac{D}{D_{ol}}\right)} \tag{2.6}$$

$$W = \frac{W_\infty D}{D_{oW}\left(1 + \frac{D}{D_{oW}}\right)} \tag{2.7}$$

where l_∞, W_∞, D_{0l}, and D_{0W} are constants that can be calculated empirically based on a linear regression of the experimental measurements of the length and width of the fracture process zone.

As it can be seen in Figure 2.4, Equations 2.6 and 2.7 predict that the length and the width of the process zone to increase with specimen size until, for a large enough specimen, a limiting value for the length and width, l_∞ and W_∞, is reached. The specimen size for which the length of the process zone reaches a constant value is not necessarily equal to that one with a constant process zone width. The specimen sizes for which the length and width reach a constant value are defined as D_l and D_w for the length and width respectively. In general $D_l > D_w$, the reason is that the most dominant factor affecting the width of the fracture process zone is the grain size, which stays constant for increasing specimen sizes. Therefore, for a specimen of size D, if $D > D_w$, both the width and length of the process zone will increase with size, if $D_w < D < D_l$ the width is constant but the length increases with size, and if $D > D_l$ both the length and the width will be constant.

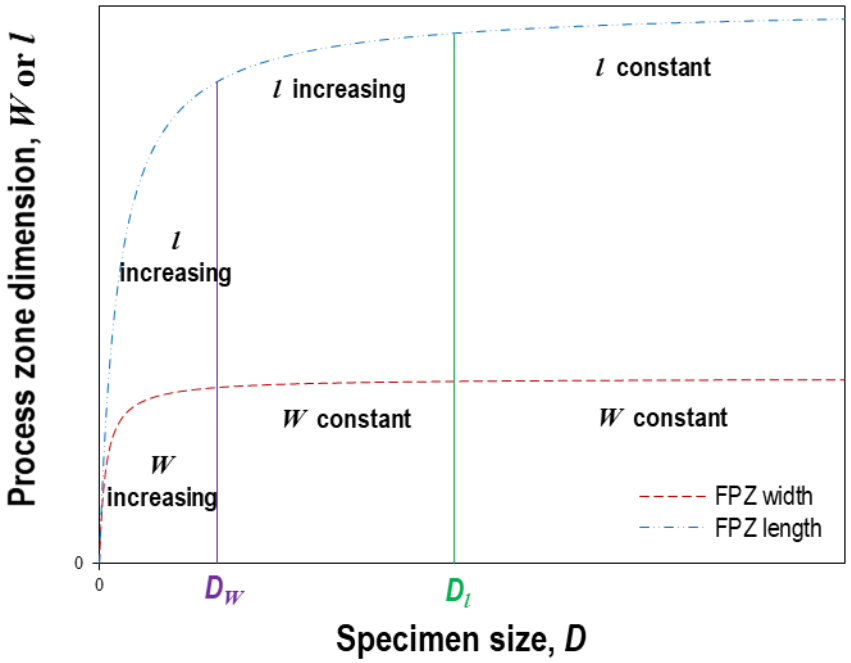

Figure 2.4: Predicted fracture process zone length and width for Rockville granite specimens of different sizes (adopted from Tarokh et al. 2017).

Size Effect on Fracture Properties

In classical plasticity or strength theory, the strength of a structure of geometrically similar specimens is independent of size. This does not hold true for quasibrittle materials such as concrete and rock where a size effect is observed. The sources of size effect include boundary layer effects, diffusion phenomena, statistical size effects, and, most importantly, the way how the energy stored in the structure is released into the fracture front, also known as the fracture mechanics size effect (Bazant and Planas 1998).

The size effect can be formulated through the concept that a crack will propagate when the energy required to fracture the material is equal to the available energy. Bazant and Planas (1998) define the strength of a structure as the value of the nominal stress σ_n at peak load. The nominal stress depends on the geometry and loading conditions on the specimen as shown in equation 2.8.

$$\sigma_n \propto \frac{P_{\max}}{bD} \tag{2.8}$$

where P_{max} is the maximum load, D is a characteristic dimension of the specimen (depth of the beam), and b is the width.

The fracture mechanics size effect is based on energy considerations. Figure 2.5 shows a beam with an initial crack length of a_o and a fracture process zone length of l_p that is subjected to a tensile stress of σ_n. When the tensile stress causes the crack to propagate by Δa, while the far field stress remains constant, the strain energy density changes from σ_n^2/E to zero in the stress relief zone (the dark grey strip). As a result, the released strain energy is equal to σ_n^2/E times the stress relief zone. Equating the required energy for crack propagation to the available energy yields:

$$G_f = 2 \cdot k \cdot (a_o + c_f) \cdot \frac{\sigma_n^2}{2E} \tag{2.9}$$

This expression is used to derive an equation for the nominal stress known as Bazant's size effect law (Bazant 1984):

$$\sigma_n = \frac{Bf_t'}{\sqrt{1+\frac{D}{D_o}}} \tag{2.10}$$

where B is a dimensionless constant and D_0 is a constant with the dimension of length.

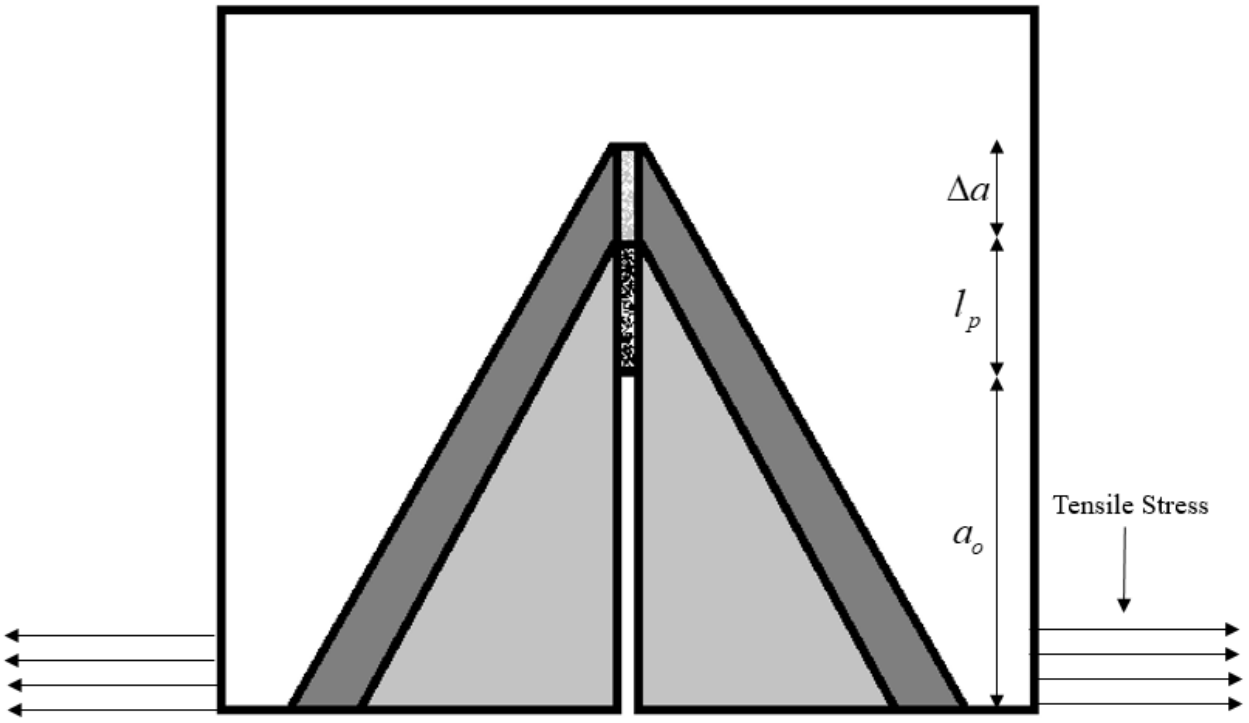

Figure 2.5: An ideal semi-infinite solid with a notch under tensile loading.

Bazant's size effect law formulates the nominal strength of a specimen as a function of its size (Figure 2.6). Small specimens behave according to the strength or plasticity criterion while large specimens, where the process zone can be neglected in relation to the specimen size, behave according to LEFM. The specimen sizes that are generally used in laboratory experiments fall within the transition region in between.

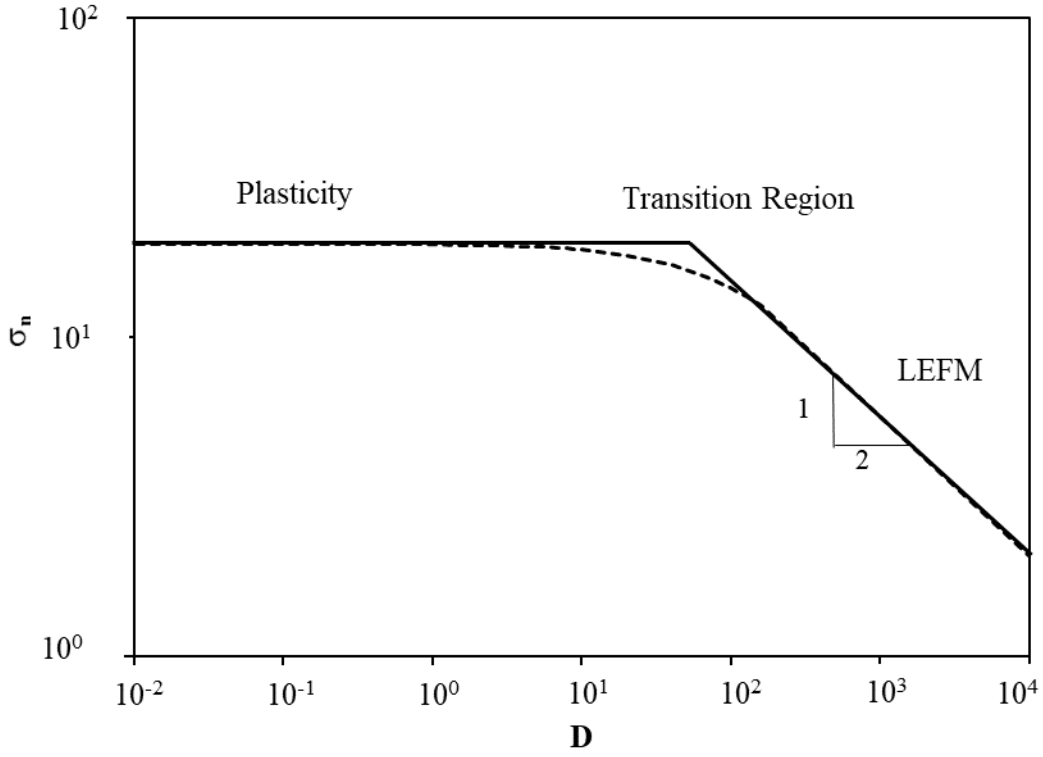

Figure 2.6: Bazant's (1984) size effect law for applied tensile stress σ_n.

As observed in Figure 2.6, the specimen's behavior at failure depends on its size, which is represented by *D*. As a result, by taking the limiting cases for the specimen size *D*, the behavior can be summarized as

$$\begin{aligned} D \ll D_o &\rightarrow \sigma_n \propto \frac{1}{\sqrt{D}} \\ D \approx D_0 &\rightarrow \sigma_n = Bf_t' \\ D \gg D_0 &\rightarrow Transition \end{aligned} \tag{2.11}$$

The brittleness number β (Bazant and Planas 1998) is a dimensionless parameter that was introduced to describe the specimen's behavior at failure:

$$\beta = \frac{D}{D_0} \tag{2.12}$$

β is usually between 0.1 and 10 for quasi brittle materials.

$$\begin{aligned} \beta > 10 &\rightarrow LEFM \\ \beta < 0.1 &\rightarrow Strength \\ 0.1 < \beta < 10 &\rightarrow Transition \end{aligned} \tag{2.13}$$

The parameters in Bazant's size effect law can also be expressed as following:

$$Bf_t' = \sqrt{\frac{E' \cdot G_t}{k \cdot c_f}} \tag{2.14}$$

$$D_0 = c_f \cdot \frac{D}{a_o} \tag{2.15}$$

Three and Four-Point Bending Testing

In order to study Mode I fracture process in rock experimentally, three and four-point bending tests can be performed on specimens of different sizes. A notch with an initial length of a_0 was carved in the center of the span of the specimens to act as a point of stress concertation so that a single crack would be generated and its location would be known beforehand. The reason that a notch is needed is because without it the position where the fracture initiates is random due to the inherent heterogeneity of the material.

Figure 2.7 shows a diagram explaining the stress in the specimen throughout fracture propagation in a three-point bending test. As the test begins and the load begins to build up, the fracture process zone is not yet developed, the stress distribution is linear and there is a tensile load on the notch. The fracture process zone starts to form and the applied load continues to increase until the fracture process zone is fully developed. As the load P increases and it reaches a critical value P_0, the tensile strength f'_t at the notch tip is reached due to the concentration of stress at that point. As it can be observed in the Figure 2.7, the stress distribution within the process zone is

nonlinear. As the crack propagates, the load decreases because the crack reduces the load carrying capacity of the specimen. The fracture process zone precedes fracture propagation and it propagates ahead of the crack tip. The crack is not capable of carrying any traction and the stress distribution in the fracture process zone continues to be inelastic. It is assumed that the fracture process zone propagates without changing size once it is fully developed as the traction free crack propagates. The length of the process zone and the traction free crack combined is referred to as the effective crack length a_e.

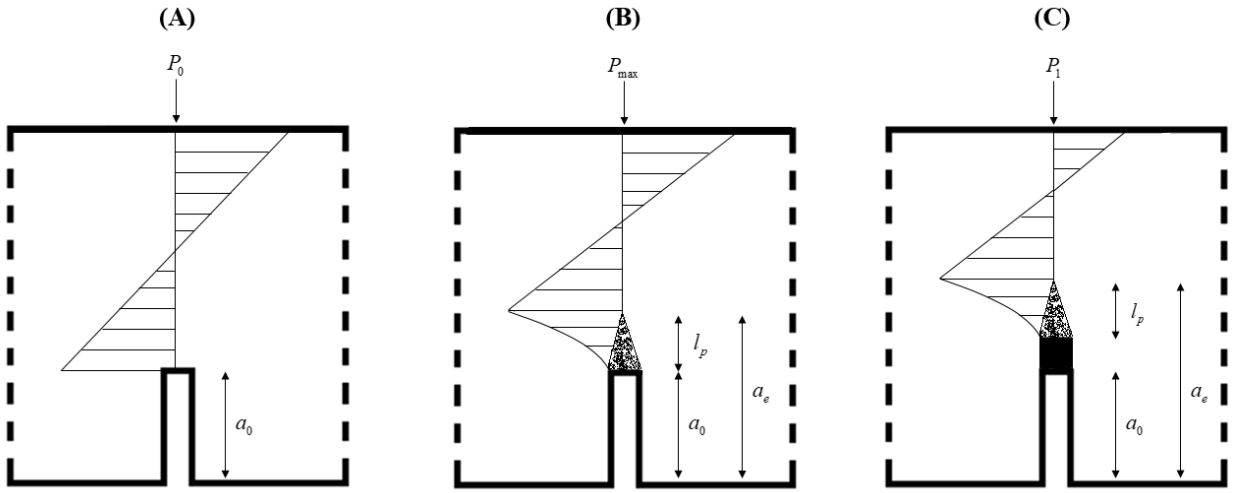

Figure 2.7: Stress distribution in a three-point bending test of a notched specimen in a quasibrittle material when (A) the fracture process zone has not yet developed (B) when the fracture process zone has fully developed and (C) when the fracture is propagating.

Experiments can also be carried out using four-point bending loading conditions. The stress distribution at the notch for a four-point bending test is similar; but unlike in three-point bending tests, the peak stresses are produced along an extended region of the specimen. The purpose of performing four-point bending tests is to study how a different stress distribution can affect the fracture process zone and the fracturing process.

CHAPTER 3: EXPERIMENTAL METHODS

Three-point and four-point bending tests were performed on geometrically similar specimens of different sizes with the purpose of studying the effect that specimen size and loading conditions have on the nominal strength, fracture toughness, and the size of the fracture process zone. Different studies have been carried out to investigate the size dependence of fracture properties in rock under three-point bending tests (Lin and Labuz 2013, Tarokh et al. 2017, Lin et al. 2019). Li et al (2017) used AE and DIC to study the fracture process zone in Barre granite under four-point bending and Topic et al. (2016) compared the flexural strength of composite reinforced concrete under three-point and four-point bending tests.

Three-point bending tests on notched specimens are widely used to study Mode I fracture. The geometry of the set up causes a tensile stress concentration on the notch tip that results in the propagation of a Mode I crack. The peak stress that is induced in three-point bending tests is at the mid-point of the specimen while the stress is reduced elsewhere. As a result, three-point bending tests are used to study the localized tensile stress around the notch tip. A diagram of a typical three-point bending test with a carved notch is shown in Figure 3.1.

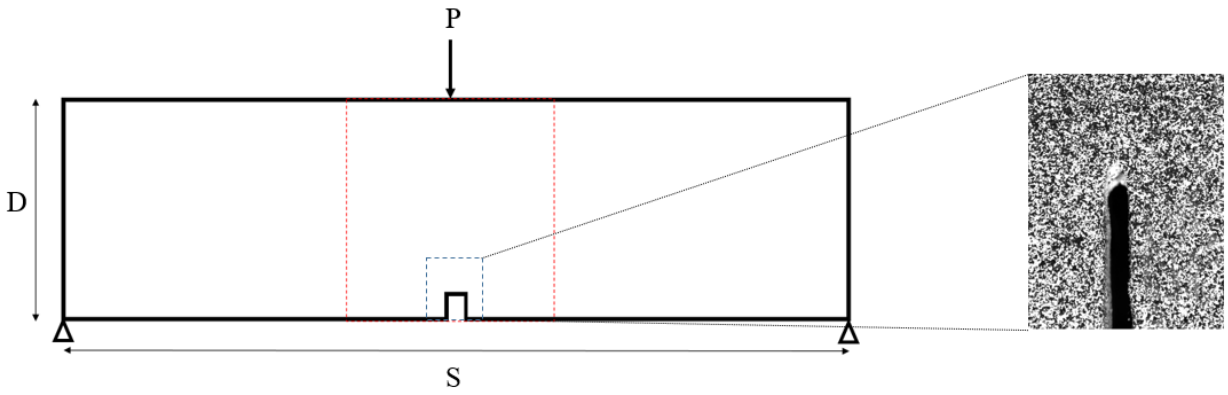

Figure 3.1: Three-point bending test geometry.

In contrast to three-point bending tests, four-point bending tests produce peak stresses along an extended region of the specimen. Four-point bending tests were performed in order to further study the influence of the loading conditions on fracture propagation and the fracture process zone. All other conditions were kept identical to the three-point bending tests. A schematic diagram of the four-point bending tests can be observed in Figure 3.2.

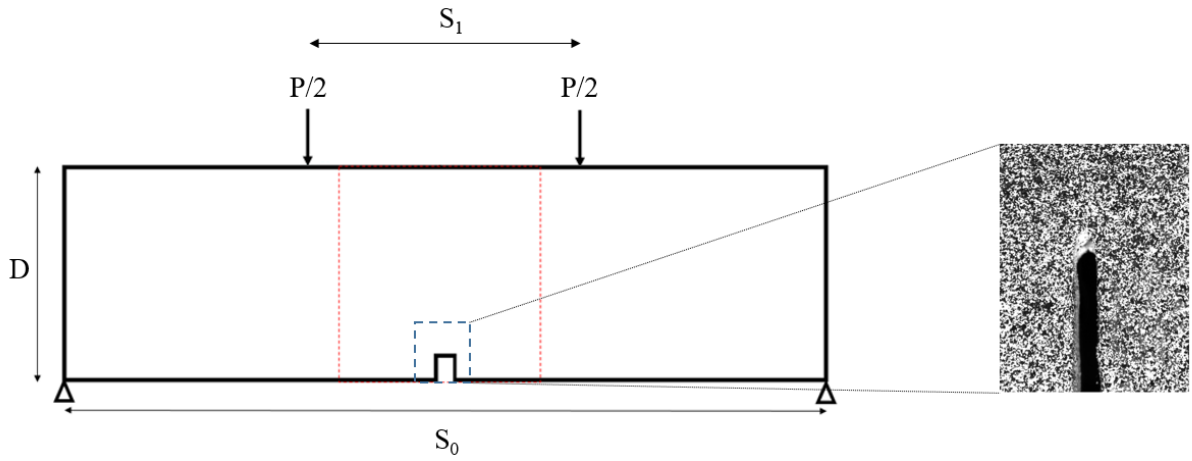

Figure 3.2: Four-point bending test geometry.

Experimental Set Up

An experimental system was designed and built such that three and four-point bending tests could be performed on specimens of different sizes. The experimental system allowed for the movement of the supports to accommodate specimens of different sizes for both three-point and four-point bending tests. In order to carry out the analysis using DIC, the experimental system included a camera and a camera stand that could be attached to the load frame, so that the relative velocity of the camera to the rock beam remained zero at all times. In other words, the camera moved along with the specimen throughout the test so the area of the specimen that was being photographed remained constant. The central region of a specimen was painted with white paint

and a white-black (greyscale) speckle pattern to be used for the DIC tracking was created by sprinkling extra-fine black glitter on top of the paint layer. A one-millimeter wide notch was carved in the center of the specimens to act as a point of stress concertation and a controlled point of fracture initiation. In the granite specimens, a constant notch to depth ratio of one to four was used. The experimental set up can be observed in Figure 3.3.

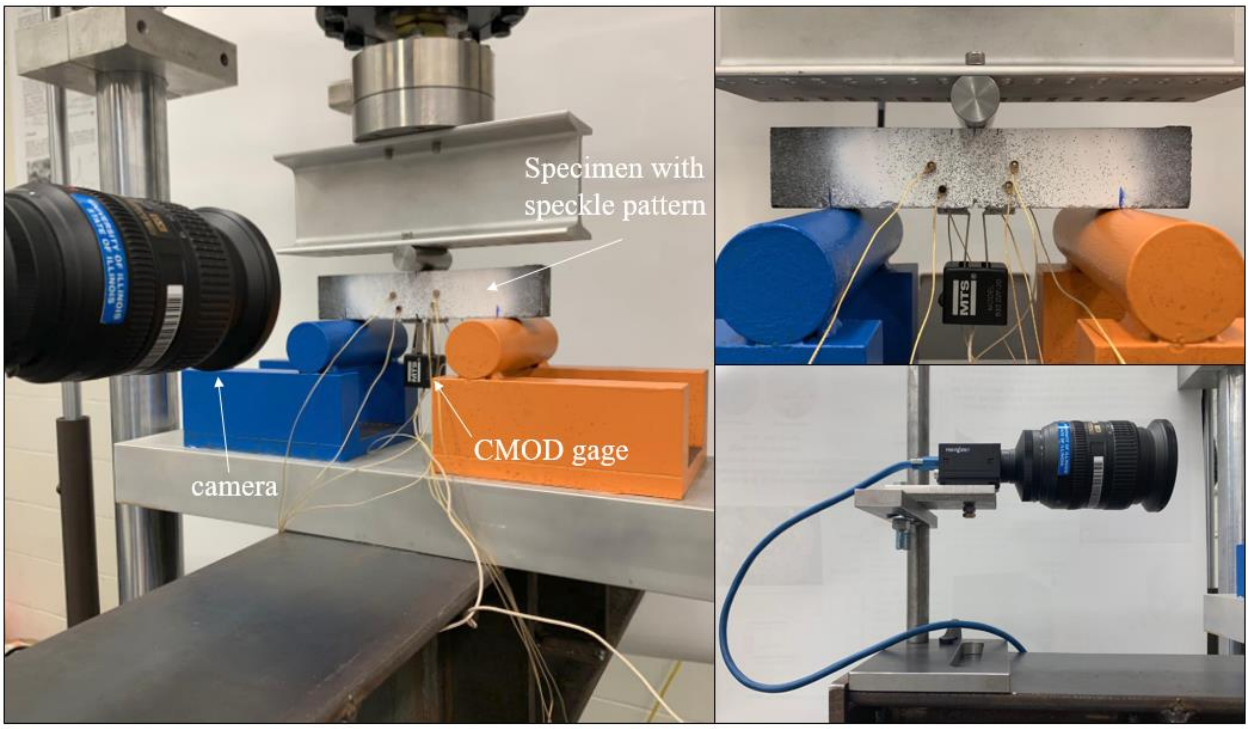

Figure 3.3: Experimental set up.

The fracture tests were performed using a closed loop servo hydraulic 20-kip load frame from MTS Systems. The load frame allowed control of the crack propagation by implementing a constant rate of crack-mouth opening displacement (CMOD). The CMOD was controlled through a feedback of a CMOD clip gauge that measures the displacement of two clips glued at both sides of the notch as shown in the Figure 3.3. The digital images where captured using a Grey Scale

Point Grey Research Grasshopper 3 GS-3 camera with an AF-S NIKKOR 18-200mm Nikon lens and the software FlyCap2, with the capability of recording at nine frames per second. The digital images were analyzed using the software package VIC-2D 6.0 by Correlated Solutions © and MATLAB.

Material

Three types of materials were tested in three-point bending for this study: Berea sandstone, Adelaide Black granite and Charcoal granite. Their properties are described below.

Berea sandstone: One test was performed using Berea sandstone, the purpose of this test was to be used as a calibration for the experimental system and the data processing methodology. The results were verified with the results obtained by Lin and Labuz (2013), which also used DIC to characterize the fracture process in Berea sandstone.

Tested Berea sandstone is conformed of uniformly sized grains ranging in size from 0.1-0.8 mm, it is slightly anisotropic with a 5% variation in P-wave velocity. It has a porosity of 20%, a Young's modulus of 10-14 GPa and a Poisson's ratio of 0.31-0.34. The tensile strength is 3.4-3.6 MPa. The specimen tested was a beam with a depth of 52 mm, a span of 127 mm, a width of 25 mm and the notch size was 12 mm long and 2 mm wide. The peak load in the three-point bending test was 420.4 N, which yields a nominal strength of 1.65 MPa. The apparent fracture toughness for the specimen was found to be K_{ICA}=1.47 MPa·m$^{0.5}$. A picture of the Berea sandstone specimen with the carved notch and the speckle pattern is shown in Figure 3.4.

Figure 3.4: Berea sandstone specimen tested in three-point bending.

Adelaide Black granite: Adelaide Black granite is a crystalline gabbro with an average grain size of 2 mm and density ρ = 2830 kg/m^3. The calculated values of dynamic (obtained from wave velocities) Young's modulus and Poisson's ratio (E [GPa]; ν) ratio are (102 GPa; 0.21), (100 GPa; 0.22), and (94 GPa; 0.23). These values correlate well (within 3%) with the same parameters measured in static uniaxial compression tests performed on cylindrical specimens (30 mm in diameter and 60 mm tall) cored in the same directions: (110 GPa; 0.21), (105 GPa; 0.30), and (91 GPa; 0.21). Close correlation between the elastic properties obtained from ultrasonic (dynamic) and static (strain rate ~ 10^{-6}/s) measurements is attributed to low crack density in the rock. The ultrasonic velocities are measured in three different directions ($c_{p,s}$ [km/s]; $c_{s,s}$ [km/s]) are (6.30; 3.83), (6.31; 3.33), and (6.16; 3.66), indicating slight (2-4%) anisotropy (Makhnenko et al., 2010). The specimens and their dimensions can be observed in the Table 3.1 and picture of an Adelaide Black granite specimen with the carved notch and the speckle pattern can be observed in Figure 3.5.

Table 3.1: Adelaide Black granite specimen dimensions.

Specimen	***D***	***S***	***b***
	[mm]	**[mm]**	**[mm]**
ABG1	43	123	25
ABG2	48	123	13
ABG3	68	123	22
ABG4	35	123	22
ABG5	39	65	25

Figure 3.5: Typical Adelaide Black granite specimen tested in three-point bending.

Charcoal granite: The ultrasonic velocities of Charcoal granite were measured in three different directions, the obtained results are: ($c_{p,s}$ [km/s]; $c_{s,s}$ [km/s]) (5.62; 3.43), (5.53; 3.34), and (5.63; 3.43), indicating slight (2-4%) anisotropy. The porosity was found to be 1.5% and $\rho = 2780$ kg/m^3. Specimens of three different sizes of Charcoal granite were tested: small, medium and large sized. Two specimens of each size for each loading condition were tested for verification purposes. Table 3.2 shows the dimensions of each Charcoal granite specimen tested under three-point bending and Figure 3.6 shows a photograph of the three specimen sizes that were used.

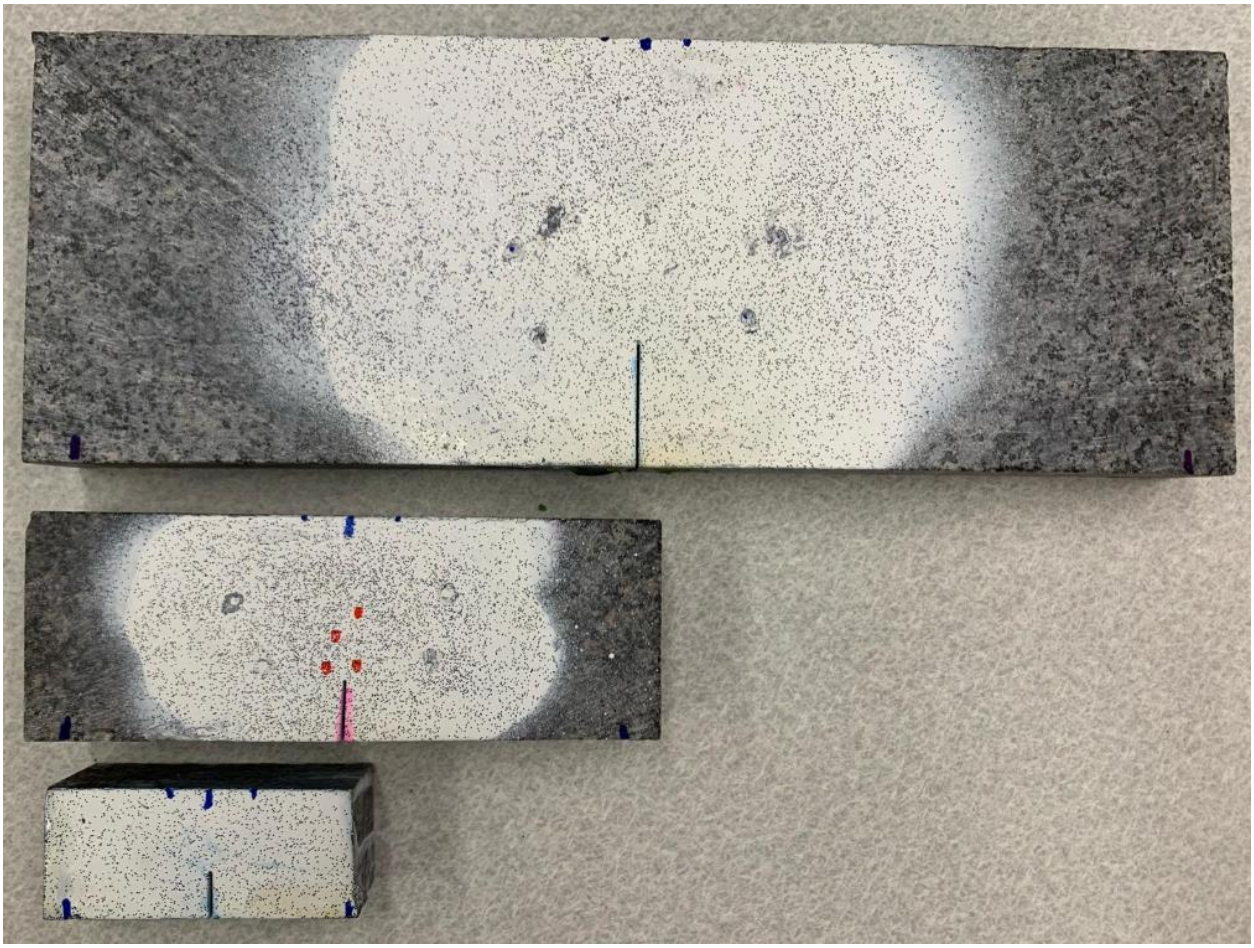

Figure 3.6: Charcoal granite specimens of different sizes.

Table 3.2: Three-point bending Charcoal granite specimen dimensions.

Specimen	***D***	***S***	***b***
	[mm]	**[mm]**	**[mm]**
CGA1	25.4	63.5	29.0
CGA2	25.4	63.5	29.0
CGA3	50.8	127.0	27.0
CGA4	50.8	127.0	29.0
CGA5	101.6	254.0	25.0
CGA6	101.6	254.0	27.0

Four-Point Bending Tests

The four-point bending tests were carried out using Charcoal granite specimens. The specimen geometries that were tested in four-point bending are summarized in Table 3.3. Similarly to the three-point bending tests, specimens of three different sizes were tested. Two specimens of each size were tested for result validation purposes.

Table 3.3: Four-point bending Charcoal granite specimen dimensions.

Specimen	***D***	***S***	***b***
	[mm]	**[mm]**	**[mm]**
CGA1	25.4	63.5	25.0
CGA2	25.4	63.5	25.0
CGA3	50.8	127.0	29.0
CGA4	50.8	127.0	30.0
CGA5	101.6	254.0	20.0
CGA6	101.6	254.0	27.0

Experimental Determination of Fracture Parameters

In three-point bending tests the nominal strength is defined by

$$\sigma_n = \frac{3SP_{\max}}{2bD^2} \tag{3.1}$$

where S is the span of the beam.

The relationship between the peak load and the specimen size derived from Bazant's size effect law is

$$P_{\max} = \frac{2bD^2 Bf_t'}{3S\sqrt{1+\frac{D}{D_o}}} \tag{3.2}$$

The apparent fracture toughness K_{ICA} is defined as the fracture toughness for a specimen of a specific size, since the real fracture toughness should be size independent. The apparent fracture toughness for a specimen undergoing three-point bending with an arbitrary span to depth ratio *S/D* is given by (Bazant and Planas 1998):

$$K_{ICA} = \sigma_n \sqrt{D} \frac{\sqrt{\alpha}}{(1+2\alpha)(1-\alpha)^{1.5}} P_{\frac{S}{D}}(\alpha) \tag{3.3}$$

where $\alpha = a_0/D$ is the notch to depth ratio and $P_{S/D}(\alpha)$ is a function of the span to depth ratio of the beam.

$P_{S/D}(\alpha)$ for an arbitrary *S/D* can be calculated using the known values for $P_{S/D}(\alpha)$ for the limiting case of pure bending when *S/D* approaches infinity using Equation 3.4 and for *S/D* =4 (the ASTM standard testing geometry) using Equation 3.5:

$$P_{\infty}(\alpha) = 1.989 - \alpha(1-\alpha)[0.0448(1-\alpha) + 1.226(1-\alpha)^2] \tag{3.4}$$

$$P_4(\alpha) = 1.900 - \alpha[-0.089 + 0.603(1-\alpha) - 0.441(1-\alpha)^2 + 1.223(1-\alpha)^3] \tag{3.5}$$

Therefore, $P_{S/D}$ for an arbitrary notch to depth ratio can be derived:

$$P_{\frac{S}{D}}(\alpha) = P_{\infty}(\alpha) + \frac{4D}{S}[P_4(\alpha) - P_{\infty}(\alpha)] \tag{3.6}$$

In four-point bending tests the nominal strength is defined by

$$\sigma_n = \frac{3P_{\max}(S_0 - S_1)}{2bD^2} \tag{3.7}$$

where S_0 is the outer span, S_1 is the inner span. The relationship between the peak load and the specimen size derived from Bazant's size effect law is

$$P_{\max} = \frac{2bD^2 Bf_t'}{3(S_0 - S_1)\sqrt{1 + \frac{D}{D_o}}} \tag{3.8}$$

The apparent fracture toughness for a specimen undergoing four-point bending is given by (Bauerle, 2000):

$$K_{ICA} = P_{\max} \cdot \frac{3(S_0 - S_1)\sqrt{a_0}}{2bD^2} \tag{3.9}$$

Linear Regression Methods

Four linear regression methods that are used to calculate different fracture parameters are explained in this section.

Method #1: Determination of the fracture toughness

In order to find the real fracture toughness, it is necessary to find the equivalent apparent fracture toughness for an ideal specimen of infinite size. When the specimen size approaches infinity, the causes of size effect can be neglected and the obtained fracture toughness is considered to be a material property. The fracture toughness for an ideal specimen of infinite size can be found by plotting the apparent fracture toughness versus size in a linear form

$$Y = AX + C \tag{3.10}$$

Where $X=1/D$ and $Y=1/K_{ICA}^2$. The fracture toughness for a specimen of infinite size can be found by using the Y-intercept of the resulting graph. Since $X=1/D$, using the limiting value:

$$\lim_{D\to\infty} X = 0 \tag{3.11}$$

the fracture toughness obtained when $X=0$ is equivalent to the fractured toughness of an ideal infinitely large specimen.

Therefore, the fracture toughness is found when $X=0$ and is given by

$$K_{IC} = \frac{1}{\sqrt{C}} \tag{3.12}$$

Method #2: Determination of the parameters for Bazant's size effect law

Bazant's size effect law (Bazant and Planas 1988), shown in equation 2.10, describes how the nominal strength of a specimen depends on specimen size.

The equation can be algebraically rearranged into different linear forms where different linear regression methods can be used to extract relevant parameters. In this method, Bazant's size effect law is rearranged into the linear form using the following expression:

$$Y = AX + C \tag{3.13}$$

where $X=D$ and $Y=1/\sigma_n^2$.

The parameters Bf_t' and D_0 are given by

$$Bf_t' = \frac{1}{\sqrt{C}}, D_o = \frac{C}{A} \tag{3.14}$$

Method #3: Determination of the parameters for Bazant's size effect law, second method

It is possible to algebraically rearrange Bazant's size effect law into an alternative linear form:

$$Y' = A'X' + C' \tag{3.15}$$

where $X`=1/D$ and $Y=1/D\sigma_n^2$.

In this case, the parameters Bf_t' and D_0 are given by

$$Bf_t' = \frac{1}{\sqrt{A'}}, \; D_o = \frac{A'}{C'} \tag{3.16}$$

Method #4: Determination of parameters for the prediction of size of the process zone

From the equations formulated by Fakhimi and Tarokh (2013) based on Bazant's size effect law, the length and width of the process zone are given by equations 2.6 and 2.7

The parameters for the length can be obtain by plotting the experimental results for the fracture process zone length versus specimen size in the linear form

$$Y = AX + C \tag{3.17}$$

Where $X=1/D$ and $Y=1/l$.

Therefore, l_∞ is calculated using the Y-intercept of the resulting graph since:

$$\lim_{D\to\infty} X = 0. \tag{3.18}$$

and as a result, l_∞ and D_{0l} can be calculated as

$$l_\infty = \frac{1}{C},\ D_{ol} = \frac{A}{C} \tag{3.19}$$

Similarly, the parameters for the width are obtained by plotting the experimental results for the process zone width with the specimen size in the linear form:

$$Y = AX + C \tag{3.20}$$

where W_∞ and D_{0W} are given by

$$W_\infty = \frac{1}{C}, D_{oW} = \frac{A}{C} \tag{3.21}$$

Sources of Error

This section analyzes the sources of error in the presented results in order to provide a better understanding on the extent of the expected and observed variability of the data and its sources.

A relevant source of error is the limit on the resolution of measurements on the DIC grid. The resolution of the DIC grid is dependent on the size of the subset, the region of interest that was chosen for the correlation algorithm, and the resolution of the digital images. The surface displacement is measured at the center of each subset and the accuracy of the measurements is

dependent on this distance. The dimensions of these parameters are slightly different for each specimen size and the average DIC measurement resolution is between 0.1-0.2 mm. This error is present in the measurements of the dimensions of the fracture process zone. The dimensions of the fracture process zone were measured to the maximum resolution to which it was possible. The relative error resulting from the level of accuracy is given by

$$\varepsilon_{R(A)} = \left(\frac{d}{M} \right) \cdot 100\% \tag{3.22}$$

where d is the accuracy that was possible for that specific measurement and M is the value of the measurement, in this case the dimension of the fracture process zone that was measured, either the length or the width.

Another source of error that must be considered when calculating parameters from experimental results is the random error. Random error arises from the fluctuations in the results that are observed during the experiments. There are different causes for the random error, e.g. variations in the initial conditions of an experiment. These variations can result from the specimen preparation process resulting in uneven specimen dimensions. It is possible that the specimens were not ideally prismatic as it is assumed and that the dimensions varied slightly from one specimen to another. Other sources of random error come from the experiment preparation, where it is possible for any component of the experimental system is not set as intended. For instance, the specimen might not be perfectly centered under the supports or any technical issue that might have affected the results during the experiment. Finally, a significant source of random error is the inherent randomness within the material. Granite is a heterogeneous material and it is possible for results vary slightly from one specimen to another.

The random error is manifested in the difference in results of replicated experiments and in the deviation of the results from theoretical predictions. For instance, it is expected that the

results for the dimensions of the fracture process zone for different specimens can be algebraically rearranged to show a linear relationship with specimen size. However, when the results are rearranged and a linear fitting is performed, the coefficient of determination, R^2, is not equal to one. R^2 is a statistical measure of how closely the data conforms to the fitted curve, in this case a linear regression; therefore, when the values deviate from the predicted linear relationship due to the presence of random error, R^2 will not be equal to one. The random error is observed in the fluctuations of experimental results and is accounted for when these results are used to calculate parameters by

$$\varepsilon_{R(R)} = \left(1 - R^2\right) \cdot 100\% \quad (3.23)$$

The total relative error that results from the errors from measurement accuracy and random errors is given by

$$\varepsilon_R = \sqrt{\left(\varepsilon_{R(A)}\right)^2 + \left(\varepsilon_{R(R)}\right)^2} \quad (3.24)$$

Based on the experimental data (see section 5), the relative error is expected not to exceed 5%.

CHAPTER 4: DIGITAL IMAGE CORRELATION APPLIED TO FRACTURE IN ROCK

Introduction of Digital Image Correlation (DIC)

Digital Image Correlation (DIC) is a non-contact optical method that uses tracking and imaging techniques for accurate high-resolution measurements of changes in images. There are many fields of application for DIC and it is often used to obtain full field displacements and strains.

DIC tracks the surface displacement of a specimen by comparing digital images of the specimen at different stages of loading. In order to track surface displacement, the specimen surface is covered in a random speckle pattern. The speckle pattern is a pattern with a random distribution of intensities in the grey scale and it is responsible for carrying the deformation information. For digital images in the grey scale, light intensity values are assigned to each color from black to white (Sutton 2009). In this study the speckle pattern was created by applying a layer of white paint on the specimen and scattering extra-fine black glitter on it while the paint was still fresh. To be as effective as possible, the speckle pattern must have the following characteristics: high contrast, randomness, isotropy, and deform along with the specimen surface.

The speckle pattern movement is tracked by performing extensive numerical analysis where the reference image (from a previous loading stage) is compared to the current image through a correlation algorithm. The algorithm tracks small regions called subsets and locates the subset in the current image. The location of maximum correlation between the reference and current image coincides with the location of the displaced subset (Figure 4.1).

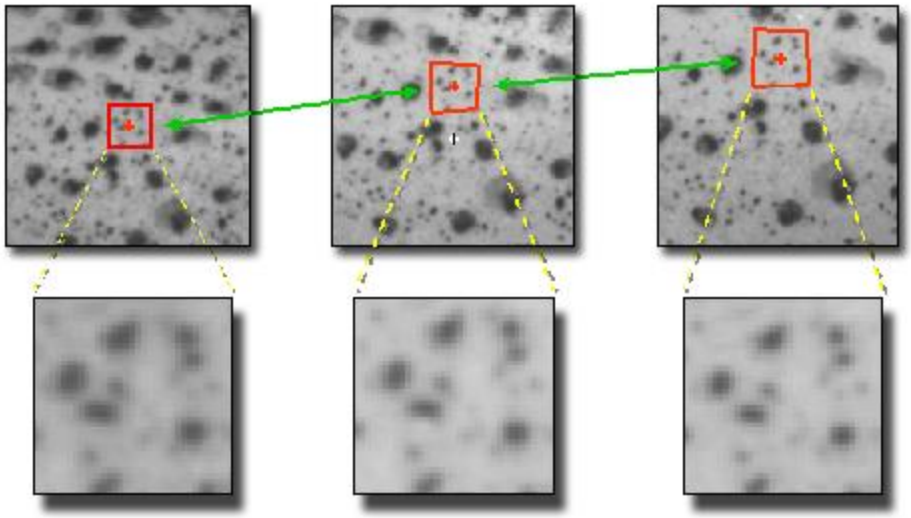

Figure 4.1: Algorithm of the tracking of the location of the center of a subset (adopted from Correlated Solutions ©).

During the experiment, digital images of the specimen are captured throughout the deformation process. The camera converts the light into a digital file composed of small units called pixels. The total number of pixels in a file is referred to as the resolution, which depends on the camera. Each pixel is assigned a digital value called the greyscale value depending on its light intensity, greyscale values range from 0 to 255. Pixels with a higher light energy value, such as white have a high greyscale value and darker pixels have lower greyscale values. A speckle pattern has a random distribution of these intensity values as shown in Figure 4.2.

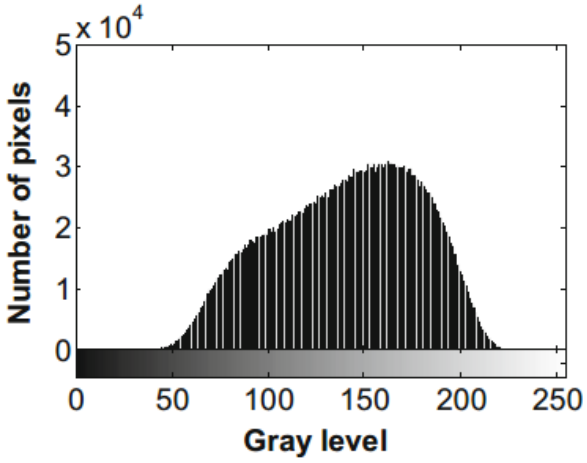

Figure 4.2: Distribution of the intensity values in the grey scale for a typical speckle pattern (adopted from Correlated Solutions ©).

During the processing stage, a relatively small region called the Region of Interest (ROI) is selected. The ROI serves as the searching area for the displaced subset. The reason that an ROI is selected is because it is not practical nor necessary to search for the displaced subset in the entire specimen because the displacements involved are usually small. The original and displaced sublets are matched by correlating the best fit of intensity patterns. When the matching of intensity patterns of the original and displaced subset is found to be optimal, the two subsets are regarded as the same, before and after deformation.

For a subset in the ROI centered at position *P(X,Y)* for the reference image taken before loading at time t_1, the intensity value corresponding to that subset is a function of its position and is given by

$$I(P) = I(X, Y) \tag{4.1}$$

The loading results in a displacement of (u_x, u_y) causing *P* to move to point *P'*. A new image is taken at a later time t_2 and the intensity values are given by:

$$I'(P') = I'(X + u_x, Y + u_y) \tag{4.2}$$

The intensity values are searched in order to determine the best subset match using a cross-correlation method in the ROI. A cross correlation function *R* is defined as the two dimensional spatial convolution of *I* and *I'* with a separation vector *S* in the correlation plane.

$$R(s) = \int I(P)I'(P'+s)dP \tag{4.3}$$

The cross correlation function has a global maximum that corresponds to the correlation of identical speckles from two images as shown in Figure 4.3. The position of the peak indicates the direction of the displacement vector in the subset. As a result, the average displacement of the speckles in the subset is interpreted as the displacement of the center of the subset. The complete displacement field is obtained by processing all the subsets in the image.

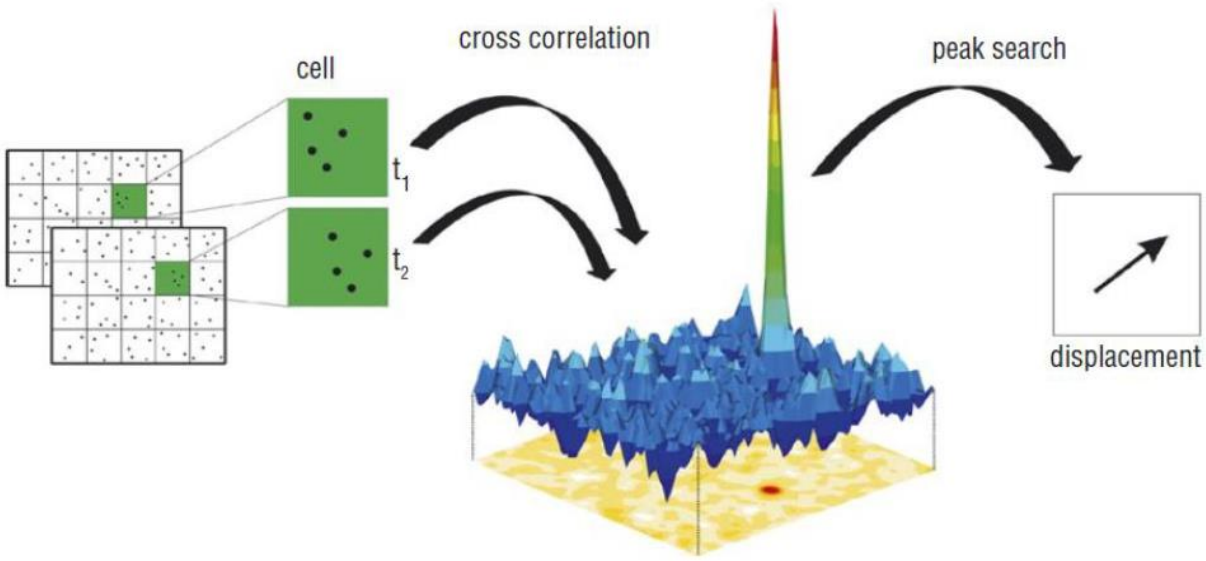

Figure 4.3: Matching the subsets before and after deformation using the global maximum of the cross correlation function (adopted from Correlated Solutions ©).

DIC is used in this study to extract important information regarding the fracture process zone by comparing surface displacements at different stages of loading. The displacement is calculated continuously on the surface of the specimen as it is loaded, as a result it is possible to

know exact displacements at different loading stages. By analyzing these displacements, different fracture parameters are calculated. Identifying different fracture parameters such as at what loading stage the fracture begins to propagate, the size of the fully developed process zone, and the size of the traction free crack at different loading stages is a challenging task and multiple DIC techniques have been developed (Lin and Labuz 2013, Lin et al. 2019).

Two different methods that utilize DIC to calculate the size of the fracture process zone will be utilized in this study. The first method that will be explained, as outlined by Lin and Labuz (2013), relies on the horizontal displacement that a specimen experiences near the notch and in the area where the fracture propagates. In this study, this method will be referred to as the Critical Displacement Method. An important note on this method is the assumption that a traction free crack does not develop in the pre peak regime, according to the behavior predicted by LEFM. The second method that will be explained was outlined by Lin et al. (2019), this method will be referred as the Displacement Gradient Method because it uses the gradient of the horizontal surface displacements to calculate the length of the fracture process zone. The Displacement Gradient Method assumes that is possible for a traction free crack to propagate in the pre peak regime as it will be discussed in the corresponding section.

Critical Displacement Method

In the early stages of loading the specimen deforms elastically but displacements are concentrated around the notch tip because the notch acts as a stress concentrator. The displacements are observed to be approximately symmetric on both sides of the notch throughout loading.

As the load increases, a zone of displacement discontinuity that is related to the fracture process zone begins to develop near the notch tip. The location of the beginning to the zone of where displacement is not continuous can be identified using incremental horizontal displacement contours that are obtained through DIC. The tip is identified as the location where the contours begin to merge as observed in Figure 4.4. The displacement field is symmetric around the position where the displacement contours merge, signifying that there is displacement on both sides of the notch. Above the tip of the zone of displacement discontinuity, the displacements are still considered elastic. As the magnitude of the displacement increases with loading, the discontinuity eventually experience a jump, which is related to fracture initiation.

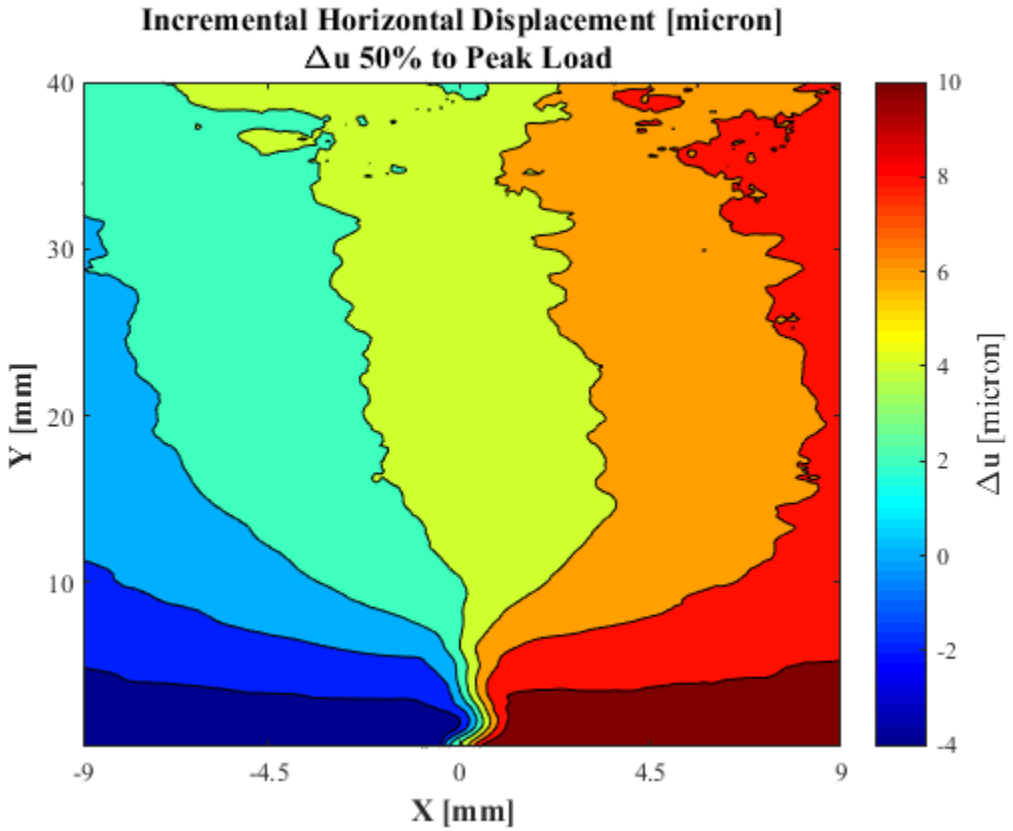

Figure 4.4: Incremental horizontal displacement in the Berea sandstone specimen from 50% to 100% peak load.

It is assumed that the traction free length does not propagate until the peak load is reached (Lin and Labuz 2013). Before peak load, however, the fracture process zone begins to develop. When peak load is reached, it is assumed that the fracture process zone has developed to its full size.

The critical opening displacement, w_c, is the threshold horizontal displacement after which the developing fracture is not capable of carrying traction anymore. w_c is calculated at the notch tip when fracture initiation begins to take place. The critical opening displacement is calculated along two vertical cross sections two millimeters away from the notch tip when the fracture initiates. The displacement is calculated two millimeters away from the crack because when the displacement gradients are extremely large, which is the case on the crack, the potential for computational errors in the DIC algorithm dramatically increases (Lin and Labuz 2013). Additionally, it is possible that the tortuosity of the crack could complicate the measurements. Therefore, measuring the displacement two millimeters away from the crack provides measurements that are more consistent and minimizes error.

The traction free length is identified as the area where the horizontal displacement on the sides of the crack is equal to or greater than the critical displacement. When the specimen reaches peak load, the traction free crack will begin to propagate and the specimen will begin to unload. As the load decreases in the post peak regime, the traction free crack continues to propagate. In post peak regime, the fracture will propagate and as it propagates, the load carrying capacity of the specimen will decrease.

The effective crack length is the combined length of the fracture process zone and the traction free crack. As explained above, the tip of the fracture process zone is identified as the point where the displacement contours merge. The transition from the traction free crack to the

fraction process zone is identified using the calculated critical displacement. When the opening displacement is equal to or greater than the critical displacement, the fracture is traction free. Therefore, the point where the displacement is equal to w_c separates the traction free region from the process zone l_p and together they form the effective crack length a_e.

Figure 4.5 shows a schematic diagram of the process zone and the fracture in the post peak regime. In the post peak regime, the effective crack length keeps increasing but the length of the process zone remains constant after reaching its fully developed value at peak load. The critical displacement w_c, is defined as the displacement that is big enough to create a discontinuity that is traction free. From the figure, point A is the tip of the effective crack length and of the process zone. At point B, the displacement is equal to w_c, so it is interpreted as the transition from the process zone to the traction free length.

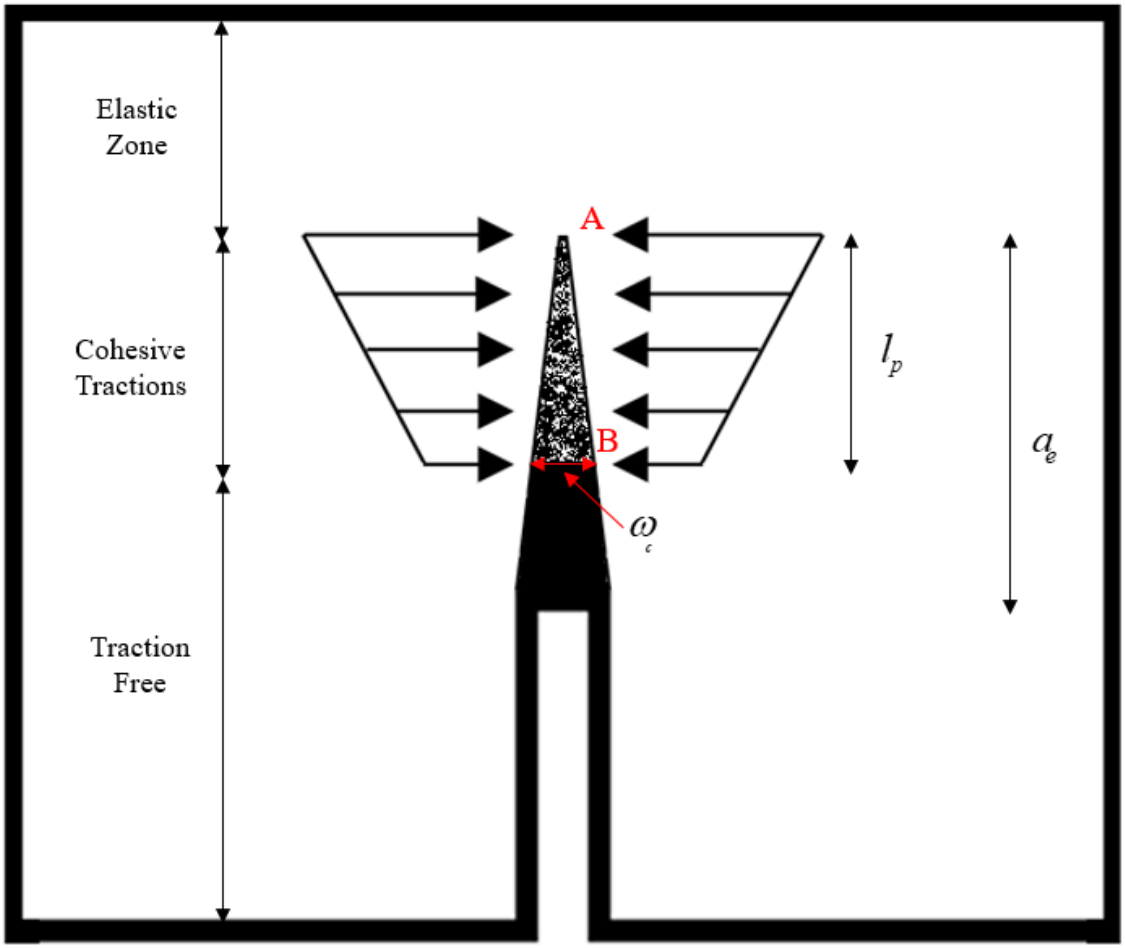

Figure 4.5: Diagram explaining the critical displacement method. Point A is the tip of the fracture process zone and point B, where the displacement is equal to w_c, is the end of the process zone or the tip of the traction free crack.

Figure 4.6 shows the horizontal incremental displacement contours for 70% pre peak load to peak load in the Berea sandstone specimen. The notch tip is at the origin of the defined coordinate axis. It is possible to observe how the contours are symmetric about the notch tip. The contours merge at around Y=8 mm, this is a result of the fracture process zone development up to peak load. The tip of the fracture process zone is identified as the merging point of the contours and its length starts from the notch tip, as no traction free crack has propagated before and up to the peak load.

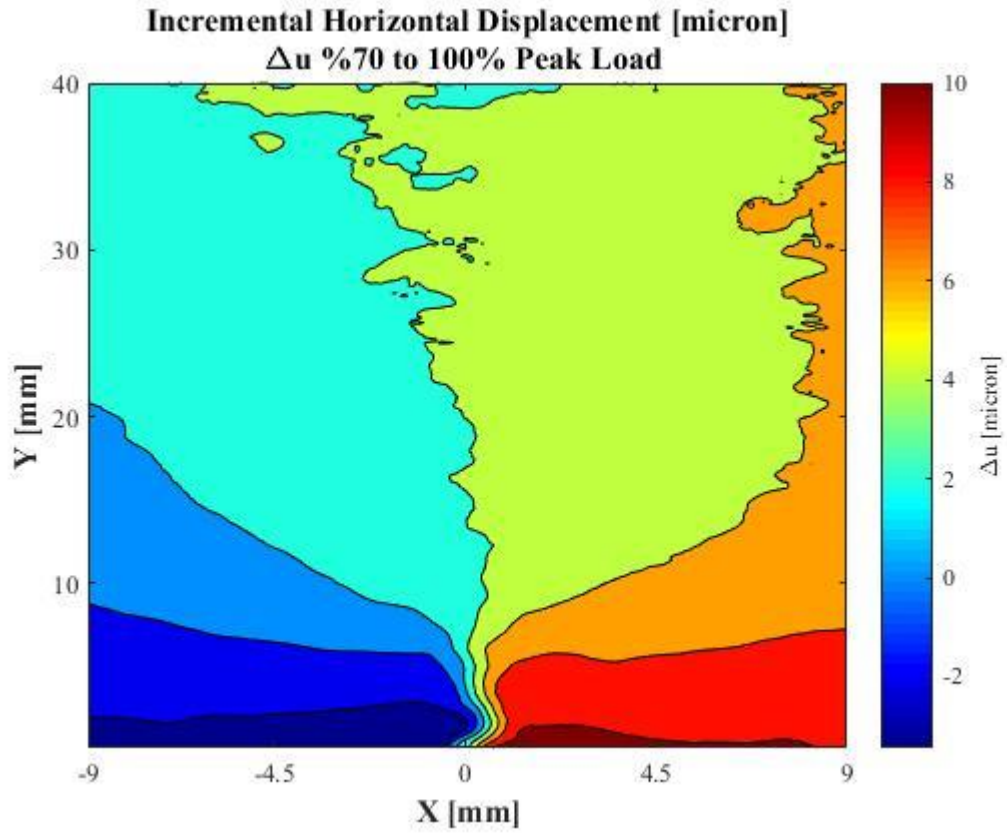

Figure 4.6: Incremental horizontal displacement in a Berea sandstone specimen from 70 to 100% peak load.

Figure 4.7 shows the horizontal displacement measured at vertical cross sections two millimeters away from both sides of the notch. The displacement was measured from the point of fracture initiation, when the fracture process zone began to develop or when the contours began to merge until peak load. The displacement calculated at the notch tip from fracture initiation to peak load was defined as the critical displacement - the maximum displacement the rock can locally experience while still carrying traction. In the post peak regime, whenever the displacement is greater than the critical displacement, it is assumed that area is not capable of experiencing cohesive tractions.

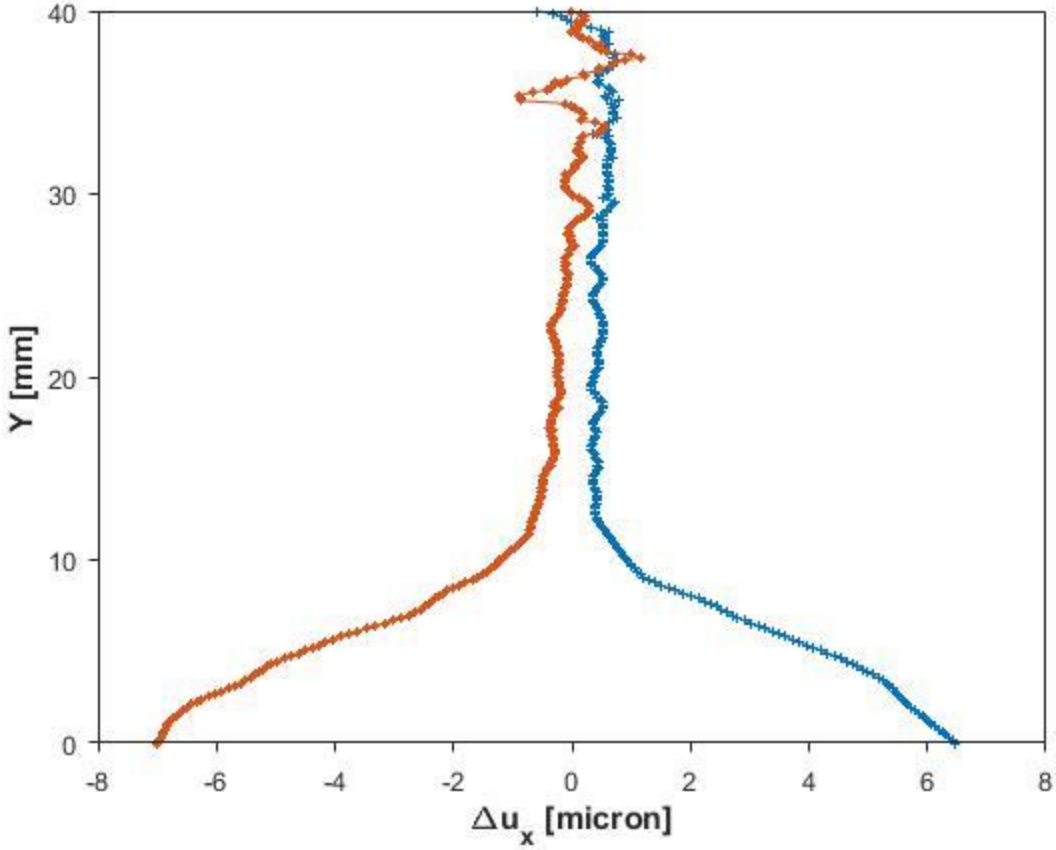

Figure 4.7: Displacement profiles at both sides of the notch for the sandstone specimen.

The effective crack length is calculated and the boundary between the fracture process zone and the traction free length is located using the critical displacement as a threshold value. The same procedure is shown here for one of the Adelaide Black granite specimens as an additional example. Figure 4.8 shows as an example the contours of the incremental horizontal displacements from 70% to peak load for the specimen ABG1.

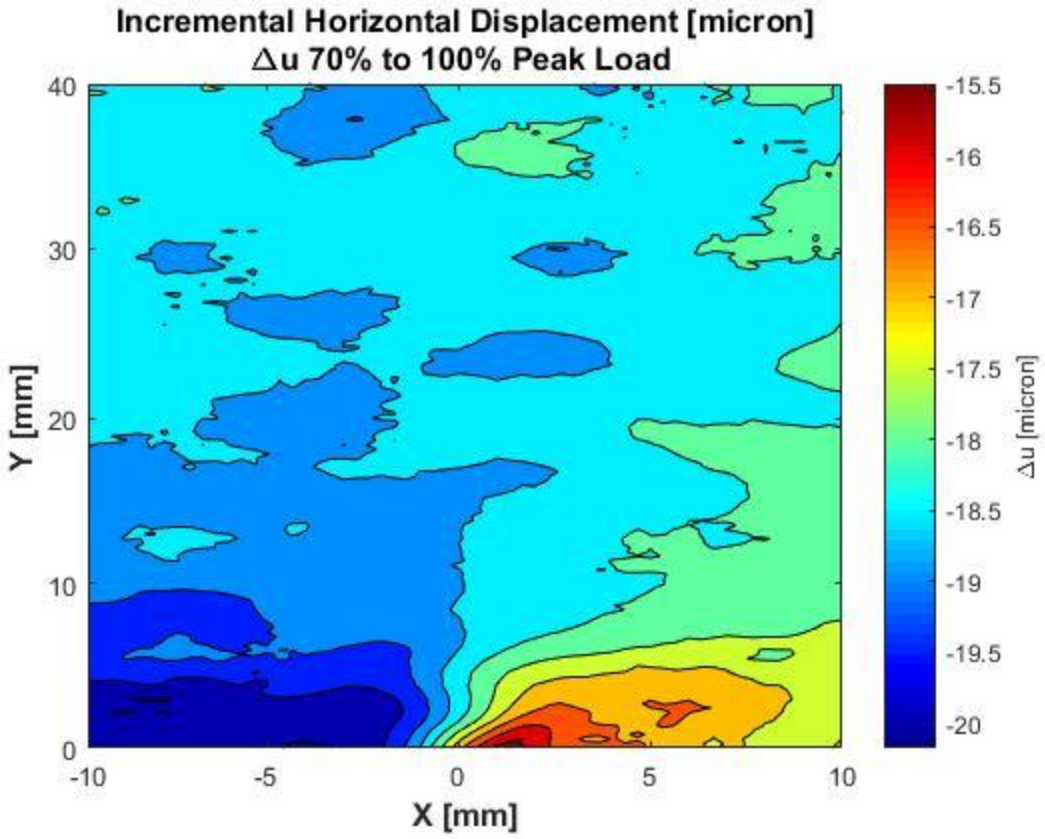

Figure 4.8: Incremental horizontal displacement contours from 70% to 100% peak load to peak load for specimen ABG1.

Figure 4.9 shows how the critical displacement was calculated for the ABG1 specimen. As expected, the critical displacement in Adelaide Black granite was significantly smaller than in Berea sandstone as it is a much stiffer material.

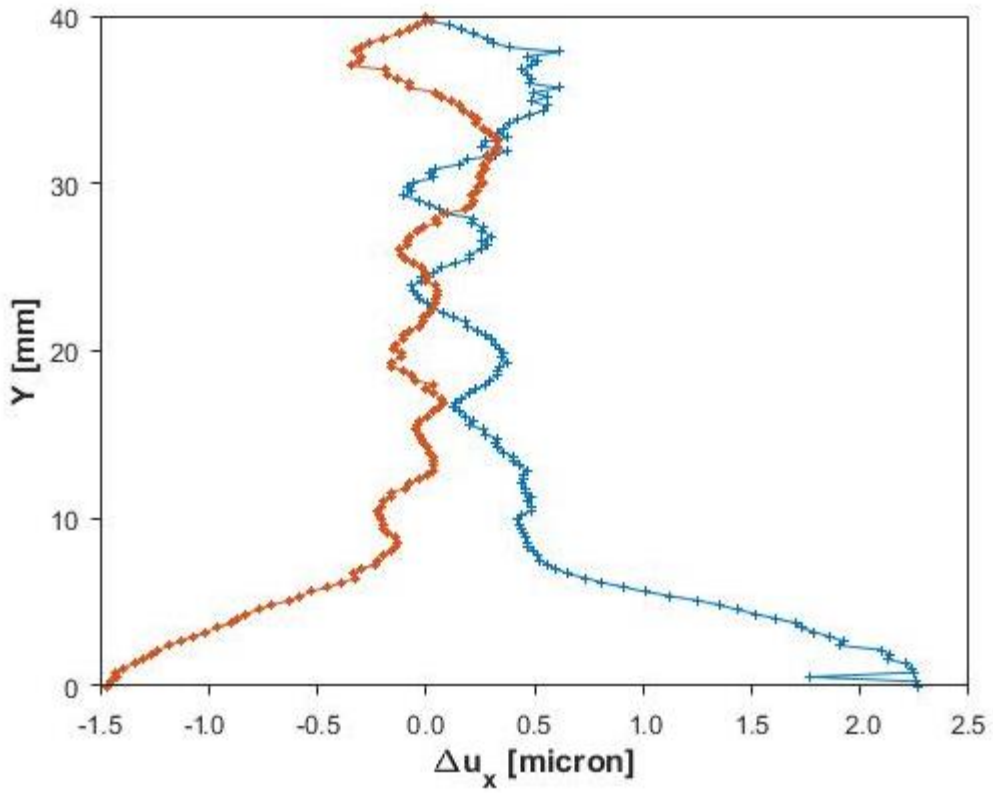

Figure 4.9: Displacement profiles at both sides of the notch for the specimen ABG1.

Displacement Gradient Method

The second method to calculate the size of the fracture process zone utilizing DIC will be referred to as the Displacement Gradient Method and it is explained in this section. The fracture process in a quasibrittle material does not completely adhere to the assumptions on which the rules of Linear Elastic Fracture Mechanics (LEFM) are based on. Quasibrittle materials behave in a nonlinear manner during fracturing, the fracture process zone around the fracture tip is one of the consequences of this. The existence of the fracture process zone near the fracture tip plays an important role in the fracturing process and more so in small specimens, which are often used in laboratory examinations. In order to deal with the influence and nonlinearity of the fracture process zone in the context of LEFM, the equivalent crack length model can be used, where the fracture process zone and the traction free crack are considered together as an equivalent crack. According

to the behavior predicted by LEFM, the propagation of the traction free crack begins at peak load, after which the specimen begins to unload.

However, Fakhimi et al. (2017) and Lin et al. (2019) reported the presence of a traction free length in the specimen before peak load was reached. An explanation to this can be reached by considering the geometry of the notch and the grain size of the specimen. The notch tip is typically considerably wider than the average grain size. The bonding between the grains is much weaker than the actual grains so the fracture generally propagates in a tortuous path along the grain boundaries. It is possible for micro-cracks to generate on the notch tip before peak load because there are contacts to grain boundaries along it and the fracture will initiate where most favorable conditions occur. It is possible that the traction free crack begins to propagate and the load to continue to increase. For instance, if the crack is propagating along the grain boundaries, and as it propagates the crack tip is arrested by a grain, more load will be needed for it to continue propagating. Figure 4.10 from Parisio et al. (2019) shows a microphotograph of a fracture propagating in Adelaide Black granite. It can be observed that the fracture propagates along grain boundaries but also through grains. Numerical simulations (Galouei and Fakhimi 2015, Fakhimi and Wan 2016) have also shown that a traction free crack can develop before peak load when the rock matrix is modeled as a system of bonded particles.

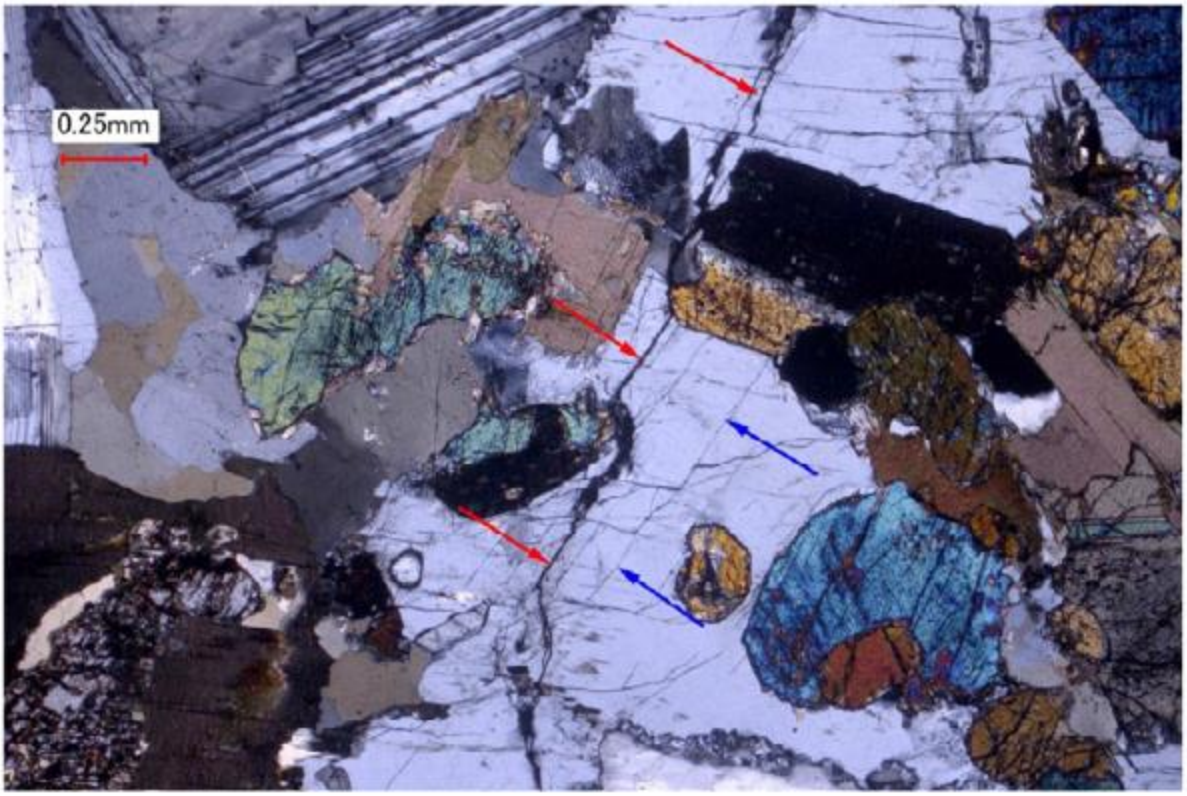

Figure 4.10: Microphotograph Adelaide Black granite showing a fracture that propagated along grain boundaries and through grains (adopted from Parisio et al. 2019).

There is an ongoing debate in the scientific literature on whether or not a traction free crack can develop during the pre peak loading regime. In this section, the results will be interpreted under the assumption that it is, in fact, possible for a traction free crack to form before reaching peak load (Lin et al. 2019).

Using DIC, the horizontal displacement can be calculated along the surface of notched specimens undergoing three or four-point bending throughout the different stages of loading. As explained before, the DIC method calculates the displacement at the center of small regions called subsets. The displacement gradient, g_{xx}, at any given position is defined using the finite difference method seen in Equation 4.4.

$$g_{xx} = \frac{\partial u}{\partial x} = \frac{u(i, j+1) - u(i, j-1)}{2d} \tag{4.4}$$

where *u(i, j)* is the subset or point where the horizontal displacement gradient is being calculated and *d* is the distance between subset centers.

Due to the geometry and loading conditions of the tests and the stress concentration caused by the notch tip, the specimen experiences tensile stress in the central region above the notch tip. This region can be subdivided into horizontal cross sections and it is assumed that a uniform tensile stress is acting along each one of them. The horizontal displacement can be plotted along the cross sections at different distances from the notch tip in the region of interest. The displacement patterns are affected by the propagating fracture and the choice of reference loading that is being used, as a result, they can be utilized to obtain information about the fracture. Figure 4.11 shows a typical three-point bending geometry, the region in the dotted line is where the specimen is experiencing tension at some stage of loading and the horizontal displacement can be plotted along horizontal cross sections within this region as shown by the dotted horizontal lines.

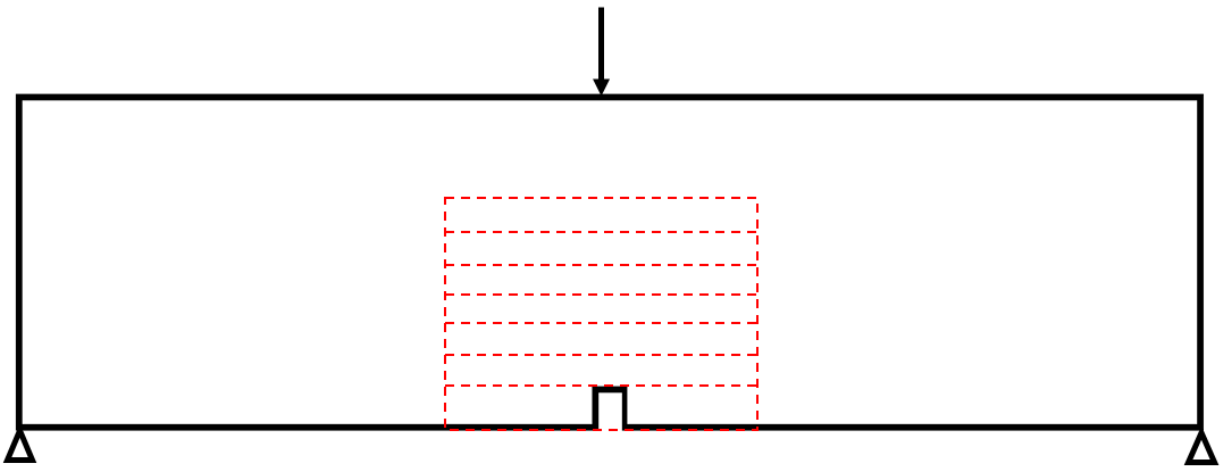

Figure 4.11: Typical testing geometry and the region of interest where the displacement is calculated at cross sections at different distances from the notch tip.

Figure 4.12 shows an example of how the horizontal displacement profiles change with increasing distance from the notch tip.

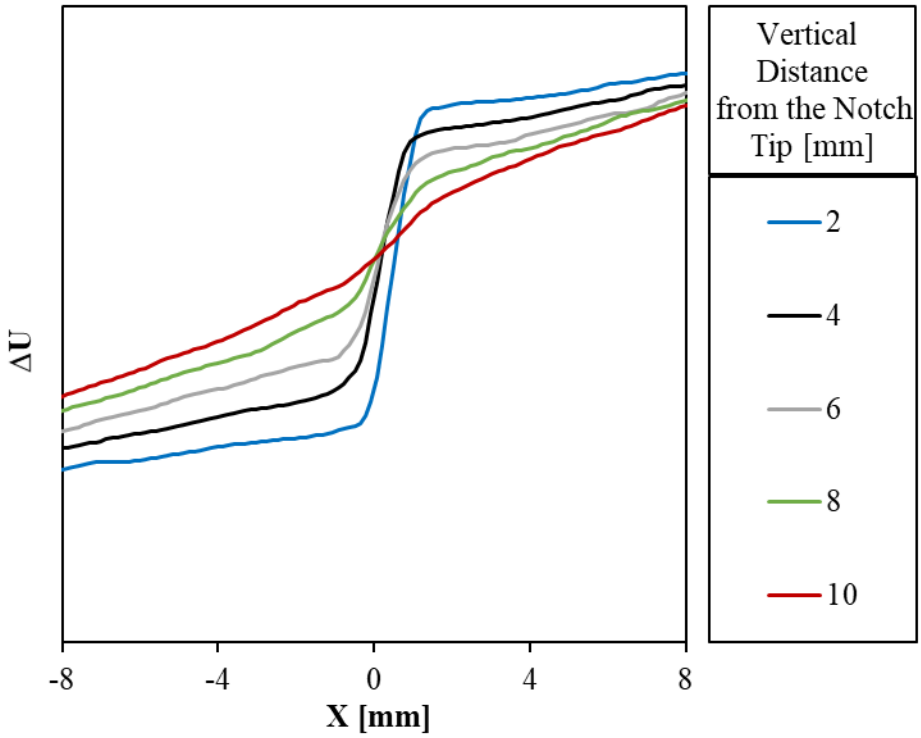

Figure 4.12: Horizontal displacement profile at different vertical distances from the notch tip for the Berea sandstone specimen.

Distinct patterns of horizontal displacement are observed at the horizontal cross sections at different distances from the notch tip or the crack tip. The patterns that are observed are highly dependent on the reference and current load that was used in the calculation. As explained in Lin et al. (2019) three main displacement patterns can be observed:

- Pattern I: The gradient g_{xx} of the horizontal displacement is positive, this is observed because the specimen is experiencing tensile loading in that region. The stress concentration of the notch and crack tip cause the tensile load to be grater in the center resulting in a higher horizontal displacement gradient g_{xx}.

- Pattern II: g_{xx} is strongly positive in the center and it is observed that $g_{xx} \approx 0$ on the sides of the observation zone. When the reference load is in the initial (unloaded) condition, pattern II is indicative of a traction free crack because no load is being carried by the material at either side of the crack resulting in $g_{xx} \approx 0$. When the reference loading is close to peak load in the pre peak regime (in this study 90% of peak load is used), the transition of pattern III to pattern II indicates the tip of the fracture process zone.
- Pattern III: The gradient in the center is largely positive for the same reason as in pattern I and II, however the positive region is surrounded by small regions where g_{xx} is negative. The negative region of g_{xx} suggests the development of material softening as a result of the concentrated damage within the fracture process zone. Pattern III is only observed when the reference load is close to the peak load.

The displacement patterns that are observed are dependent on the reference loading. Figure 4.13 shows the displacement patterns that occur when the reference loading is the initial or unloaded condition. Figure 4.14 shows the displacement patterns observed when the reference loading is close to the current load.

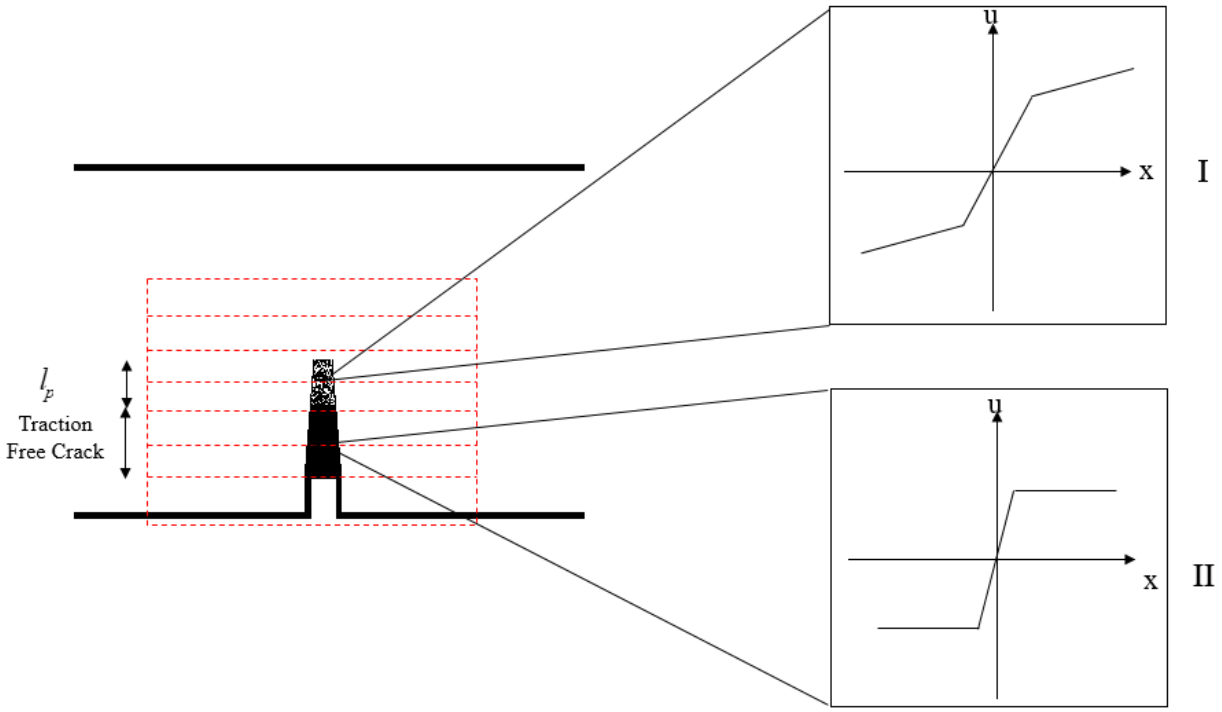

Figure 4.13: Displacement patterns observed when the reference load is the unloaded condition.

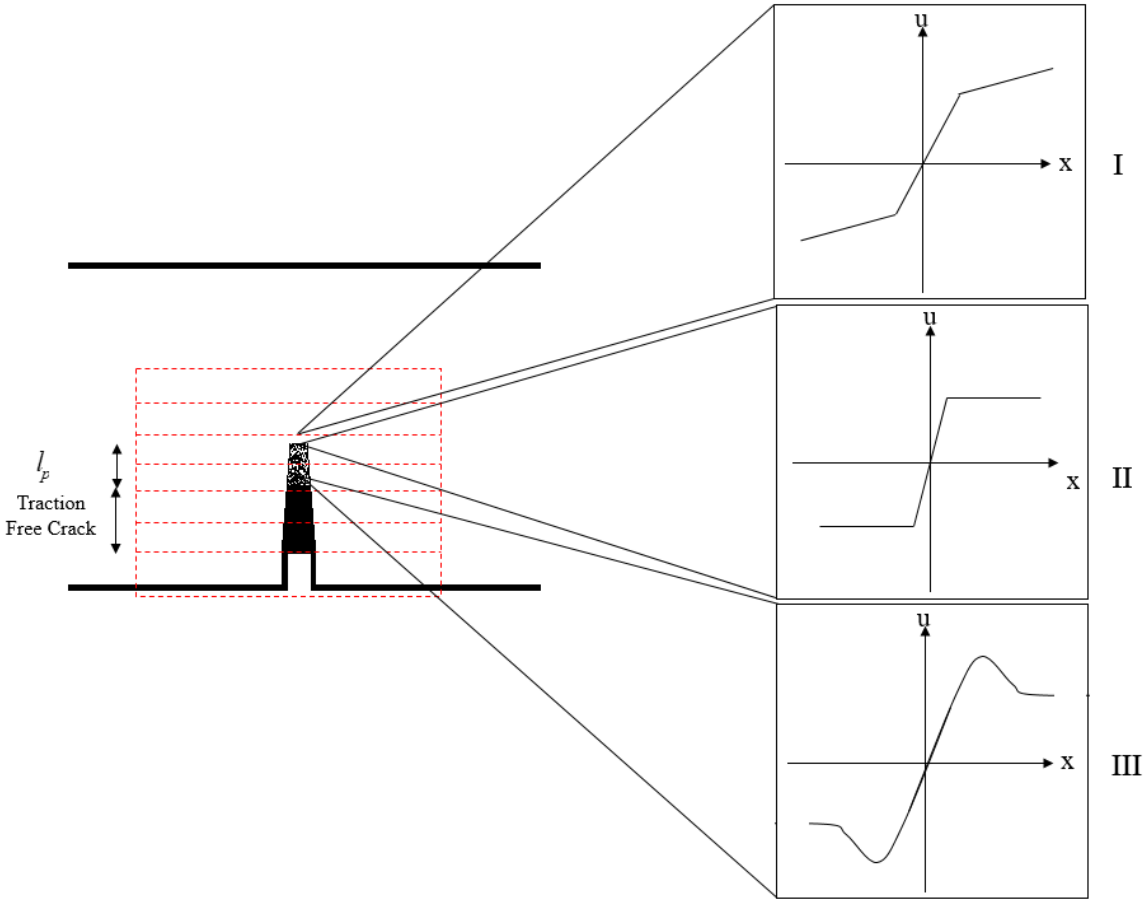

Figure 4.14: Displacement patterns observed when the reference load is close in magnitude (around 10% less) of the current load.

The displacements that are being analyzed are the incremental surface displacements that occur from the reference load to the current load. The profile of the opening displacements is dependent in the reference loading and the current loading that are chosen to carry out the analysis. The analysis is performed in both the pre peak and post peak regimes.

Pre Peak Regime Analysis

Figure 4.15 shows the displacement contours and related displacement gradients for the Berea sandstone specimen using the initial conditions (unloaded) as the reference load and the peak load as the current load. The displacement profile on the notch tip is observed to follow pattern II. The fact that the displacement follows pattern II is indicative that a traction free crack has already formed at peak load (the current load); $g_{xx} \approx 0$ indicates that no load is being carried by the material on the sides of the crack. The end of the cohesionless crack is found at the point where the displacement pattern transitions from pattern II to pattern I, which happens at 2.5 mm above the notch tip.

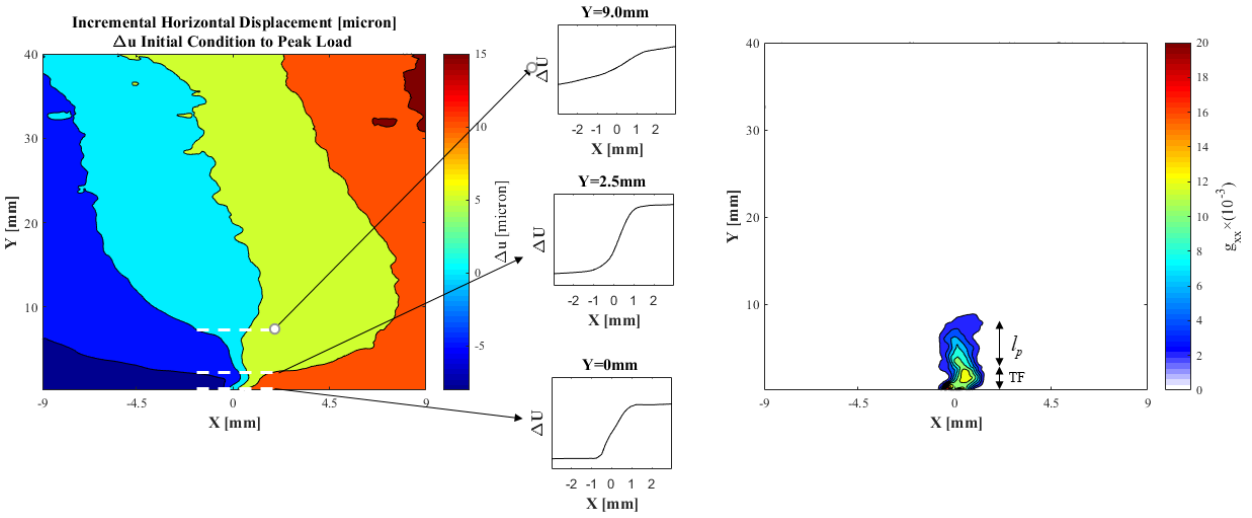

Figure 4.15: Displacement contours from the unloaded condition to peak load, displacement patterns at different distances from the notch tip and the contour of the displacement gradient.

By using the displacement from the initial conditions to peak load, it was determined that the traction free length extends from the notch tip to 2.5 mm from the notch tip. The fracture process zone starts where the traction free crack ends. To find the tip of the fracture process zone the incremental displacements from a reference load that is closer to the peak load are analyzed. Therefore, the displacements are analyzed starting from 2.5 mm from the notch tip using a

reference load that is close to peak load as observed in Figure 4.16. Pattern III can be observed on this region, the negative sections of the displacement gradient indicate material softening characteristic of the fracture process zone. The tip of the fracture process zone is located where pattern III transitions to pattern II. This happens at 8.5 mm from the notch tip for the Berea sandstone specimen, indicating that the process zone developed at peak load is approximately 6 mm long. Interestingly, the tip of the process zone is close to or at the point where the displacement contours merge. The contour of the displacement gradient shows that unloading of the material occurs to the sides of the fracture from 90% peak load to peak load. It is important to point out that the results may vary slightly depending on which loading stage is chosen as the reference load.

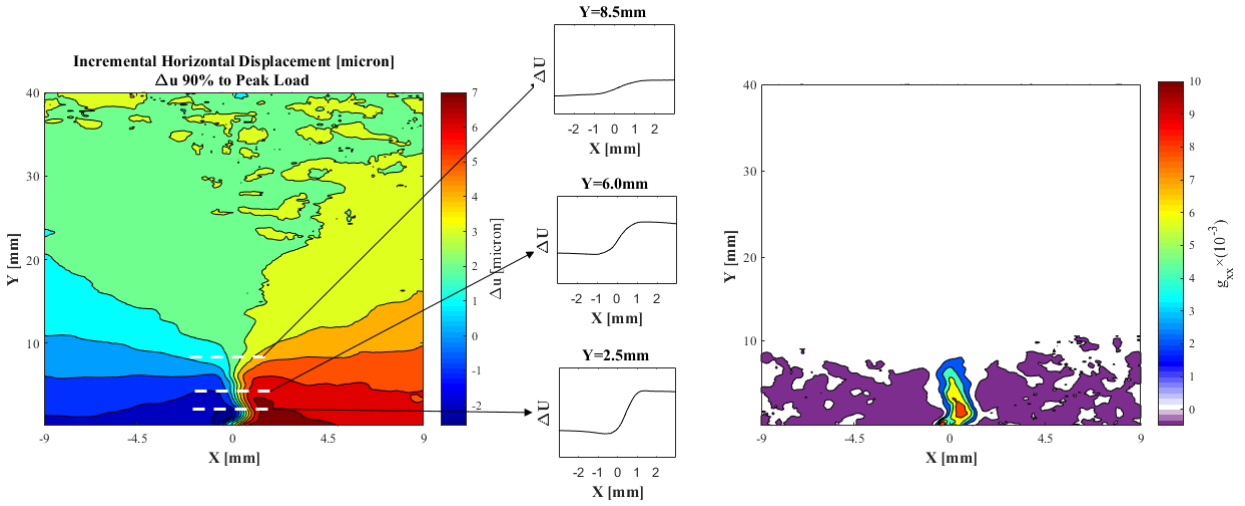

Figure 4.16: Displacement contours from the 90% peak load to peak load, displacement patterns at different distances from the notch tip and the contour of the displacement gradient.

Post Peak Regime Analysis

For the post peak regime the reference load will only be the initial condition. Global unloading during the post peak regime makes the determination of the boundary of the fracture process zone and the elastic region unclear, so the incremental displacements from other loading stages are not considered. Regardless, it is possible to determine the length of the traction free crack in a similar fashion to how it is done in the pre peak regime.

Figure 4.17 shows the displacement contours from initial conditions to different stages of post peak loading. The tip of the traction free crack is interpreted to be at the point where the displacement patterns transition from pattern I to pattern III. For Berea sandstone, this happens at 5.5 mm from the notch tip at the 90% post peak loading stage and at 8.5 mm from the notch tip at the 80% post peak loading stage.

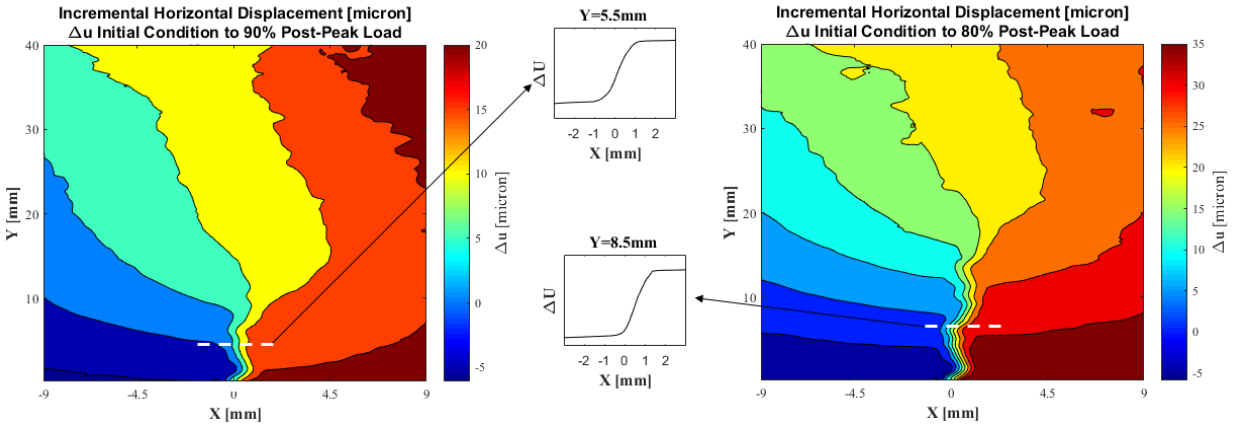

Figure 4.17: Displacement contours from the unloaded condition to 90% post peak load, displacement patterns at different distances from the notch tip and the contour of the displacement gradient.

Calculating the Width of the Fracture Process Zone Using DIC

The inelastic processes that occur in the fracture process zone such as material softening and damage localization cause the horizontal displacement gradient to be affected within this region. When the horizontal displacement gradient is plotted in a cross section that includes the fracture process zone, it is observed that the gradient of the horizontal displacement is greater inside the fracture process zone. The change in the displacement gradient is indicative of the presence of the fracture process zone. The length of the process zone is interpreted as the area where the horizontal displacement gradient is affected at the midpoint of the length of the process zone at peak load using the unloaded condition as the reference load. The inflection points observed in the gradient that enclose the section, where the displacement gradient has a higher value, delimit this area. The inflection points indicate a change in regime in the displacement resulting from the effects the characteristic mechanisms of the fracture process zone have on the surface displacement of the specimen. Figure 4.18 shows the horizontal displacement profile in the middle of the fracture process zone at peak load for the Berea sandstone specimen and the dotted red lines indicate what is interpreted to be the width of the fracture process zone.

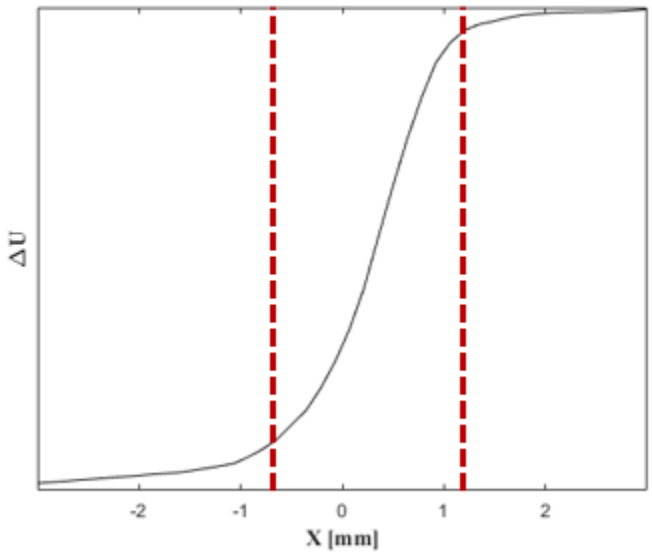

Figure 4.18: The horizontal displacement gradient plotted at half the length of the fracture process zone at peak load for the Berea sandstone specimen.

An alternative method to calculate the width of the fracture process zone is proposed using the vertical surface displacement of the specimen. In a similar way to how the horizontal displacement profiles are affected by the presence of the fracture and the fracture process zone, it is observed that the vertical displacement profiles are affected as well. The vertical displacement profiles can be plotted at different horizontal distances from the notch as shown in Figure 4.19. It can be seen that the displacement profiles that are near the notch are affected by the fracture process and, as the distance from the notch increases, the displacement profiles converge into an approximately uniform pattern.

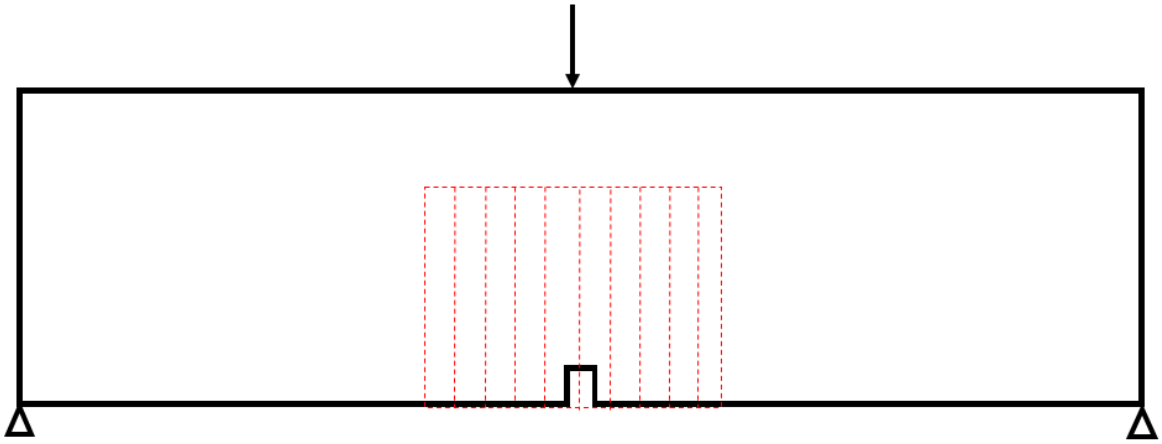

Figure 4.19: Typical testing geometry and the region of interest where the displacement is calculated at vertical cross sections at different horizontal distances from the notch tip.

Figure 4.20 shows the plots for the vertical displacement profiles at different distances from the notch tip for the Berea sandstone specimen. The profiles that are close to the notch have an initial negative slope. The slope of the vertical profiles is affected by the mechanisms that are characteristic of the fracture process zone such as material softening and yielding. The half-length of the fracture process zone is interpreted to be the horizontal distance from the notch tip where the vertical displacement profile no longer exhibits the change of slope resulting from the presence of the fracture process zone.

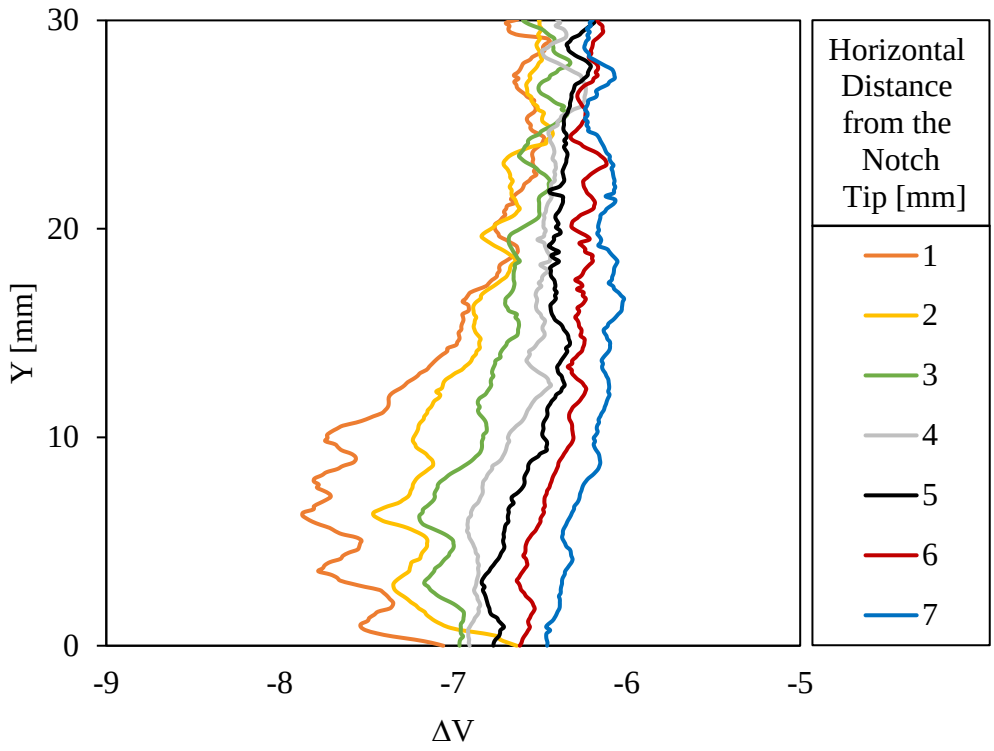

Figure 4.20: Vertical displacement profiles at different horizontal distances from the notch tip for the Berea sandstone specimen.

CHAPTER 5: RESULTS AND DISCUSSION

Adelaide Black Granite

Five Adelaide Black granite specimens were tested under three-point bending loading conditions. The calculated nominal strength and the apparent fracture toughness for each specimen are displayed in Table 5.1.

Table 5.1: Nominal strength and apparent fracture toughness of the Adelaide granite specimens.

Specimen	D	σ_n	K_{ICA}
	[mm]	**[kN]**	**[MPa·m$^{0.5}$]**
ABG1	43	16.90	1.41
ABG2	48	16.15	1.44
ABG3	68	15.32	1.54
ABG4	35	16.48	1.35
ABG5	39	13.37	1.40

The apparent fracture toughness was calculated for each Adelaide Black granite specimen using Equation 3.3 and the fracture toughness was calculated using the linear regression method #1 as observed in Figure 5.1.

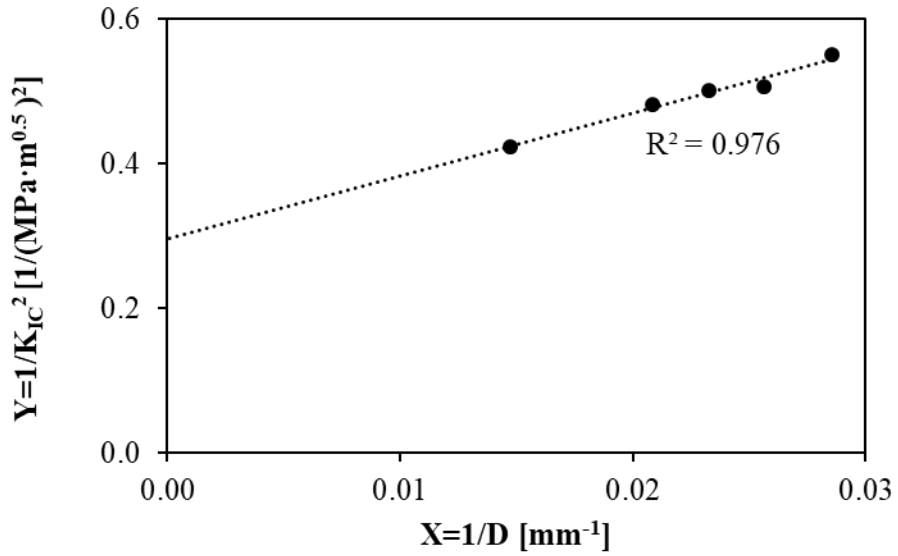

Figure 5.1: Linear regression for the calculation of the fracture toughness of Adelaide Black granite.

The fracture toughness of Adelaide Black granite was found to be 1.9 ±0.1 MPa·$m^{0.5}$. As expected, a significant size effect was observed on the fracture toughness in Adelaide Black granite: larger specimens have a greater fracture toughness that is closer to the value predicted by LEFM.

In order to predict the behavior of Adelaide Black granite specimens of different sizes, the nominal strength for each specimen was calculated and the average values of the parameters to plot Bazant's size effect law were obtained using the linear regression methods #2 and #3: D_0=189.2 mm and Bf'_t=17.9 MPa. Bazant's size effect law predicts the nominal strength and the type of failure regime as a function of specimen size. Bazant's size effect law was plotted for Adelaide Black granite and is shown in Figure 5.3. Larger specimens behave as predicted by LEFM while small specimens tend to follow the plasticity or strength criterion. As predicted, the specimens that were tested for this study fell under the transition region in Bazant's size effect law, showing a significant deviation from behavior predicted by LEFM.

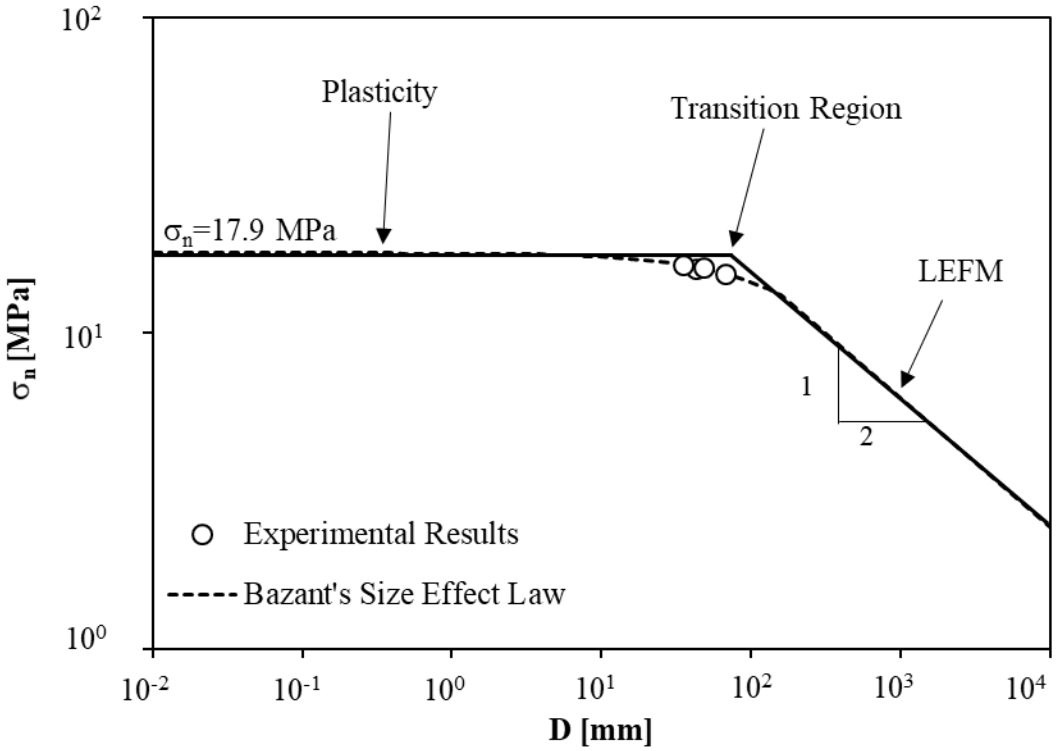

Figure 5.2: Bazant's size effect law plotted based on experiments performed on Adelaide Black granite specimens.

It was not possible to calculate the dimensions of the fracture process zone for specimens ABG2 and ABG4. There were some connectivity issues with the camera during the testing of specimen ABG2 and no data could be recovered to perform an analysis using DIC. The main challenge of using DIC with Adelaide Black granite is high stiffness of the material that results in extremely small displacements (in the order of fractions of microns to microns) during the fracturing process, which are difficult to capture with the digital camera and the resolution of the DIC algorithm. The incremental displacements in the ABG4 test, which was the smallest Adelaide Black granite specimen, only fractions of microns, and it was not possible to analyze incremental displacements for different stages of loading at this resolution. Consequently, the dimensions of the fracture process zone could not be calculated for specimen ABG4. However, this result

provides interesting insight on the nature of size dependence in Adelaide Black granite, the amount of displacement specimen of different sizes experience during fracture, and the challenges of the applicability of DIC on crystalline rocks. The analysis of the size dependence of the dimensions of the fracture process zone was carried out for the remaining Adelaide Black granite specimens.

The length of the fracture process zone was calculated with DIC using the two methods introduced, the Critical Displacement Method and the Displacement Gradient Method. Figure 5.3 shows the linear regression method used to obtain the parameters needed to predict the length of the process zone as a function of specimen size in Adelaide Black granite.

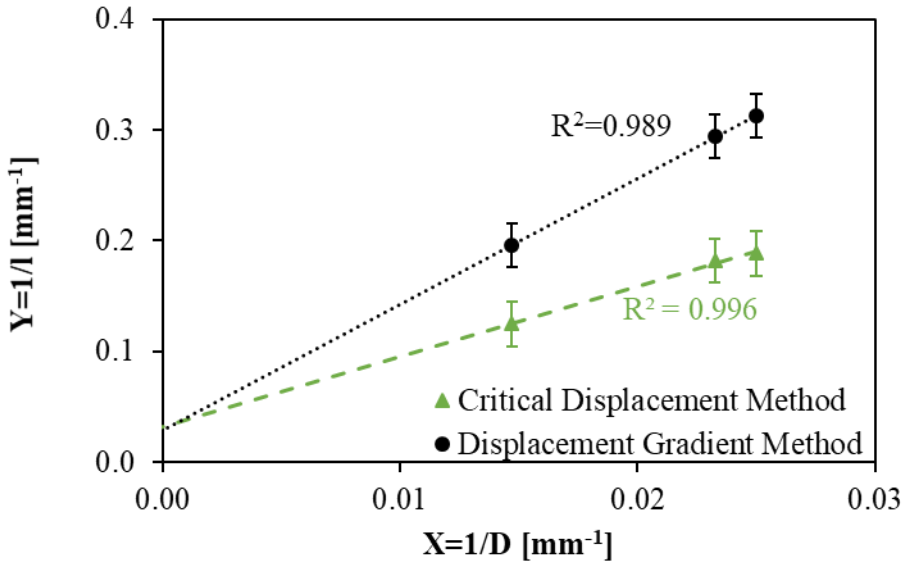

Figure 5.3: Linear regressions for the length of the fracture process zone plotted as a function of specimen size for the Adelaide Black granite specimens.

The linear regressions were used to obtain the parameters needed for equation 2.6 to predict the length of the fracture process zone as a function of specimen size. Figure 5.4 shows the prediction for the length of the fracture process zone compared to the experimental results for both methods that were used to calculate it.

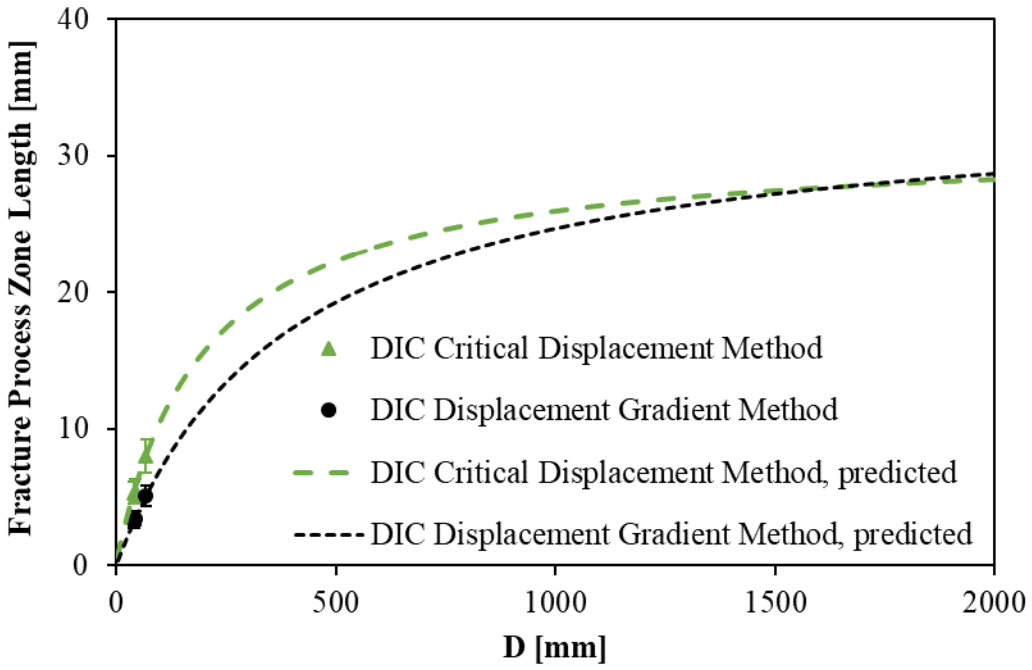

Figure 5.4: Experimental results and theoretical prediction for the length of the fracture process zone in Adelaide Black granite calculated using DIC with two different methods.

The width of the fracture process zone was also calculated using DIC. The results were used to perform a linear regression as shown in Figure 5.5 and calculate the necessary parameters for predicting the width of the fracture process zone as a function of specimen size (Equation 2.7).

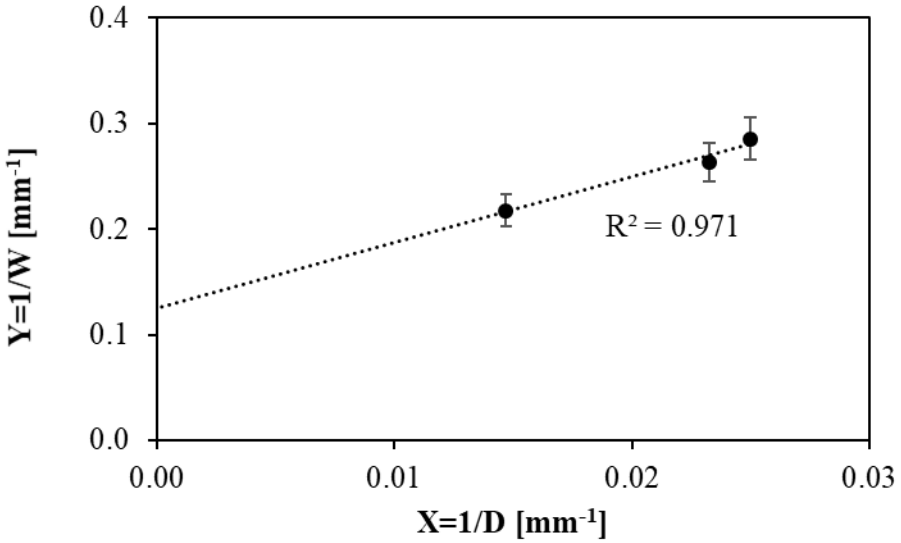

Figure 5.5: The width of the fracture process zone plotted as a function of specimen size for the Adelaide Black granite specimens.

Figure 5.6 shows the predicted value for the width of the process zone compared to the experimental results.

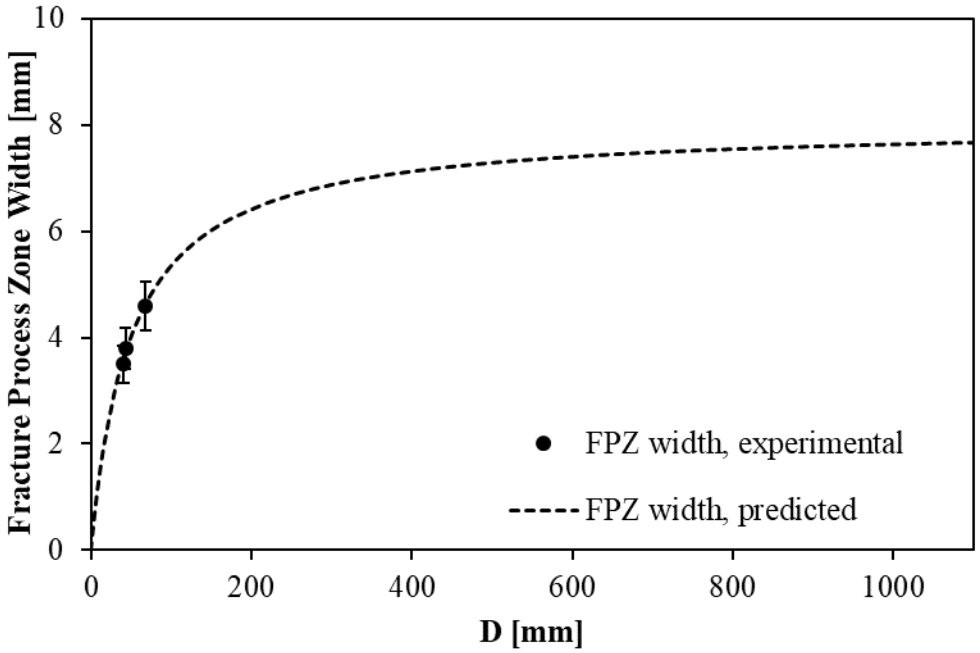

Figure 5.6: Experimental results and theoretical prediction for the width of the fracture process zone in Adelaide Black granite.

The calculated dimensions of the fracture process zone of the Adelaide Black granite specimens and the predicted fracture process zone size for an infinitely large specimen are

displayed in Table 5.2. These results are compared with the values obtained using acoustic emission (AE) method provided by Parisio et al. (2019) for the same rock. It can be seen that experimental results and the predicted value for the size of the fracture process zone in an infinitely large specimen are in reasonable agreement for both types of measurements. The fact that results obtained using acoustic emission are similar to those calculated using DIC is an important step in the validation of the use of DIC to calculate the dimensions of the fracture process zone in crystalline rocks.

A significant advantage of DIC is that it is possible to calculate continuous surface displacements throughout the entire experiment; on the other hand, with AE, only discrete events are recorded. With AE it is necessary to interpolate the information from individual events at a certain distance from each other while DIC allows for the continuous measurement of surface displacement. The fact that continuous measurements are possible using DIC allows for the measurement of the fracture process zone at greater resolution.

Table 5.2: Experimentally obtained and predicted dimensions of the fracture process zone using DIC compared to values obtained using Acoustic Emission in Adelaide Black granite.

DIC				**AE (Parisio et al. 2019)**		
D	**FPZ Length**	**FPZ Length**	**FPZ Width**	***D***	**FPZ Length**	**FPZ Width**
	Critical Displacement Method	**Displacement Gradient Method**				
[mm]	[mm]	[mm]	[mm]	[mm]	[mm]	[mm]
40	5.3	3.2	3.5	30.6	4.3, 4.6	4.1, 4.3
43	5.5	3.4	3.8	44.7	5.5, 5.9	4.6, 4.8
68	8.0	5.1	4.6	67.1	9.3	5.0
∞	31.0 ±1.9	34.3 ±2.1	7.3 ±0.5	∞	36.8	6.1

Charcoal Granite

Six Charcoal granite specimens were tested using three-point bending and six specimens were tested using four-point bending loading conditions. The calculated nominal strength and apparent fracture toughness for each Charcoal granite specimen can be observed in Table 5.3.

Table 5.3: Nominal strength and apparent fracture toughness of the Charcoal granite specimens.

Method	**Specimen**	***D***	σ_n	K_{IC}
		[mm]	**[MPa]**	**[MPa·m$^{0.5}$]**
Three-point bending	CGA1	25.4	11.56	1.06
	CGA2	25.4	10.73	1.02
	CGA3	50.8	8.49	1.17
	CGA4	50.8	8.8	1.21
	CGA5	101.6	6.37	1.25
	CGA6	101.6	6.69	1.29
Four-point bending	CGB1	25.4	8.38	0.70
	CGB2	25.4	7.71	0.69
	CGB3	50.8	7.85	0.86
	CGB4	50.8	7.7	0.91
	CGB5	101.6	6.38	1.01
	CGB6	101.6	6.14	0.97

The apparent fracture toughness of each Charcoal granite specimen was used to perform the linear regression method #1 as observed in Figure 5.7 in order to calculate the fracture toughness of Charcoal granite.

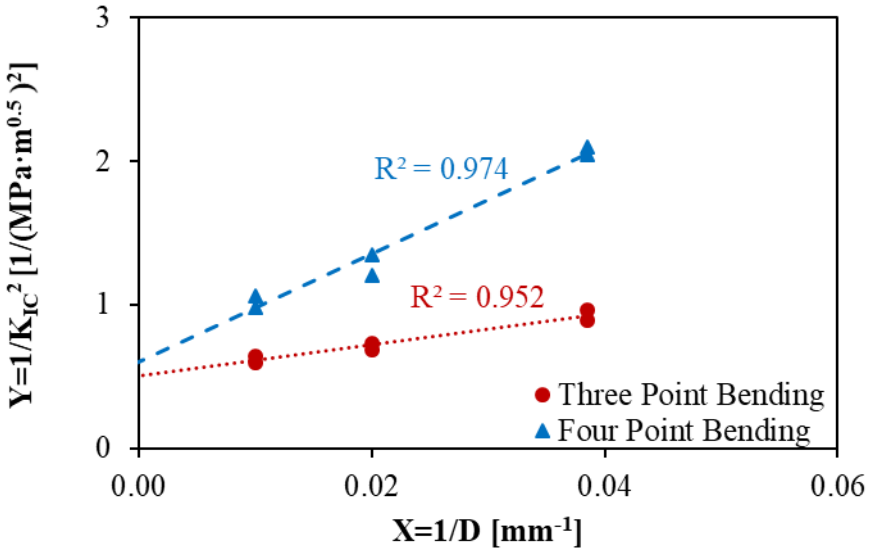

Figure 5.7: Linear regression using the apparent fracture toughness of each Charcoal granite specimen used to calculate the real fracture toughness.

As seen in Figure 5.7, the apparent fracture toughness in Charcoal granite shows a clear dependence on specimen size for both loading conditions. As predicted, as the specimen gets larger, its fracture toughness comes closer to the value predicted by LEFM. The calculated fracture toughness for Charcoal granite is 1.4±0.1 MPa·$m^{0.5}$ for the specimens tested under three-point bending and 1.3±0.1 MPa·$m^{0.5}$ for the specimens tested under four-point bending, both calculated values are in reasonable agreement.

The nominal strength of each specimen was measured and used to obtain the parameters necessary to calculate the nominal strength as a function of specimen size using Bazant's size effect law. The two linear regression methods used to calculate the size effect parameters can be seen in Figure 5.8.

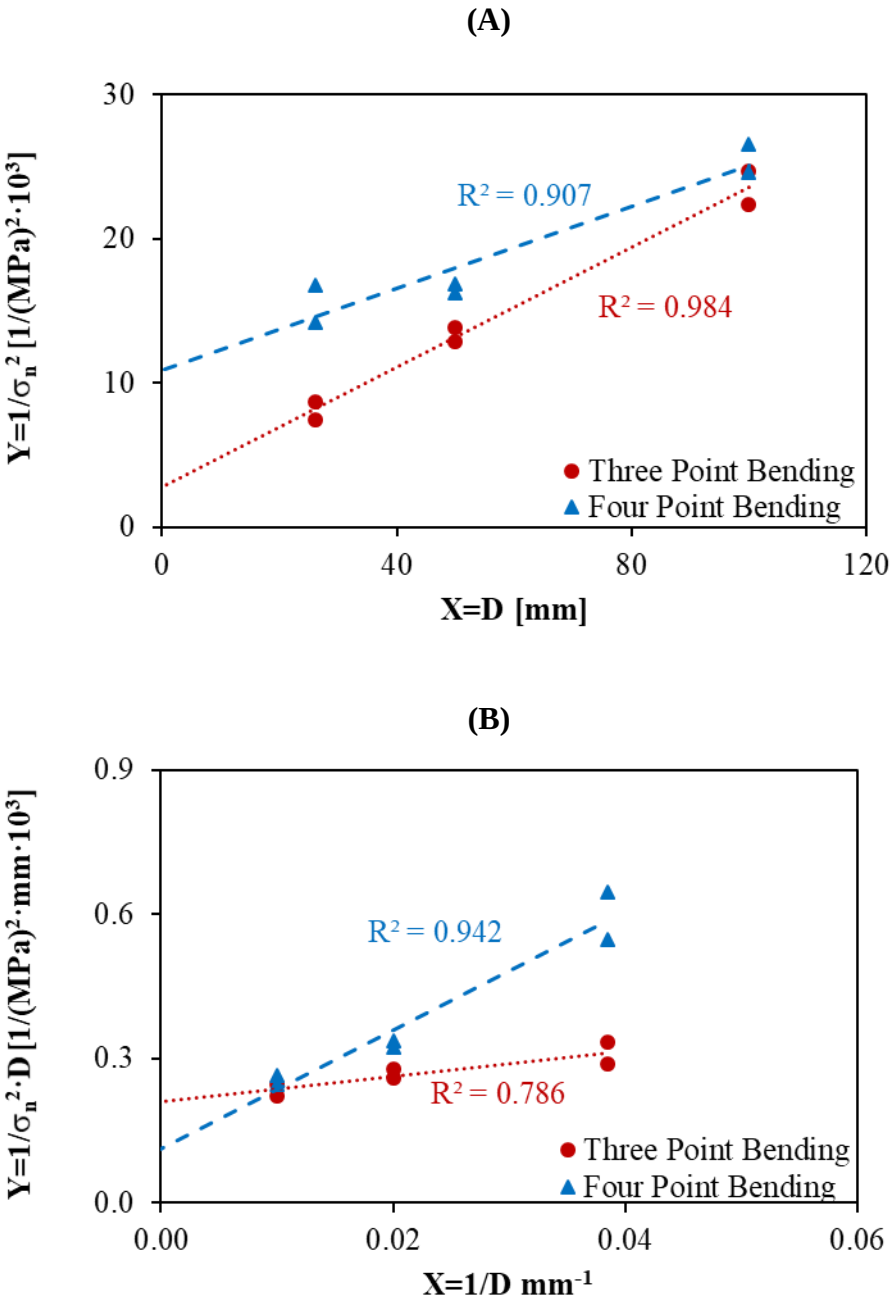

Figure 5.8: Linear regressions used to obtain the necessary parameters for Bazant's size effect law for Charcoal granite using (A) linear regression method #1 and (B) linear regression method #2.

The average values for the parameters for Bazant's size effect law for Charcoal granite calculated from the linear regressions are displayed in Table 5.4 and the data is shown in Figure 5.9.

Table 5.4: Parameters for Bazant's size effect law for Charcoal granite.

Method	D_o	$Bf'(t)$
	[mm]	**[MPa]**
Three-Point Bending	13.0	19.1
Four-Point Bending	92.5	9.3

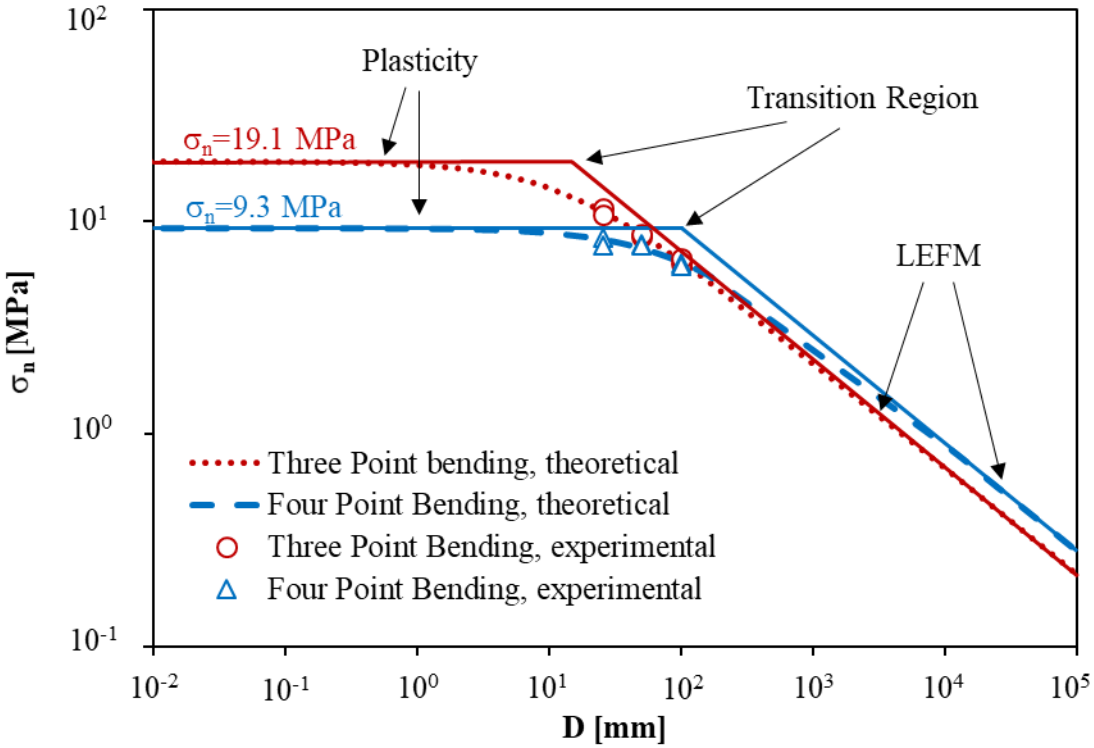

Figure 5.9: Bazant's size effect law for Charcoal granite specimens under three and four-point bending loading conditions.

Figure 5.9 shows the significant size dependence of the nominal strength in Charcoal granite. As expected, the nominal strength for all the specimens tested using four-point bending was lower than for specimens of the same size tested using three-point bending. The reason that this result was expected, as explained in ASTM C1161-13, is that in the three-point bending

configuration, only a small portion of the specimen is exposed to the maximum stress, as opossed to four-point bending where this occurs along the entire length of the inner span. This causes the nominal and flexural strength to be lower in specimens tested using four-point bending when compared to three-point bending.

The length of the fracture process zone was calculated for each Charcoal granite specimen through DIC utilizing the two methods that were outlined in the corresponding chapter. The calculated length of the fracture process zone for all the specimens was used to obtain the parameters needed for Equation 2.6 in order to predict the length of the fracture process zone as a function of specimen size. This was done by performing linear regressions and using the fitting squares method as explained in the corresponding section. Figure 5.10 (A) shows the linear regression method for the calculated lengths of the fracture process zone in Charcoal granite using the Critical Displacement and the Displacement Gradient Method and Figure 5.10 (B) for the specimens tested using four-point bending.

Using the linear regressions shown in Figure 5.10, it was possible to calculate the parameters needed to predict the length of the fracture process zone as a function of specimen size using equation 2.6. Figure 5.11 shows the experimental results and the theoretical prediction for the length of the the fracture process zone in Charcoal granite: Figure 5.11 (A) shows the result for the three-point bending tests while Figure 5.11 (B) shows the results for the four point bending tests.

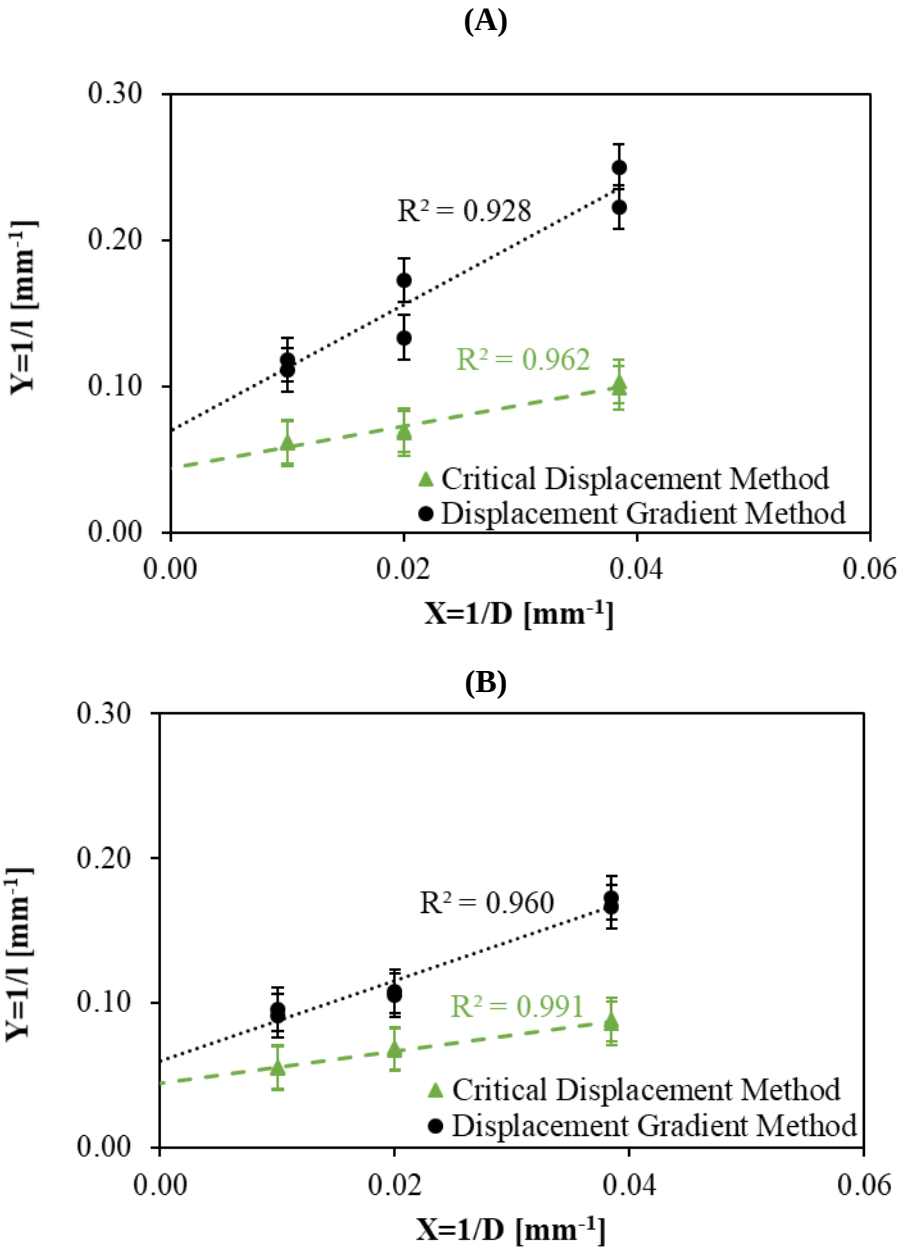

Figure 5.10: Linear regression methods used to obtain parameters needed to calculate the length of the process zone in Charcoal granite as a function of specimen size for specimens tested under (A) three-point bending (B) four-point bending.

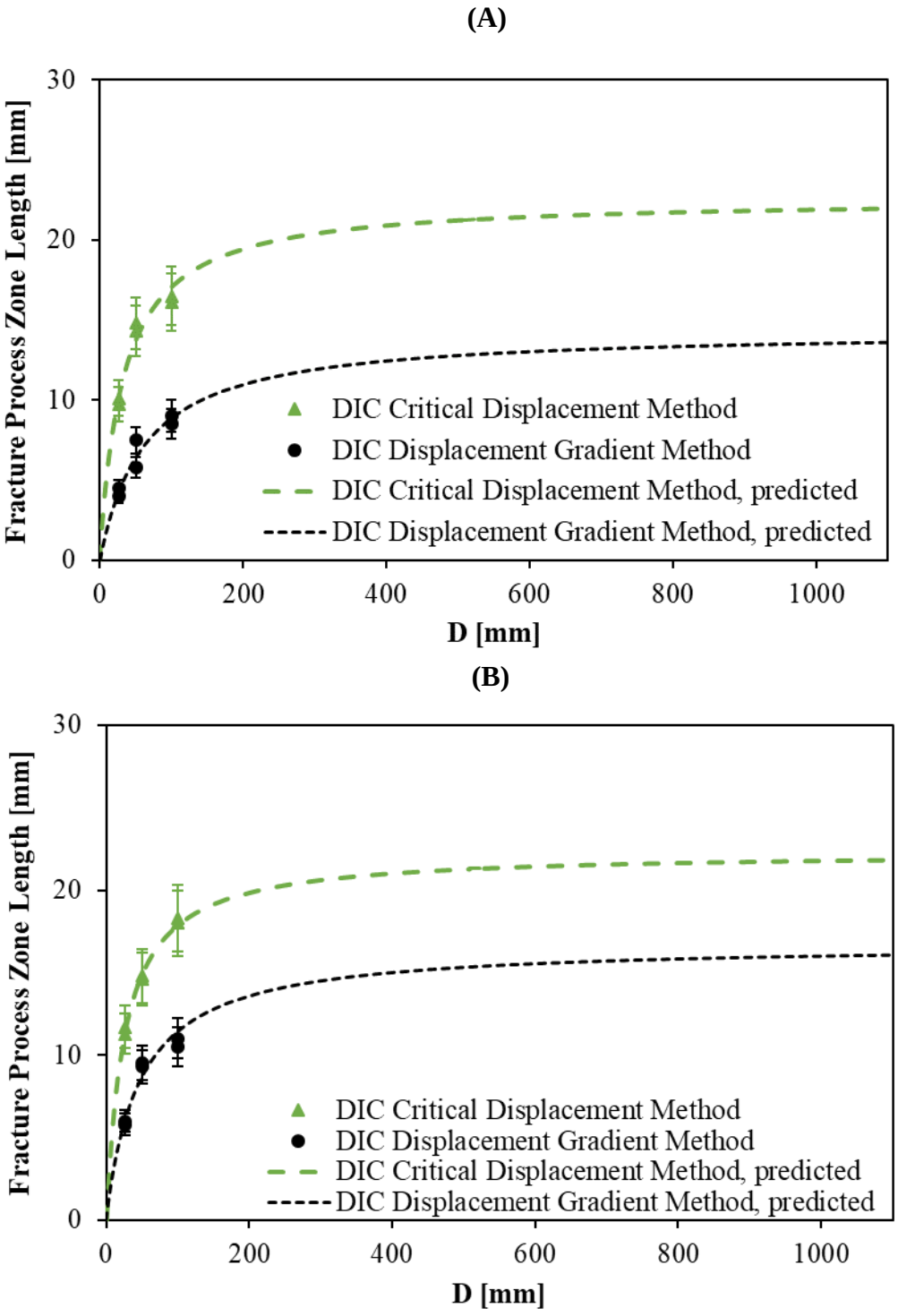

Figure 5.11: Experimental results and theoretical prediction for the length of the fracture process zone in Charcoal granite calculated using DIC with two different methods under (A) three-point bending and (B) four-point bending loading conditions.

It can be observed that for both three and four-point bending experiments and theoretical predictions, the length of the process zone calculated using the Critical Displacement Method is larger than that calculated using the Displacement Gradient Method. The main difference between the two methods is that the Critical Displacement Method assumes that there is no propagation of a traction free crack before peak load, while the Displacement Gradient Method assumes that it is possible. Figure 5.4 shows that the predicted length of the fracture process zone for large specimen sizes of Adelaide Black granite using both methods is very similar, but as seen in Figure 5.10, this is not the case for Charcoal granite. Future work is needed with more materials, specimen geometries, and loading conditions in order to investigate the cause of this effect, which is related to the propagation, or lack thereof, of a traction free crack in the pre peak regime.

A main objective of this study is to investigate how the dimensions of the fracture process zone are affected by the two kinds of loading conditions provided by three and four-point bending. A comparisson of the calculated and predicted lengths of the fracture process zone in both loading regimes was carried out. Figure 5.12 (A) compares the results for the length of the fracture process zone for specimens tested under three and four-point bending, when the fracture process zone is calculated using the Critical Displacement Method. Figure 5.12 (B) shows the same comparison but when the length of the fracture process zone is calculated using the Displacement Gradient Method.

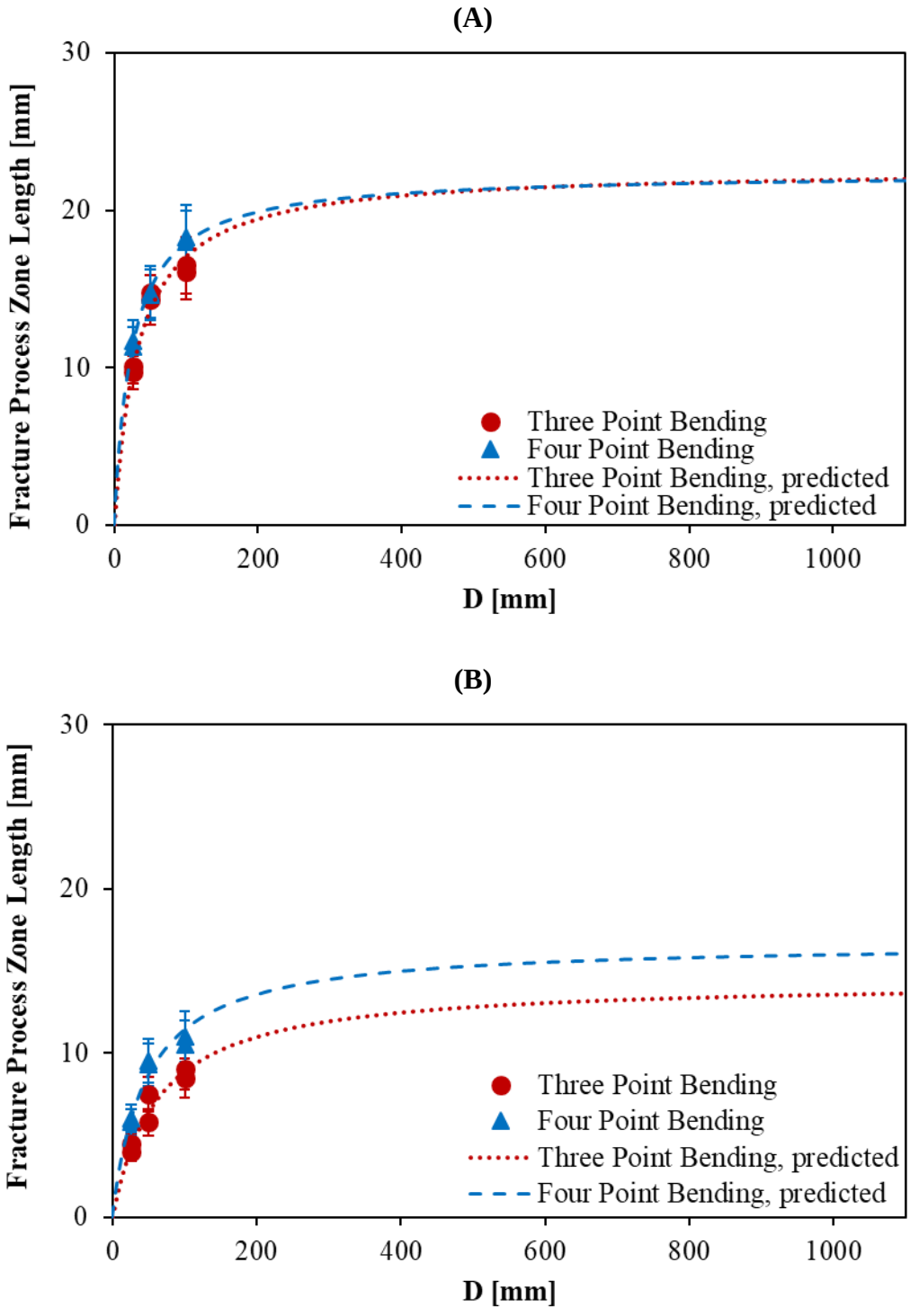

Figure 5.12: Comparison of experimental results and theoretical prediction for the length of the fracture process zone in Charcoal granite for specimens under three and four-point bending loading conditions. The fracture process zone was calculated using (A) the Critical Displacement DIC method and (B) the Displacement Gradient DIC method.

For the specimen sizes that were tested in the laboratory, when the Critical Displacement DIC method is used to calculate the length of the fracture process zone, the observed length of the fracture process zone is larger in the specimens tested using four-point bending when compared to three-point bending. However, the predicted length of the fracture process zone for an infinitely large specimen was very similar for both types of loading contions, 22.60 ±2.5 mm for three-point bending and 22.4 ±1.7 mm for four-point bending. A possible explanation is that in the three-point bending tests only a small region of the specimen is exposed to the maximum stress, but in infinitely large specimens, this region is large enough to encapsulate the facturing process in the local conditions that approach those of a four-point bending test, therefore yielding similar results.

Figure 5.11 (B) shows a comparison of the fracture process zone length calculated using the Displacement Gradient Method and the theoretical prediction of the fracture process zone length in Charcoal granite. Similarly to the results shown in Figure 5.11 (A), the calculated length of the fracture process zone for all the specimen sizes that were tested in the laboratory was larger in the four-point bending tests. However, in this case, the theoretical prediction for the length of the fracture process zone for larger and infinitley large specimens is that it will be larger for specimens under four-point bending loading conditions. The predicted lenghts of the fracture process zone for infinitely large specimens by using the Displacement Gradient DIC Method are 14.4 ±1.0 mm for three-point bending and 16.8 ±1.1 mm for four-point bending. This effect and the reason why the results are different is related to the possible propagation of a traction free crack before peak load. It would be apporpiate to further investigate this phenomenon with additional testing using more materials, loading conditions, and specimen geometries.

The width of the fracture process zone was calculated for each Chracoal granite specimen using DIC and the results were used to perform a linear regression in order to obtain the

parameters needed to calculate the width of the process zone as a function of specimen size according to equation 2.7. Figure 5.13 shows the linear regression used to calculate the parameters needed for equation 2.7. Figure 5.14 compares the experimental and predicted values for the width of the fracture process zone for three and four-point bending tests in Charcoal granite.

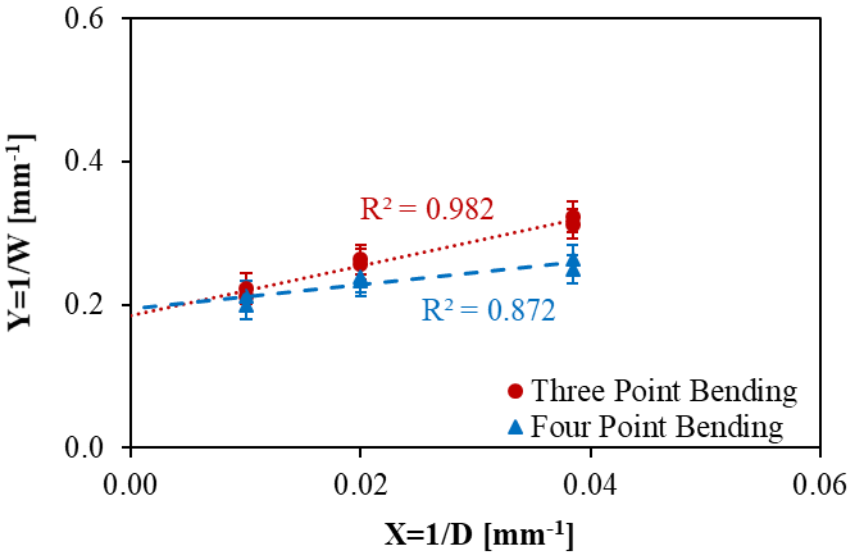

Figure 5.13: Linear regression using the width of the fracture process zone plotted as a function of specimen size for Charcoal granite specimens.

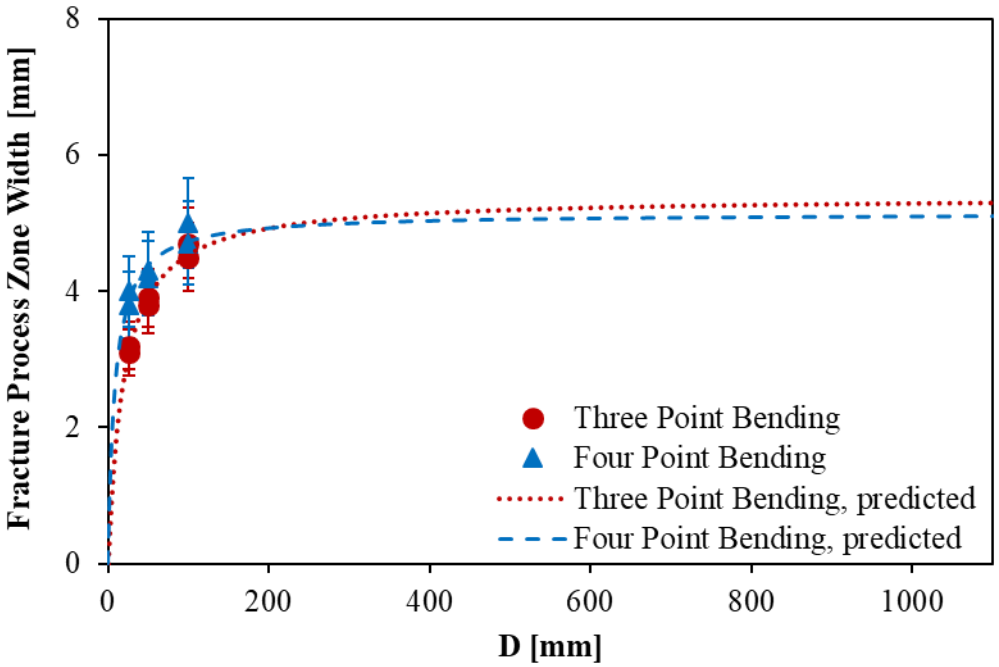

Figure 5.14: Experimental results and theoretical prediction for the width of the fracture process zone of Charcoal granite.

The width of the fracture process zone was observed to be larger in the specimens tested under four-point bending compared to same size specimens tested using three-point bending for all the tested specimen sizes. However, as observed in Figure 5.14, the predicted width of the fracture process zone for large and infinitely large specimens is very similar for specimens undergoing four and three-point bending loading conditions. The predicted width of the fracture process zone in an infinitely large Charcoal granite Specimen is 5.4 ±0.4 mm for three-point bending and 5.2 ±0.8 mm for four-point bending. A possible explanation is that for an infinite large specimen the local conditions where the fracture is propagating are similar for both kinds of loading regimes. In addition, as discussed by Wang et al. (1990) and Mihashi et al. (1991), the most dominant factor affecting the width of the fracture process zone is the grain or aggregate size. Considering that the tests were performed on the same material with the same grain size and grain size distribution, it is to be expected that the width of the process zone not to significantly deviate. Nonetheless, future work is recommended with additional tests using a wider array of specimen geometries and loading conditions. Summarizing, Table 5.5 displays the dimensions of the fracture process zone in Charcoal granite specimens of different sizes calculated using DIC.

Table 5.5: Fracture process zone dimensions in Charcoal granite calculated using DIC for specimens of different sizes and under three and four-point bending loading conditions.

	Three-point Bending			**Four-point Bending**		
D	**FPZ Length**	**FPZ Length**	**FPZ Width**	**FPZ Length**	**FPZ Length**	**FPZ Width**
	Critical Displacement Method	**Displacement Gradient Method**		**Critical Displacement Method**	**Displacement Gradient Method**	
[mm]	[mm]	[mm]	[mm]	[mm]	[mm]	[mm]
25.4	10.1, 9.7	4.0, 4.5	3.1, 3.2	11.3, 11.7	5.8, 6.0	3.8, 4.0
50.8	14.3, 14.8	5.8, 7.5	3.8, 3.9	14.6, 14.8	9.3, 9.5	4.2, 4.3
101.6	16.1, 16.5	8.5, 9.0	4.5, 4.7	18.0, 18.3	10.5, 11.0	4.7, 5.0
∞	22.60 ±2.5	14.4 ±1.0	5.4 ±0.4	22.4 ±1.7	16.8 ±1.1	5.2 ±0.8

CHAPTER 6: CONCLUSIONS

In this study, Digital Image Correlation (DIC) was utilized to investigate the dependence of the dimensions of the fracture process zone on the size and loading conditions of the specimen. The fracture process zone is involved in the initiation and propagation of fractures in rock. Its presence influences the behavior of rock during fracture and therefore it must be carefully investigated. DIC was used to measure the fracture process zone and to further understand how specimen size and loading conditions affect fracture behavior in two types of granitic specimens: Adelaide Black granite and Charcoal granite.

Detecting the fracture process zone in granite through the use of DIC is a challenging task since the surface displacements are extremely small during the fracture process. The width of the fracture process zone was measured using DIC and two different methods to calculate the length were carried out. One method assumes that there is no propagation of a traction free crack in the pre peak regime and the other one assumes that it is in fact possible. The dimensions of the fracture process zone that were measured using DIC in the Adelaide Black granite under three-point bending were compared to results from Parisio et al. (2019), where acoustic emission measurements were utilized. The results appear to be in reasonable agreement, which is an important step in verifying the measurements obtained through DIC in crystalline rocks, which appears to be a more accurate technique.

The dimensions of the fracture process zone display a clear dependence on specimen size within the size range that is typically used in laboratory experiments. It was observed that the size of the fracture process zone increases for larger specimen sizes and it is predicted that its dimensions eventually reach a limiting value. An equation derived from Bazant's size effect law by Fakhimi and Tarokh (2013) and based on the experimental results was used to determine the dimensions of the fracture process zone as a function of specimen size. It was also possible to

predict the size of the fracture process zone in a theoretical infinitely large specimen for which there is no longer any size effect.

It was observed that for the specimen sizes typically used in the laboratory, the size of the fracture process zone that was measured in Charcoal granite specimens undergoing four-point bending was larger than that measured in specimens under three-point bending. However, it is predicted that for larger specimens this difference gets smaller and for a theoretical infinitely large specimen the dimensions of the fracture process zone are very similar for both loading conditions. A possible explanation is that in three-point bending only a small region is exposed to the maximum stress as opposed to four-point bending where a wider section of the specimen experiences the maximum stress. For large enough specimens, the region of the three-point bending tests where the maximum stress is experienced is large enough that the local conditions where the fracture is propagating closely resemble those of four-point bending.

It should be noted that for the DIC method in which it is assumed that it is possible for a traction free crack to propagate before peak load, the length of the process zone is predicted to be larger for specimens under four-point bending when compared to three-point bending even for extremely large specimens. This topic needs further investigation to reduce the controversy on the presence or absence of a traction free crack in the pre peak regime.

In order to better understand how specimen geometry and loading conditions affect the size of the fracture process zone, further research is recommended on this topic. Additional specimen geometries such as semi-circular specimens could be tested under three-point bending conditions to investigate how the change in geometry of the specimen affects the fracture process zone. In addition, validation of the measurements performed in Charcoal granite would be advantageous, this can be done by verifying the results with other detection techniques such as acoustic emission.

REFERENCES

Abé, H., Keer, L. M., Mura, T., 1976. Growth Rate of a Penny-Shaped Crack in Hydraulic Fracturing of Rocks. Journal of Geophysical Research, 81, 6292.

Alam S., Loukili A., Grondin F., Roziere E., 2015. Use of the Digital Image Correlation and Acoustic Emission Technique to Study the Effect of Structural Size on Cracking of Reinforced Concrete. Engineering Fracture Mechanics, 143:17–31

Anderson, E. M., 1972. The Dynamics of Faulting and Dyke Formation with Applications to Britain. Hafner Publishing Co., New York, N.Y., pp. 29-56.

ASTM Standard C1161-13, 2013. Standard test method for flexural strength of advanced ceramics at ambient temperature. ASTM International, West Conshohocken.

Bakku, S. K., Fehler, M., Bakku, M., Fehler, 2014. Monitoring Hydraulic Fracturing Using Distributed Acoustic Sensing in a treatment well. SEG Denver 2014 Annual Meeting.

Barbier, E., 2002. Geothermal Energy Technology and Status: an Overview. Renewable and Sustainable Energy Reviews, 6 (1), 3–65.

Barenblatt G. I., 1959. The Formation of Equilibrium Crack during Brittle Fracture-General Ideas and Hypotheses, Axially Symmetric Cracks. Journal of Applied Mathematics and Mechanics, 23(3):622–36.

Barton, C.C., 1982. Variables in Fracture Energy and Toughness Testing of Rock. The 23rd US symposium on rock mechanics (USRMS). American Rock Mechanics Association.

Bauerle, D., 2000. Laser Processing and Chemistry. Springer, Berlin, 3rd edition.

Bažant, Z. P., 1984. Size Effect in Blunt Fracture: Concrete Rock, Metal. Journal of Engineering Mechanics, 110(4), 518–535.

Bažant, Z.P., Kazemi, M., 1990. Determination of Fracture Energy, Process Zone Length and Brittleness Number from Size Effect, with Application to Rock and Concrete. International Journal of Fracture, 44 (2) 111–131.

Bažant, Z.P., Planas, J. 1998. Fracture and Size Effect in Concrete and other Quasi-Brittle Materials. CRC Press.

Bhandari, A.R., Inoue, J., 2005. Experimental Study of Strain Rates Effects on Strain Localization Characteristics on Soft Rock. Soils and Foundations, 45 No.1: 125 140.

Biolzi, L., Labuz, J.F., Muciaccia, G., 2011. A Problem of Scaling in Fracture of Damaged Rock. International Journal of Rock Mechanics and Mining Sciences, 48 (3), 451–457.

Brooks, Z., Ulm, F.J., Einstein, H., 2012. Role of Microstructure Size in Fracture Process Zone Development of Marble. In: 46th US Rock Mechanics/Geomechanics Symposium. American Rock Mechanics Association.

Brooks, Z., Ulm, F.J., Einstein, H., 2013. Environmental Scanning Electron Microscopy (ESEM) and Nanoindentation Investigation of the Crack Tip Process Zone in Marble. Acta Geotechnica, 8 (3), 223–245.

Bunger, A. P., Gordeliy, E., Detournay, E., 2013. Comparison between Laboratory Experiments and Coupled Simulations of Saucer-Shaped Hydraulic Fractures in Homogeneous Brittle-Elastic Solids. Journal of the Mechanics and Physics of Solids, 61 1636–1654, 2013.

Bunger, A.P., Detournay, E., 2005. Asymptotic Solution for a Penny-Shaped Near-Surface Hydraulic Fracture. Engineering Fracture Mechanics, 72 (16), 2468–24.

Bunger, A.P., Kear, J., Dyskin A.V., Pasternak, E., 2015. Sustained Acoustic Emissions Following Tensile Crack Propagation in Crystalline Rock. International Journal of Fracture, (2015) 193:87–98.

Bunger, A.P., Kear, J., Jeffrey, R., Prioul, R., Chuprakov, D., 2016. Laboratory Investigation of Hydraulic Fracture Growth through Weak Discontinuities with Active Ultrasonic Monitoring. International Society for Rock Mechanics and Rock Engineering, 13th ISRM International Congress of Rock Mechanics.

Chong, K., Li, V.C., Einstein, H., 1989. Size Effects, Process Zone and Tension Softening Behavior in Fracture of Geomaterials. Engineering Fracture Mechanics, 34 (3), 669–678.

Collier, R. J., Doherty, E. T., and Pennington, K. S., 1965. Concrete by Means of Fracture Mechanics and Finite Elements. Applied Physics Letters, 7, 223.

Dawicke D. S., Sutton, M. A., 1994. CTOA and Crack-Tunneling Measurements in Thin Sheet 2024-T3 Aluminum Alloy. Experimental Mechanics, 34(4):357–368.

de Pater, C. J., Groenenboom, J., van Dam, D. B., R. Romijn, R., 2001. Active Seismic Monitoring of Hydraulic Fractures in Laboratory Experiments. International Journal of Rock Mechanics and Mining Sciences, 38 777-785.

Detournay, E., 2004. Propagation Regimes of Fluid-Driven Fractures in Impermeable Rocks. International Journal of Geomechanics, 4 Issue 1.

Detournay, E., 2016. Mechanics of Hydraulic Fractures. Annual Review of Fluid Mechanics, 48, 311–339.

Elices, M., Guinea, G. V., Gómez, J., Planas, J., 2002. The Cohesive Zone Model: Advantages, Limitations and Challenges. Engineering Fracture Mechanics, 69, 137-163.

Fakhimi A., Tarokh A., Labuz J. F., 2017. Cohesionless Crack at Peak Load in a Quasi-Brittle Materials. Engineering Fracture Mechanics, 179:272–7.

Fakhimi A., Wan F., 2016. Discrete Element Modeling of the Process Zone Shape in Mode I Fracture at Peak Load and in Post-Peak Regime. International Journal of Rock Mechanics and Mining Sciences, 85:119–28.

Fialko, Y., 2001. On Origin of Near-Axis Volcanism and Faulting at Fast Spreading Mid-Ocean Ridges. Earth and Planetary Science Letters, 190:31–9.

Galouei M., Fakhimi A., 2015. Size Effect, Material Ductility and Shape of Fracture Process Zone in Quasi-Brittle Materials. Computers and Geotechnics, 65:126–35.

Germanovich, L. N., Lowell, R. P., 1995. The Mechanism of Phreatic Eruptions. Journal of Geophysical Research, 100(B5):8417–34.

Griffith, A. A., 1921. The Phenomena of Rupture and Flow in Solids. Philosophical Transactions of the Royal Society, 221 163–198.

Groenenboom, J., Fokkema, J., 1998. Monitoring the Width of Hydraulic Fractures with Acoustic Waves. Geophysics, 63 NO.1.

Groenenboom, J., van Dam, D. B., 2000. Monitoring Hydraulic Fracture Growth: Laboratory Experiments. Geophysics, 65-2.

Haggerty M., Lin Q., Labuz J.F., 2010. Observing Deformation and Fracture of Rock with Speckle Patterns. Rock Mechanics and Rock Engineering, 43:417–26.

Higgins, D.D. and Bailey, J.E., 1976. Fracture Measurements on Cement Paste. Journal of Materials Science, 11, pp. 1995-2003.

Hillerborg, A., Modeer, M., Petersson, P.E., 1976. Analysis of Crack Formation and Crack Growth in Concrete By Means Of Fracture Mechanics and Finite Elements. Cement and Concrete Research, 6: 773-781.

Horii, H., Nemat-Nasser, S., 1986. Brittle Failure in Compression: Splitting, Faulting and Brittle-Ductile Transition. Philosophical Transactions of the Royal Society, 319 (1549), 337–374.

Inglis, C. E., 1913. Stresses in a Plate Due to the Presence of Cracks and Sharp Corners, Transactions of the Institute of Naval Architects, 55 219–242.

Ingraffea A.R., 1987. Theory of Crack Initiation and Propagation in Rock. In: Atkinson BK, Editor. Fracture Mechanics of Rock. London: Academic Press, p. 71–110.

Irwin G. R., 1957. Analysis of Stresses and Strains Near the End of a Crack Traversing a Plate. Journal of Applied Mechanics, 24. 361-364.

Ishida, T., 2001. Acoustic Emission Monitoring of Hydraulic Fracturing in Laboratory and Field. Construction and Building Materials 283-295.

Ishida, T., Chen Q., Mizuta Y., Roegiers, J.C., 2004. Influence of Fluid Viscosity on the Hydraulic Fracture Mechanism. Transactions of ASME, 126, 190-200.

Ishida, T., Chen, Q., Mizuta, Y., 1997. Effect of Injected Water on Hydraulic Fracturing Deducted from Acoustic Emission Monitoring. Pure Applied Geophysics, 150, 627-646.

Jankowski, L., Stys, D., 1990. Formation of the Fracture Process Zone in Concrete. Engineering Fracture Mechanics, 36 (2), 245–253.

Jeffrey, R. G., Mills, K. W., 2000. Hydraulic Fracturing Applied to Inducing Longwall Coal Mine Goaf Falls. Pacific Rocks, Girard, Lieberman, Breeds & Doe ISB 90 5809 1554.

Jones, J.P., Whittier, J.S., 1967. Waves at a Flexibly Bonded Interface. Journal of Applied Mechanics, 34 (4), 905-909.

Kear, J., White, J., Bunger, A.P., Jeffrey, R., Hessami, A., 2013. Three Dimensional Forms of Closely Spaced Hydraulic Fractures. International Conference for Effective and Sustainable Hydraulic Fracturing (HF 2013).

Kobayashi, R., Matsuki, K. and Otsuka, N., 1986. Size Effect in the Fracture Toughness of Ogino Tuff. International Journal of Rock Mechanics and Mining Sciences and Geomechanics Abstracts, 23-1, pp. 13-18.

Kodaka, T., Higo, Y., Kimoto, S. and Oka, F., 2007. Effects of Sample Shape on the Strain Localization of Water-Saturated Clay. International Journal for Numerical and Analytical Methods in Geomechanics, 31: 483-521.

Kovalyshen, Y., Bunger, A.P., Kear, J., Kasperczyk, D., 2014. Comparison between Ultrasonic and Photometric Methods for Hydraulic Fracture Laboratory Monitoring. International Journal of Rock Mechanics and Mining Science, 70 368-374.

Kuruppu, M., Obara, Y., Ayatollahi, M., Chong, K., Funatsu, T., 2014. ISRM-Suggested Method for Determining the Mode I Static Fracture Toughness Using Semi-Circular Bend Specimen. Rock Mechanics and Rock Engineering, 47 (1), 267–274.

Labuz, J., Biolzi, L., 1998. Characteristic Strength of Quasi-Brittle Materials. International Journal of Solids and Structures, 35 (31-32), 4191–4203.

Labuz, J., Shah, S., Dowding, C., 1985. Experimental Analysis of Crack Propagation in Granite. International Journal of Rock Mechanics and Mining Sciences and Geomechanics Abstracts, 22 (2), 85–98.
Labuz, J. F., Shah, S. P., Dowding, C. H., 1987. The Fracture Process Zone in Granite: Evidence and Effect. International Journal of Rock Mechanics and Mining Sciences and Geomechanics Abstracts, 24. No. 4 pp 235 246.

Lakirouhani, A., Bunger, A., Detournay, E. 2008. Modeling of Hydraulic Fractures from a Wellbore, fifth Asian Rock Mechanics Symposium (ARMS5).

Le, J. L., Bazant, Z. P., 2011. Unified Nano-Mechanics Based Probabilistic Theory of Quasibrittle and Brittle Structures: I. Strength, Static Crack Growth, Lifetime And Scaling. Journal of the Mechanics and Physics of Solids, 59 (7), 1291–1321.

Lecampion, B., Desroches, J., 2015. Simultaneous Initiation and Growth of Multiple Radial Hydraulic Fractures from Horizontal Wellbore. Journal of the Mechanics and Physics of Solids, 82, Pages 235-258.

Lecampion, B., Desroches, J., Jeffrey, R., Bunger, A.P., 2017. Experiments versus Theory for the Initiation and Propagation of Radial Hydraulic Fractures in Low-Permeability Materials. Journal of Geophysical Research: Solid Earth, 122, 1239–1263.

Li X. J., Marasteanu M.O., 2010. The Fracture Process Zone in Asphalt Mixture at Low Temperature. Engineering Fracture Mechanics, 77(7):1175–90.

Li, V. C, 1986. Mechanics of Shear Rupture Applied to Earthquake Zones. Chapter in Rock Fracture Mechanics (Edited eight Atkinson). Academic Press, New York.

Li, B.Q., Einstein, H.H., 2017. Comparison of Visual and Acoustic Emission Observations in a Four Point Bending Experiment on Barre Granite. Rock Mechanics and Rock Engineering, 50, 2277–2296.

Lin, Q., & Labuz, J. F., 2011. Identifying Quasi-Brittle Fracture By AE and Digital Imaging. Journal of Acoustic Emission, 29, 68-77.

Lin Q., Labuz J. F., 2013. Fracture of Sandstone Characterized By Digital Image Correlation. International Journal of Rock Mechanics and Mining Science, 60, 235–245.

Liu, J. and Iskander, M., 2004. Adaptive Cross Correlation for Imaging Displacements in Soils. Journal of Computing in Civil Engineering, 18: 46-57.

Lockner, D., Byerlee, J., Kuksenko, V., Ponomarev, A., Sidorin, A., 1991. Quasi-Static Fault Growth and Shear Fracture Energy in Granite. Nature, 350 (6313), 39–42.

Lockner, D., Byerlee, J.D. 1977. Hydrofracture in Weber Sandstone at High Confining Pressure and Differential Stress. Journal of Geophysical Research, 82 (14), 2018–2026.

Makhnenko, R., Bunger, A., Detournay, E., 2010. Deviation from Linear Elastic Fracture in Near Surface Hydraulic Fracturing Experiments with Rock. 44th US Rock Mechanics Symposium and 5th US-Canada Rock Mechanics Symposium. American Rock Mechanics Association

Matsuki, K., Hasibuan, S., Takahashi, H., 1991. Specimen Size Requirements for Determining the Inherent Fracture Toughness of Rocks According to the ISRM Suggested Methods. International Journal of Rock Mechanics and Mining Sciences and Geomechanics Abstracts, 28 (5), 365–374.

Meng, C., de Pater, C.J., 2010. Acoustic Imaging of Hydraulic Fracture Evolution. SEG Denver 2010 Annual Meeting.

Mihashi, H., Nomura, N. and Niiseki, S., 1991. Influence of Aggregate Size on Fracture Process Zone of Concrete Detected with Three Dimensional Acoustic Emission Technique. Cement and Concrete Research, 21, pp. 737-744.

Murdoch, L.C., 2002. Mechanical Analysis of Idealized Shallow Hydraulic Fracture. Journal of Geotechnical and Geoenvironmental Engineering, 128,488–495.

Nabipour, A. 2013. Experimental and Numerical Study of Ultrasonic Monitoring of Hydraulic. Thesis, Curtin University.

Nakayama, T., Tanaka, M., Nishimura, H., Ueda, M., Ishida, T., Mizuta, Y., 2000. Borehole AE Monitoring During in-Situ Hydraulic Fracturing Stress Measurements Pacific Rocks, Girard, Liebman, Breeds 6; Doe (eds) O 2000 Balkema, Rotterdam, ISBN 90 5809 155 4.

Otsuka, K. and Date, H., 2000. Fracture Process Zone in Concrete Tension Specimens. Engineering Fracture Mechanics, 65, 111-131.

Ouchterlony, F., 1990. Fracture Toughness Testing of Rock with Core Based Specimens. Engineering Fracture Mechanics, 35 (1), 351–366.

Parisio, F., Tarokh, A., Makhnenko, R., Naumov, D., Miao, X.Y., Kolditz, O., Nagel, T., 2019. Experimental Characterization and Numerical Modelling Of Fracture Processes in Granite. International Journal of Solids and Structures.

Peng, S. and Johnson, A.M., 1972. Crack Growth and Faulting in Cylindrical Specimens of Chelmsford Granite. International Journal of Rock Mechanics and Mining Science. 9, pp. 37-86.

Peters, W. H., Ranson, W. F., Sutton, M. A., Chu, T. C., 1983. J. Application of Digital Correlation Methods to Rigid Body Mechanics. Optical Engineering, 22 No.6: 738-742.

Pollard, D.D., Holzhausen, G., 1979. On the Mechanical Interaction Between a Fluid-Filled Fracture and the Earth's Surface. Tectonophysics, 53:27–57.

Rokhlin, S.I., Wang, Y. J., 1991. Analysis of Boundary Conditions for Elastic Wave Interaction with an Interface between Two Solids. The Journal of Acoustical Society of America, 89, 503.

Savic, M., 1995. Ultrasonic Scattering from a Hydraulic Fracture: Theory, Computation and Experiment. Ph.D. Thesis, Delft University of Technology.

Savitski A., Detournay, E., 2002. Propagation of a Penny-Shaped Fluid-Driven Fracture in an Impermeable Rock: Asymptotic Solutions. International Journal of Solids and Structures, 39:6311-6337.

Schmidt, R. A., Lutz, T., 1979. KIc and JIc of Westerly Granite–Effects of Thickness and In-plane Dimensions. In: Fracture Mechanics Applied to Brittle Materials, ASTM International.

Schmidt, R.A., 1976. Fracture-Toughness Testing Of Limestone. Experimental Mechanics, 16 (5), 161–16.

Stanier S., Blaber J., Take W., White D., 2016. Improved Image-Based Deformation Measurement for Geotechnical Applications. Canadian Geotechnical Journal, 53:727–739

Sutton, M.A., Orteu, J. J., Schreier, H., 2009. Image Correlation for Shape, Motion and Deformation Measurements: Basic Concepts, Theory and Applications, Springer, US, Rigden, J. D., Gordon, E. I., Proc. I.R.E., 50, 2367.

Shah, S.P., 1990. Experimental Methods for Determining Fracture Process Zone and Fracture Parameters. Engineering Fracture Mechanics, 35: 3-14.

Shlyapobersky, J., 1985. Energy Analysis of Hydraulic Fracturing. 26th U.S. Symposium on Rock Mechanics, Rapid City, South Dakota, USA539–546.

Skarzynski, L, Tejchman, J., 2016. Experimental Investigations of Fracture Process in Concrete by Means Of X-Ray Micro-Computed Tomography. Strain, 52 (1), 26–45.

Stanchits, S., Surdi, A., Edelman E., Suarez-Rivera R., 2012. Acoustic Emission and Ultrasonic Transmission Monitoring of Hydraulic Fracture Propagation in Heterogeneous Rock Samples. 46th Rock Mechanics/Geomechanics Symposium, American Rock Mechanics Association. 12-527.

Stewart, L., Cassell, B.R., Boll, G.M., 1992. Acoustic-Emission Monitoring During Hydraulic Fracturing. SPE Formation Evaluation.

Tarokh A., Fakhimi A., Labuz J. F., 2012. Size of Process Zone in Fracture Testing of Rock. 46th Rock Mechanics/Geomechanics Symposium, American Rock Mechanics Association, 12-527.

Tarokh A., Makhnenko R. Y., Fakhimi A., Labuz J. F., 2017. Scaling of the Fracture Process Zone in Rock. International Journal of Fracture, 204(2):191.

Tarokh, A., Blanksma D.J., Fakhimi, A., Labuz, J., 2016. Fracture Initiation in Cavity Expansion of Rock. International Journal of Rock Mechanics and Mining Sciences. 85(2016)84–91.

Tarokh, A., Fakhimi, A., 2013. Relationship between Grain Size and Fracture Properties of Rock. 47th US Rock Mechanics/Geomechanics Symposium, American Rock Mechanics Association.

Tarokh, A., Fakhimi, A., 2014. Discrete Element Simulation of the Effect of Particle Size on the Size of Fracture Process Zone in Quasi-Brittle Materials. Computers and Geotechnics, 62, 51–60.

Tehrani F.S., Arshad MI, Prezzi M., Salgado R., 2017. Physical Modeling of Cone Penetration in Layered Sand. Journal of Geotechnical and Geoenvironmental Engineering, 144(1): p04017101.

Topic J., Bartos J., Kopecky L., Seps K., Pros Z., Trejbal J., 2016. Cement Composite Reinforced With Synthetic Fibers: Comparison of Three-Point And Four-Point Bending Test Results. Applied Mechanics and Materials, 827:332–335

Vavro, L., Soucek, K., Kytýr, D., Fíla, T., Keršner, Z., Vavro, M., 2017. Visualization of the Evolution of the Fracture Process Zone in Sandstone by Transmission Computed Radiography. Procedia Engineering, 191, 689–696.

Vilarrasa, V., Carrera, J., 2015. Geologic Carbon Storage Is Unlikely To Trigger Large Earthquakes And Reactivate Faults Through Which CO2 Could Leak. Proceedings of the National Academy of Sciences of the United States of America, 112 (9), 5938–5943.

Wang, C., Peide, L., Rongsheng, H., Xiutang, S., 1990. Study of the Fracture Process Zone in Rock by Laser Speckle Interferometry. International Journal of Rock Mechanics and Mining Sciences and Geomechanics Abstracts, 27 (1), 65–69.

Watanabe, N., Egawa, M., Sakaguchi, K., Ishibashi, T., Tsuchiya, N., 2017. Hydraulic Fracturing and Permeability Enhancement in Granite from Subcritical/Brittle to Supercritical/Ductile Conditions. Geophysical Research Letters.

Watanabe, N., Numakura, T., Sakaguchi, K., Saishu, H., Okamoto, A., Ingebritsen, S.E., Tsuchiya, N., 2017. Potentially Exploitable Supercritical Geothermal Resources in the Ductile Crust. Nature Geoscience, 10 (2), 140–144.

Wegst, U. G., Bai, H., Saiz, E., Tomsia, A. P., Ritchie, R.O., 2015. Bioinspired Structural Materials. Natuer Materials, 14 (1), 23–36.
Wu, Z., Rong, H., Zheng, J., Xu, F., Dong, W., 2011. An Experimental Investigation on the FPZ Properties in Concrete Using Digital Image Correlation Technique. Engineering Fracture Mechanics, 78 (17), 2978–2990.

Yamaguchi, I., 1981. Speckle Displacement and Decorrelation in the Diffraction and Image Fields for Small Object Deformation. Optica Acta: International Journal of Optics, 28 pp. 1359-1376.

Young, C., 1999. Controlled-Foam Injection for Hard Rock Excavation. Rock Mechanics for Industry, Proceedings of 37th US Rock Mechanics Symposium, Vail, Colorado, 1,115–122.

Zang, A., Wagner, F.C., Stanchits, S., Janssen, C., Dresen, G., 2000. Fracture Process Zone in Granite. Journal of Geophysical Research: Solid Earth, 105 (B10), 23651–2366.

Zhang, D. and Wu, K., 1999. Fracture Process Zone of Notched Three-Point Bending Concrete Beams. Cement and Concrete Research, 29, pp. 1877-1892.

Zhang, X., Detournay, E., Jeffrey, R., 2002. Propagation of a Penny-Shaped Hydraulic Fracture Parallel to the Free Surface of an Elastic Half-Space. International Journal of Fracture, 115, 125–158.

Zhu, G., Gu, L., Su, J., Dai, J., Ding, W., Zhang, J. and Song, L., 2012. Sedimentary Association of Alternated Mudstones and Tight Sandstones in China's Oil and Gas Bearing Basins and its Natural Gas Accumulation. Journal of Asian Earth Science, 50, 88–104.

Zietlow, W.K. and Labuz, J.F., 1998. Measurement of the Intrinsic Process Zone in Rock Using Acoustic Emission. International Journal of Rock Mechanics and Mining Sciences, 35, No.3, pp. 291-299.

APPENDIX A: ULTRASONIC MONITORING OF NEAR SURFACE HYDRAULIC FRACTURES IN CRYSTALLINE ROCK

Ultrasonic measurements are a powerful tool in monitoring and understanding the physics of hydraulic fractures and they can be used at both laboratory and field scales. In order to better understand hydraulic fracture propagation and any effects the specimen geometry may have on it, hydraulic fracturing experiments are carried out in granite blocks of different sizes that are loaded equally in two directions with no load applied along the third direction. An injection fluid consisting of a glycerin-water mixture is injected at one third of the specimen depth. The geometrical asymmetry of the problem causes the hydraulic fractures to propagate in a curving manner towards the free surface of the block that is characteristic of near surface hydraulic fractures. Throughout the experiments, the fracture is monitored with time lapsed ultrasonic measurements with active sources from both compressional (P-wave) and shear wave (S-wave) transducers. As the hydraulic fracture propagates, it interacts with the ultrasonic waves, and by studying these interactions it is possible to detect and characterize the geometry of the fracture. When the fracture crosses the line of sight of two compressional wave transducers, the P-waves are dispersed and attenuated and the fracture width can be calculated by studying the effect this has on the signals, diffractions caused by the fracture tip can be used to located the fracture tip and calculate its radius and S-waves reflected by the fracture can be used to calculate the fracture depth. The results are compared to measurements of the surface displacement of the blocks and to the analytical solution from a model that describes the geometry of penny-shaped hydraulic fractures and are shown to be in general agreement.

Introduction

Hydraulic fractures are tensile cracks that result from high pressure injection of a viscous fluid into a solid medium. Common applications of hydraulic fracturing include the stimulation of low-permeable or unconventional reservoirs for oil extraction and in enhanced geothermal systems. The presence of an asymmetric stress field near the fracture tip can cause the fracture to curve (Murdoch 2002; Bunger et al. 2005; Bunger et al. 2013), this condition is most commonly observed when the hydraulic fracture propagates in the vicinity of a free surface and can also happen as a result of a propagating fracture interacting with another preexisting fracture (Kear et al. 2013). Field applications for so-called near surface hydraulic fractures include petroleum exploration (Lecampion and Desroches 2015), hard rock excavation (Young 1999), quarrying (Pollard and Holzhazhuaen 1979), controlled generation of goafing events in mines (Jeffrey and Mills 2000), and environmental remediation (Murdoch 2002). In addition, some geological processes involve near surface hydraulic fracturing, such as the intrusion of dikes and sills which propagate with a small depth relative to their length (Anderson 1972; Fialko 2001) and phreatic eruptions (Germanovich and Lowell 1995). The design of hydraulic fracture systems in the field depends on assumptions on their behavior and geometry. The propagation of hydraulic fractures is a complicated process and often times there is insufficient data to properly characterize them, which may lead to undesirable results. The study and monitoring of near surface hydraulic factures is an important step towards more accurate models to describe them, which in turn will be beneficial to better understanding and predicting these processes.

Non-destructive geophysical methods have been successfully utilized to detect and monitor hydraulic fractures and characterize their properties. Acoustic emission (AE) has been effectively used to monitor the initiation, propagation, and reopening of hydraulic fractures in the laboratory

(Lockner and Byerlee 1977; Stewart 1992; Ishida 2001) and for measurements for the in-situ stress field (Nakayama et al. 2000, Ishida, 2001). AE is used to study the effect of injection rates and of the viscosity of the injection fluid on hydraulic fracturing in granite (Ishida et al. 1997, 2004) and to investigate the effect that discontinuities in the rock have on propagating hydraulic fractures in shale and sandstone (Stanchits et al. 2012). AE successfully was used to locate events caused by and hydraulic fracture propagating in locks of Adelaide Black Granite with no external loading (Bunger et al. 2015). Bunger (2005) presented a photometric approach for monitoring and measuring the width of fluid driven fractures in transparent materials where the crack front can be observed directly and the crack width can be calculated based on the diminishing intensity of the light passing through the fluid filled crack compared to light passing only through the transparent specimen.

In this paper, the use of ultrasonic measurements to monitor and characterize near surface hydraulic fractures is discussed. By studying the behavior of the ultrasonic wave signals and their interaction with propagating hydraulic fractures, rock and fracture parameters can be extracted. In addition, ultrasonic measurements allow for the repeatability of measurement, whereas the lack of data redundancy is one of the major limitations of passive methods such as AE. Groenenboom and Fokkema (1998), de Pater et al. (2001) and Groenenboom and van Dam (2001) present the use of ultrasonic measurements to monitor hydraulic fractures and characterize their geometry. Ultrasonic monitoring has been used to measure the width and radius of propagating planar hydraulic fractures in artificial rock and cement.

Ultrasonic monitoring allows for attaining of additional information such as the fracture growth rate, the change of fracture width over time, and the change in behavior of the fracture after the pump is shut (Savic, 1995). Meng (2010) and Bunger et al. (2015) used ultrasonic

measurements to track the moving crack front and its interactions with pre-existing fractures in rock specimens. Nabipour (2013) used ultrasonic measurements to monitor hydraulic fractures in specimens at different states of stress. Additionally, ultrasonic methods have been used in conjunctions with other methods in order to validate the results. Stanchits (2012) used AE to detect fracture initiation and propagation while ultrasonic measurements are adopted to determine the fracturing stages (initiation, interaction with an artificial discontinuity, and propagation away from the interface). Kovalyshen (2014) compared the results of photometric measurements to ultrasonic measurements performed on the same specimen and found consistency between the two methods. Ultrasonic measurements were used in Adelaide Black granite to study the interaction of a propagating hydraulic fracture and weak discontinuities and by determining if the hydraulic fracture crossed the discontinuity (Bunger et al. 2016). Ultrasonic measurements also show potential for development towards future use in field applications (de Pater et. al. 2001). Sudish et al. (2014) discusses active source seismic experiment in a treatment well and analyzes time-lapse changes resulting from the hydraulic fractures. The experiment takes place in a gas-field where seismic data is recorded in Distributed Acoustic Sensing, the time-lapse changes resulting from stimulation are discussed and potential is shown for the use of this method in the field.

Previous studies deal with planar or penny shaped fractures. In this study, ultrasonic measurements are used to monitor near surface or saucer pan shaped hydraulic fractures. In the laboratory experiments presented, the granite blocks with low permeability are subjected to an asymmetric stress field. This condition causes the fracture to curve towards the free surface forming a saucer-pan shape (Murdoch, 2002; Bunger et al. 2005). The curvature of the hydraulic fracture poses additional challenges in characterizing the geometry of the fracture. LVDTs were installed on the free surface in order to independently measure the fracture aperture and compare

with the results obtained from ultrasonic measurements. The use of ultrasonic monitoring in crystalline rock with low permeability is important because these characteristics better represent the rock formations that are relevant for common applications of hydraulic fracturing processes.

Background

A near surface hydraulic fracture is a fluid driven fracture caused by the injection of a viscous fluid that propagates at depth from a free surface that is comparable to its length. During the initiation of the fracture, while its radius is smaller than the depth, the fracture will propagate in a planar manner in a direction parallel to the free surface. As the fracture radius becomes comparable to the depth, the fracture will begin to curve towards the free surface until it will eventually daylight. The curving of the fracture is a result of the asymmetry of the stress field and the geometry of the problem (Murdoch, 2002; Bunger et al. 2005; Bunger et al. 2013).

Scaled laboratory experiments are set up in blocks of crystalline rock and a near surface hydraulic fracture is induced while the specimen is loaded in two directions with no load in the third. Throughout the experiment, as the hydraulic fracture propagates, ultrasonic transducers scan the rock sample repeatedly. Waves are sensitive to the properties of the medium in which they propagate and are known to be affected by the presence of fractures in rock, as well as the fluid that fills the fracture (Groenenboom and Fokkema 1998). The interactions of the ultrasonic waves with the hydraulic fracture are analyzed in order to monitor and characterize the fracture properties.

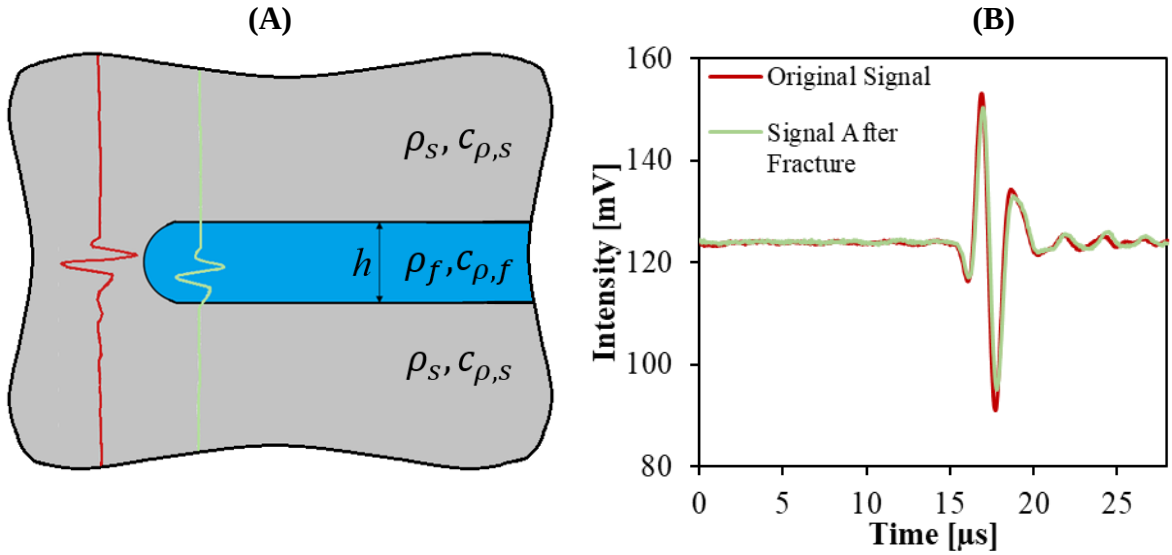

Figure A.1: **(A)** Schematic diagram of an hydraulic fracture modeled as a thin fluid filled layer and its effect on ultrasonic signals. **(B)** Compressional wave signal affected by the presence of a fracture.

It has been observed that when the fracture tip is sufficiently far away, shear waves are completely shadowed in the presence of a fracture, indicating that there are no frictional contacts between the sides of the fracture (the fracture is acoustically open). These observations have led to the conclusion that it is appropriate to model the fracture as a thin homogeneous layer that is filled with a fluid (Groenenboom and Fokkema 1998) as opposed to a linear slip model that was traditionally used (Jones and Whittier 1967).

In this paper, three different types of interactions between the waves and the hydraulic fracture are discussed and used to calculate different parameters; these interactions are summarized in the Figure A.2 The tip of the hydraulic fracture is known to act as a strong diffractor of acoustic waves (Groenenboom and van Dam, 2001). Through an analysis of wave diffractions caused by the fracture tip, it is possible to pinpoint the location of the fracture tip in time and monitor the growth and radius of the fracture. The fracture also causes dispersion and attenuation of compressional waves as they cross the fracture interface and the fracture aperture can be detected and its width

measured by analyzing the attenuated and dispersed signals. Additionally, S-waves are partially reflected by the fracture and it is possible to measure the depth of the fracture by analyzing the reflection of S-waves.

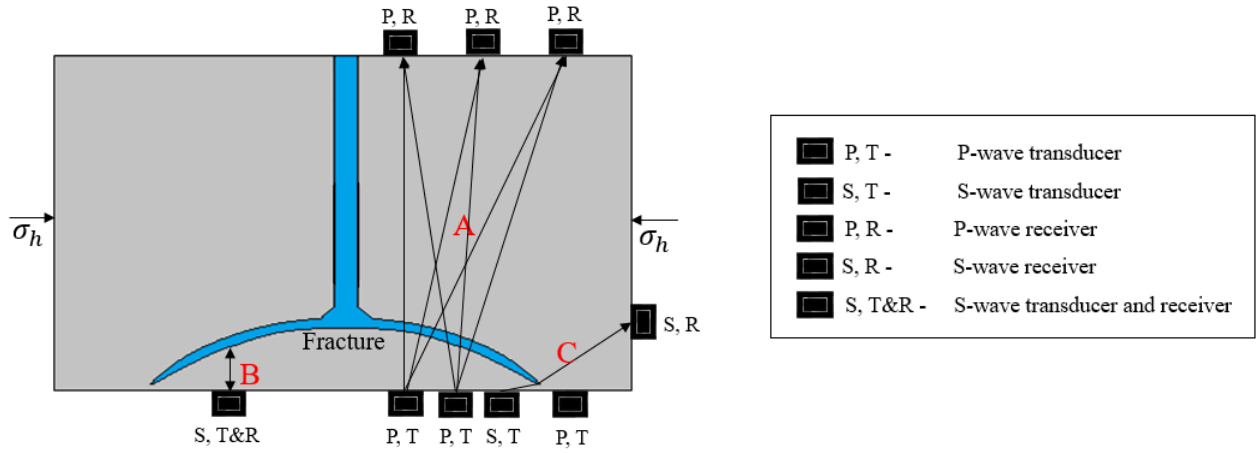

Figure A.2: Experimental set up of the rock block and the ultrasonic transducers/receivers to monitor a near surface hydraulic fracture. Three types of measurement configurations for the transducers/receivers are shown: (A) dispersions and attenuation of P-waves (B) reflection of S-waves (C) diffraction of S-waves.

Determination of fracture width

The effect that the fracture has on compressional waves after it has crossed the line of sight of a transducer pair is further analyzed to obtain the fracture aperture and calculate its width. Originally wave signals are in the time domain, and in order to study the wave signals in the frequency domain, a Fourier transformation is performed. From the theory of wave propagation in layered media (Groenenboom and Fokkema 1998, Rokhlin and Wang 1991), the following parameters are defined: ρ_f is the density of the fluid in the fracture, ρ_s is the density of the solid rock, $c_{p,f}$ is the P-wave velocity in the fluid, $c_{p,s}$ is the P-wave velocity in the solid, h is the fracture width, and ω is the frequency of the signal.

The impedance ratio between the solid and the fluid phase, which is a function of the properties of the solid and the fluid is introduced as:

$$z_r = \frac{\rho_f c_{\rho,f}}{\rho_s c_{\rho,s}} \tag{A.1}$$

Using the impedance ratio the reflection coefficient can be defined as:

$$r_{ff} = -\frac{1-z_r}{1+z_r} \tag{A.2}$$

For a layer of width *h*, the one-way phase delay related to the propagation of a wave in the thin fluid layer is given by:

$$\alpha = \frac{\omega h}{c_{\rho,f}} \tag{A.3}$$

With these quantities, the global transmission coefficient in Fourier domain can be defined as:

$$\hat{T}(\omega,h) = \frac{(1-r_{ff}{}^2)\exp(-i\alpha)}{1-r_{ff}{}^2\exp(-i\alpha)} \tag{A.4}$$

The reference signal (from pristine rock), S_0, is transformed to the Fourier domain, $\hat{S}_0$, and it can be used to find the predicted signal frequency $\hat{S}^T$ for a fracture of width *h*:

$$\hat{S}^T(\omega,h) = \hat{T}(\omega,h)S_0 \tag{A.5}$$

The width of the fracture at each scan can be estimated by minimizing the misfit for a range of fractures width between the measured signal $S^D(t)$ and the predicted signal $S^T(t)$ in the time domain.

$$E(h) = \sum \omega(t_i) = \left| S^T(t_i,h) - S^D(t_i) \right|^2 = \min \tag{A.6}$$

As it can be observed, the theoretical signal for a fracture of width *h* is a function of the densities and P-wave velocities of the fluid and the solid and the width of the fracture. The only

unknown in equation 5 is the width of the fracture. Therefore, *h* can be found by finding the fracture width that minimizes the misfit between the theoretical and the measured signals. Figure A.3 shows the misfit over a range of fracture widths between the theoretical and measured signals for a certain moment of time. The width of the fracture corresponding to the minimum error is taken as the calculated width of the fracture at that moment of time.

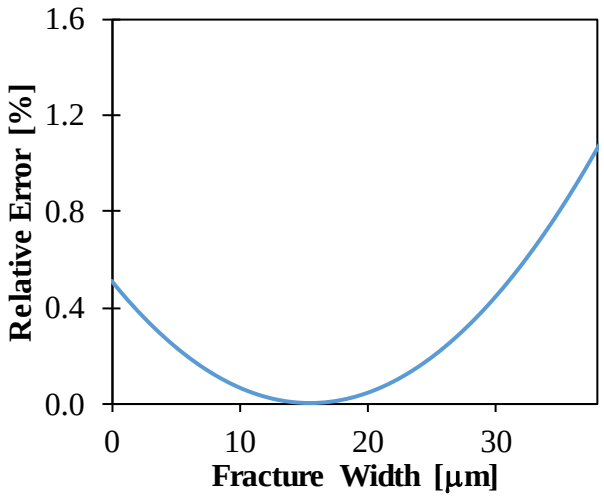

Figure A.3: Fracture width vs relative error of the misfit between the theoretical and measured signal at a given moment of time. The calculated fracture width is reported as one where relative error is minimized.

Determination of fracture geometry using a 2D transducer set

In an experimental setup where side transducers are not available, other techniques can be utilized to characterize fracture geometry as a function of time. This is done by analyzing the way the fracture affects different types of signals. The change in the signal caused by the fracture propagation can be presented using difference domain plots and the different types of interactions between the fracture and the ultrasonic waves cab ne used to calculate different fracture parameters.

Difference domain plots provide information on the change in the signals related only to the propagation of the fracture (Savic 1995). The signal begins to be monitored before the fracture

starts to propagate such that the initial scans can be used as a reference. When the fracture begins propagating, the signal continues to be recorded at each scan. By comparing each scan to the reference scan, it is possible to determine the changes in the signal are related to the fracture itself. Difference domain plotting consists of presenting the difference each signal and the reference signal.

Figures A.4 (A) and (B) show two different types of difference domain plots. It can be observed that initially the signal does not change, meaning that the signal is equal to the reference signal, or that there is not any observed effect because the fracture has not yet propagated. As the fracture propagates and approaches the transducers (where the signal is measured), it is possible to observe a change in the signals.

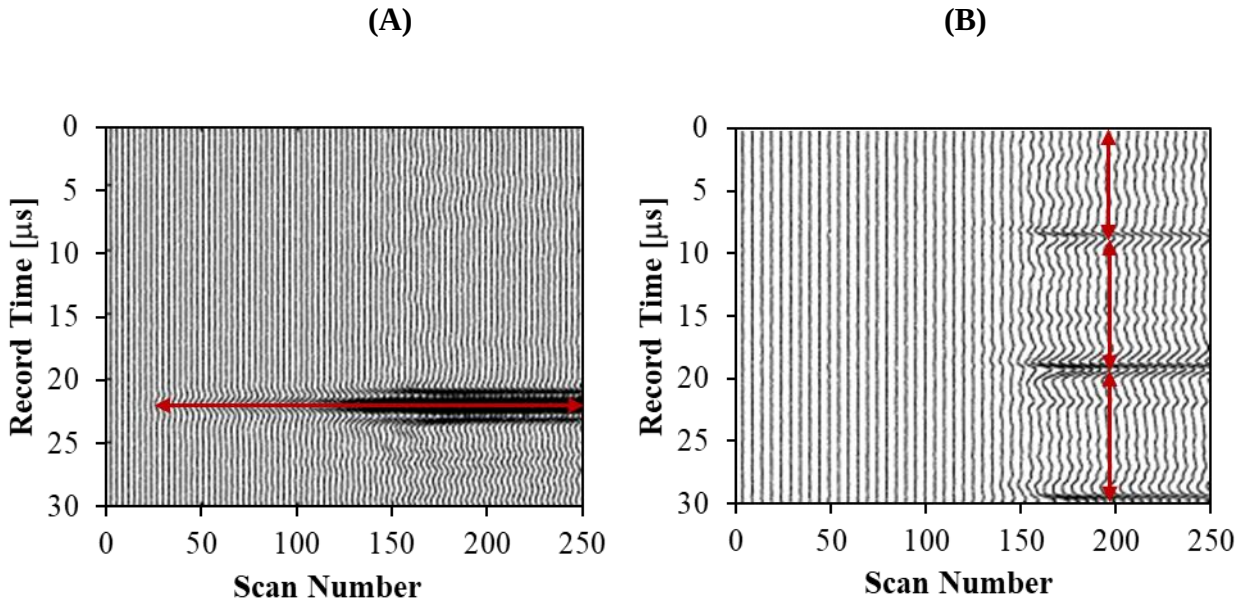

Figure A.4: Difference Domain plot for (A) dispersion and attenuation of P-waves resulting from a fracture in the line of sight of a transducer pair (B) S-waves reflected by the fracture.

In Figure A.4 (A), before scan number 25 the signal is equal to the reference signal, from scan number 30 it begins to be altered, and the change in the signal is interpreted as the dispersion and attenuation of P-waves caused by the hydraulic fracture. This is a result of the fracture approaching the line of site of the transducers and interacting with the signal. It can be observed that the alteration in the signal becomes more severe as time goes on, which is interpreted as an increase in fracture width. In Figure A.4 (B), the scans are different from the reference scan starting from scan number 150 and onwards. It can be seen that the signal is disturbed periodically on the record time of the scan. This is a result of S-waves being reflected from the hydraulic fracture and being detected, the waves are reflected a total of three times during the recorded time frame.

The fracture radius as a function of time can be calculated by analyzing the dispersion of compressional waves caused by the fracture. When P-wave transducers are placed on opposite sides of the specimen at different lengths from the borehole, the signal is affected as the fracture

nears the line of sight of the transducers. By comparing the undisturbed signal with the signal at each time step after fracture propagation has started using difference domain plots it is possible to observe the moment when the fracture first reaches the line of sight of each transducer pair and locate the fracture tip. The depth of the fracture can be calculated by analyzing the reflection of the shear waves from the fracture surface. Since the fracture is a fluid filled layer and are the S-wave velocity in the fluid is zero, the shear waves do not cross the fracture are instead partially reflected by the fracture (Groenenboom and van Dam, 2000). It is possible to place shear wave transducers along the free surface of the specimen, and since the S-wave velocity in the material is known, by measuring the arrival time of the reflected signals it is possible to calculate the depth of the fracture at the location of the transducer.

Using 3D set of transducers to determine fracture geometry

The fracture radius and depth can also by monitored by analyzing the wave diffractions caused by the fracture tip, these events are visible when the transducers and receivers face the fracture at an angle of 90 ° as shown in Figure 5. The change in location of the fracture tip causes a change in the arrival time of the diffracted events. By analyzing the change in arrival time of diffracted events, it is possible to reconstruct the fracture radius and depth. It was observed in Groenenboom and van Dam (2000) and de Pater et al. (2001) that shear waves are appreciably more sensitive to the tip, and that diffractions of compressional waves could not be detected in a meaningful way beyond background noise levels. Therefore, the configuration shown in Figure 5 utilizes shear wave transducers to detect wave diffractions caused by the fracture tip. It is important

to note that the S-wave receiver on the side of the block was placed below the initial fracture surface to get signals reflected from the tip and not the surface.

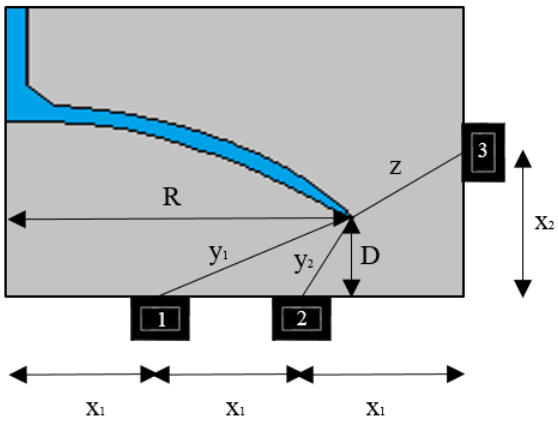

Figure A.5: Shear wave transducer configuration used to monitor the fracture radius and depth in small size blocks.

The arrival times t_1 and t_2 for the reflected signals of transducers 1-3 and 2-3 respectively were measured and the following system equations (7) was solved, were $c_{s,s}$ is the shear wave velocity in the solid and δ is either the positive half length of the transducer's active element, the negative half length of the transducer's active element or zero depending on where the fracture tip is located. It was noticed that the signals are transmitted and received from the whole surface of the transducers, so the shortest travel time for the signals had to be taken into account.

$$\begin{cases} y_1^2 - D^2 - (R - (x_1 + \delta))^2 = 0 \\ y_2^2 - D^2 - (R - (2x_1 + \delta))^2 = 0 \\ z^2 - (3x_1 - R)^2 - (x_2 - D)^2 = 0 \\ y_1 + z - c_{s,s} t_1 = 0 \\ y_2 + z - c_{s,s} t_2 = 0 \end{cases} \tag{A.7}$$

The system of equations is solved three times, one time for each of the possible values of δ ; as a result, t_1, t_2, the radius and depth of the fracture are calculated in each time step. After the

experiment is concluded, the solutions for the system of equations are compared with the direct measurements in order to decide which estimate for δ is in fact accurate.

Experiments with the transducer/receiver configuration described in Figure 4 were performed in two different small blocks. Figure 6 shows difference domain graphs for diffractions from the wave tip detected by transducer/receiver pair 1 and 2 for one of these experiments. Figure A.6 (A) shows the diffractions detected by the transducer 1 / receiver pair. While initially the signal is not altered, as the signal becomes affected by the fracture changes in the signal occur At first the signals are the equal to the reference signal, but once the fracture is detected the interactions are detected at an earlier record time as the scan number increases, this is a result of the fracture tip moving and changing the travel path of the diffracted waves. It can be observed that the signal is altered at an earlier record time as the experimental time increases, this is a result of the change in the travel path of the diffracted waves caused by the change in position of the fracture tip. Figure A.6 (B) shows the diffractions detected by the transducer 2/ receiver pair. The experiment ended a few moments after the fracture was initially detected by this receiver/transducer pair, as a result a change in arrival time was not detected. The radius and depth for the fracture where calculated for the moment the fracture was detected by the transducer 2/receiver pair for the arrival time measured at this moment. This was the case for the two experiments where the 3D transducer geometry was available.

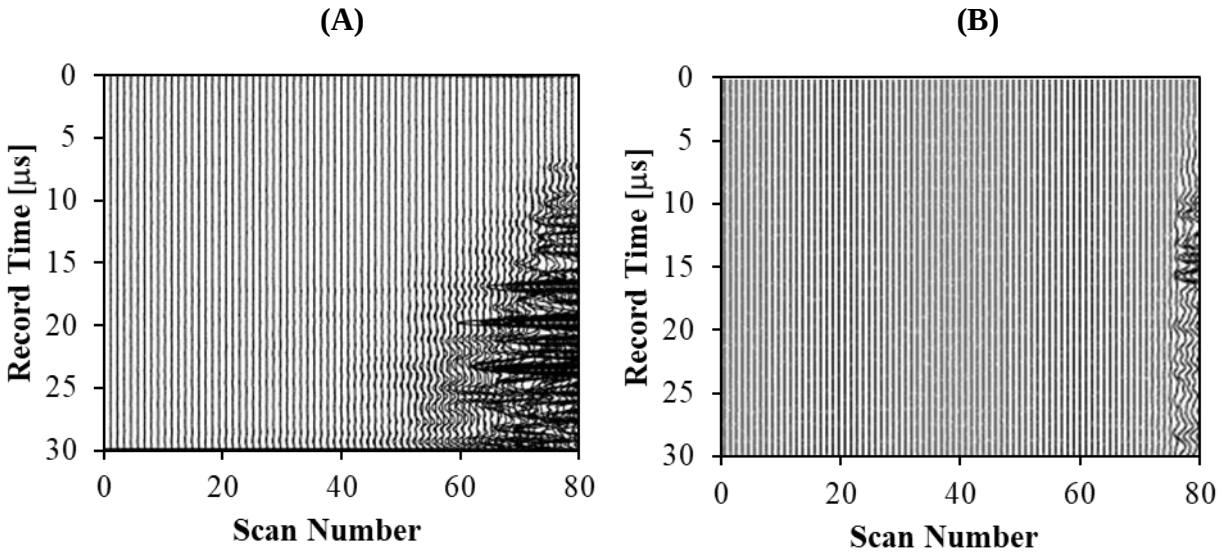

Figure A.6: Difference Domain plot for the effect of the diffractions caused by the fracture tip. (A) Diffractions detected by the transducer 1 / receiver pair ,the solid line shows how the diffractions arrive at an earlier time for later scans (B) Diffractions detected by the transducer 2 / receiver pair, the experiment ended shortly after the fracture was first detected by this transducer/receiver pair.

Experimental Methods

The hydraulic fracturing experiments were carried out using blocks of Adelaide Black Granite (ABG) from Australia. ABG is a crystalline gabbro with an average grain size of 2 mm and density ρ = 2870 kg/m^3.The rock has no weak planes and it has an extremely low permeability (~ 10^{-20} m^2) making the leak-off of fluid from the hydraulic fractures into the rock negligible during the experimental times (few hours). The ultrasonic velocities are measured on the blocks of rock and ($c_{p,s}$ [km/s]; $c_{s,s}$ [km/s]) pairs in three different directions are (6.30; 3.83), (6.31; 3.77), and (6.16; 3.66), indicating slight (2-4%) anisotropy. The calculated values of dynamic Young's modulus and Poisson's ratio (E [GPa]; ν) ratio are (102 GPa; 0.21), (100 GPa; 0.22), and (94 GPa; 0.23). These values correlate well (within 7%) with the same parameters measured in static uniaxial

compression tests performed on cylindrical specimens (30 mm in diameter and 60 mm tall) cored in the same directions: (110 GPa; 0.21), (105 GPa; 0.30), and (91 GPa; 0.21). Close correlation between the elastic properties obtained from ultrasonic (dynamic) and static (strain rate ~ 10^{-6}/s) measurements is attributed to low crack density in the rock.

The ultrasonic monitoring of hydraulic fracturing experiments was carried on several blocks and two different specimen sizes were used: small size blocks with dimensions of 200×200×120 mm and large size blocks with dimensions of 400×400×235 mm. A vertical borehole was drilled in the middle of the blocks to simulate a well, with the dimensions of 8.2 mm in diameter and 96-98 mm depth for the small size blocks and 18.3 mm in diameter and 187-190 mm depth for the large size blocks. Similarly to Bunger (2005), a 0.5-2 mm circumferential notch was carved at the bottom of the boreholes to act as a stress concentrator and therefore the point of fracture initiation. A metal tube was inserted and glued in the boreholes and connected to a pump from which the fluid was injected into the blocks at constant injection rate throughout fracture initiation and propagation.

The injection fluid consisted of a mixture of water, red food dye, and glycerin. The red food dye was added to better observe the fractures in the post-mortem analysis of the rock blocks. The glycerin with the viscosity of 1.4 Pa·s was added to increase the duration of the experiment. The dynamic viscosity of the injection fluid is dependent on temperature and is expressed using the following equation:

$$\mu = 294.4 \cdot T^{-1.996} \tag{A.8}$$

where μ [Pa·s] is the dynamic viscosity and T [ºC] is the temperature. The constants were determined using a Canon-Feske capillary viscometer in a variable temperature water bath. In

order to ensure that the hydraulic fractures occur in the so-called toughness dominated regime (Savitski and Detournay 2002, Detournay 2004), where the primary mechanism of energy dissipation is the fracturing of the rock as opposed to viscous flow effects, the duration of the experiment has to exceed a characteristic time defined by:

$$t_{mk} = 0.0145 \cdot \left(\frac{\mu^5 Q^3 E'^{13}}{K_{IC}^{18}} \right)^{0.5} \tag{A.9}$$

where Q is the injection rate, $E' = E/(1 - \nu^2)$, and K_{IC} is the fracture toughness. K_{IC} was measured in semicircular beam tests performed on specimens with diameters 30 – 90 mm. K_{IC} was found to be in the range of 1.27-2.98 MPa·m$^{0.5}$ (Parisio et al. 2019) showing size dependence captured by Bazant's size effect law (Bazant and Planas 1997). The injection rates used in the experiments were in the range of 0.79-3.0 mm^3/sec, the characteristic time was found to be less than 0.05 seconds for all the experiments. As a result, it can be stated that the experiments were conducted in a toughness-dominated regime.

The specimens were loaded inside the polyaxial reaction frame equally in two lateral directions using water filled flat-jacks capable of providing a pressure of up to 20 MPa. Flat jack pressures were applied prior to fluid injection in the borehole and were maintained constant throughout testing. The propagation of the hydraulic fractures was monitored by the piezoelectric contact transducers glued onto the rock surface using epoxy and capable of generating compressional and shear waves. The transducer models were Panametric V103-RM and V153-RM with an active element size of 0.5 inch (12.7 mm) diameter for the small size blocks and V102-RM and V152-RM with an active element size of 1.0 inch (25.4 mm) diameter for the large size blocks. A combination of 12 compressional and up to 6 shear wave transducers were used in the experiments. The transducers were integrated into a computer-controlled box; therefore, each

transducer was capable of acting both as a source and as a receiver. Linear Variable Differential Transformers (LVDTs) were placed along the free surface towards which the fracture propagates with the purpose of having additional forms of measurement of the fracture aperture and the fracture width profile as a function of time. A diagram of the experimental set up is shown in Figure A.7. (A_ photograph of a large size and a small size block inside the polyaxial reaction frame during the experiment can be observed in Figure A.8.

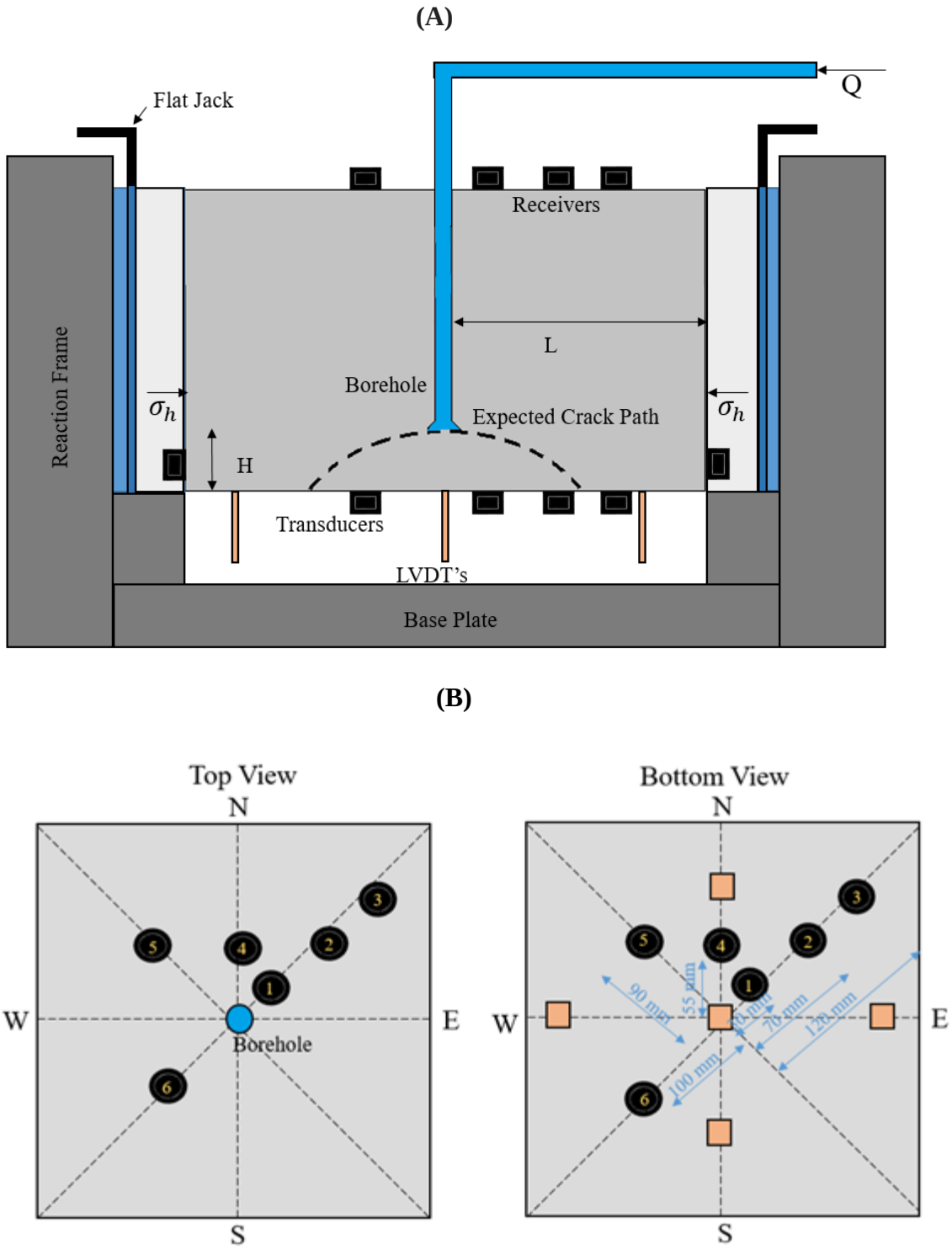

Figure A.7: Diagram of the experimental set up: (A) Side view of the specimen inside the reaction frame, and (B) top and bottom view of one of the specimens with LVDTs and ultrasonic transducers.

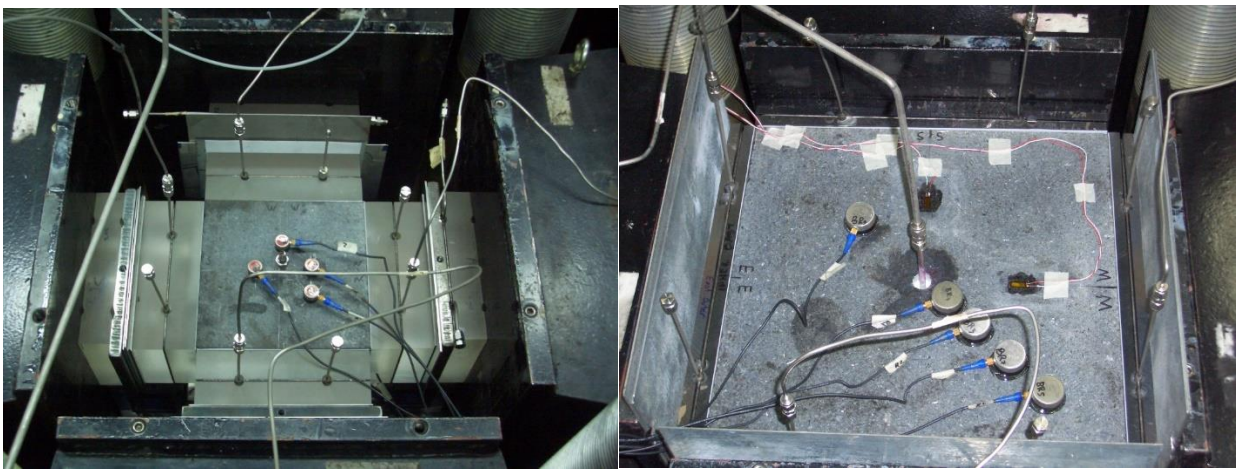

Figure A.8: Photos of the top view of experimental set up: (A) small size block with the side plates and (B) large size block.

As the fluid is injected, the fluid pressure increases until the maximum pressure is reached. The instant when the applied flow rate at the pump was equal to the flow rate into the fracture is defined as the breakdown time. The fracture was allowed to propagate until it daylighted at the free surface or on the sides of the specimen. After that, the fluid injection was stopped and the specimen was unloaded and cut through the borehole into four similar pieces to study the shape of the propagated fracture.

Table A.1: Material Properties

Adelaide Black Granite		
ρ	2870	[kg/m^3]
Permeability	~10^{-20}	[m^2]
K_{IC}	2.5	[MPa$\sqrt{}$m]
Static		
E	102	[GPa]
ν	0.24	
Dynamic		
E	99	[GPa]
ν	0.22	

Injection Fluid		
μ	0.75	Pa·s

Results

Initiation of hydraulic fractures from borehole

Figure A.9 shows the injection pressure and the displacement measured in the central LVDT (aligned with the borehole) and the displacement rate of the LVDT displacement for a large size block. It can be observed that after injection begins, pressure builds up prior to the fracture initiation. After an initial non-linear increase, the pressure increases linearly with time. The slope of the pressure increase over time is proportional to the injection rate and inversely proportional to the compliance of the injection system.

As the pressure increases, the surface displacement is monitored, the surface displacement and the displacement rate graphs have an inflection point, which is interpreted to be the point of fracture. A vertical black line is used to mark the moment the maximum pressure is reached, this moment is also marked by a vertical line in the displacement rate graph. It can be observed that the maximum pressure coincides with the inflection point in the LVDT displacement and the LVDT displacement rate graphs. The pressure required to initiate crack propagation is a function

of the properties of the rock (strength and fracture toughness), the stress field in the vicinity of the borehole, the injection rate, the viscosity of the fluid, and the geometry of the notch carved around the point of injection.

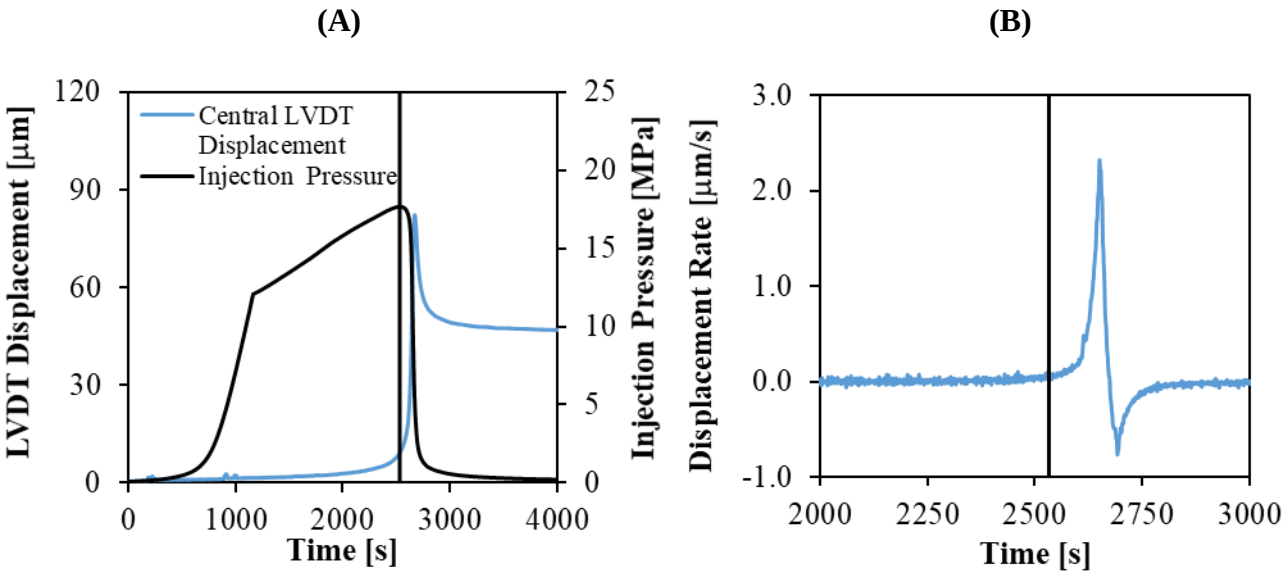

Figure A.9: (A) Injection pressure and central LVDT displacement vs experimental time and (B) displacement rate vs experimental time for a large size block experiment.

Similarly, Figure A.10 shows the injection pressure and the displacement measured in the central LVDT and the displacement rate for a small size block. The moment when the maximum pressure was reached is marked with a vertical line in both the LVDT displacement and displacement rate graphs. The inflection point is interpreted to be the moment of fracture initiation and it is observed that it coincides with the maximum pressure for both small and large blocks. This results show that measurements of the displacement on the free surface using LVDT's can be used to obtain the moment when the maximum pressure occurs.

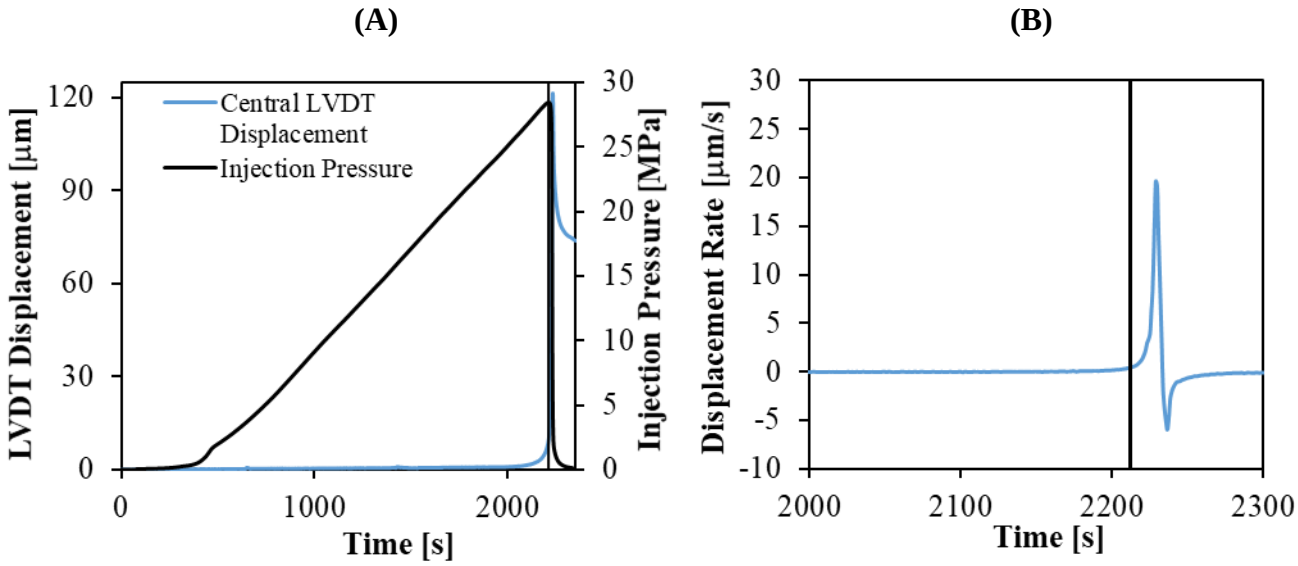

Figure A.10: (A) Injection pressure and central LVDT displacement vs experimental time and (B) displacement rate vs experimental time for a small size block experiment.

Monitoring of fracture width

By compiling the calculated widths at the different scans the width of the fracture is plotted as a function of time at the distance from the borehole where the transducer is placed.

Figure A.11 demonstrates the calculated width compared to the displacement of LVDTs that were placed nearest to the corresponding transducers on the free surface. The LVDTs are placed 100 mm away from the borehole for the experiments performed on large blocks and 50 mm away from the borehole in the experiments performed with small blocks. It can be observed that the fracture width calculated using the ultrasonic monitoring method has similar dependence on experimental time and is of similar magnitude as the LVDT displacement.

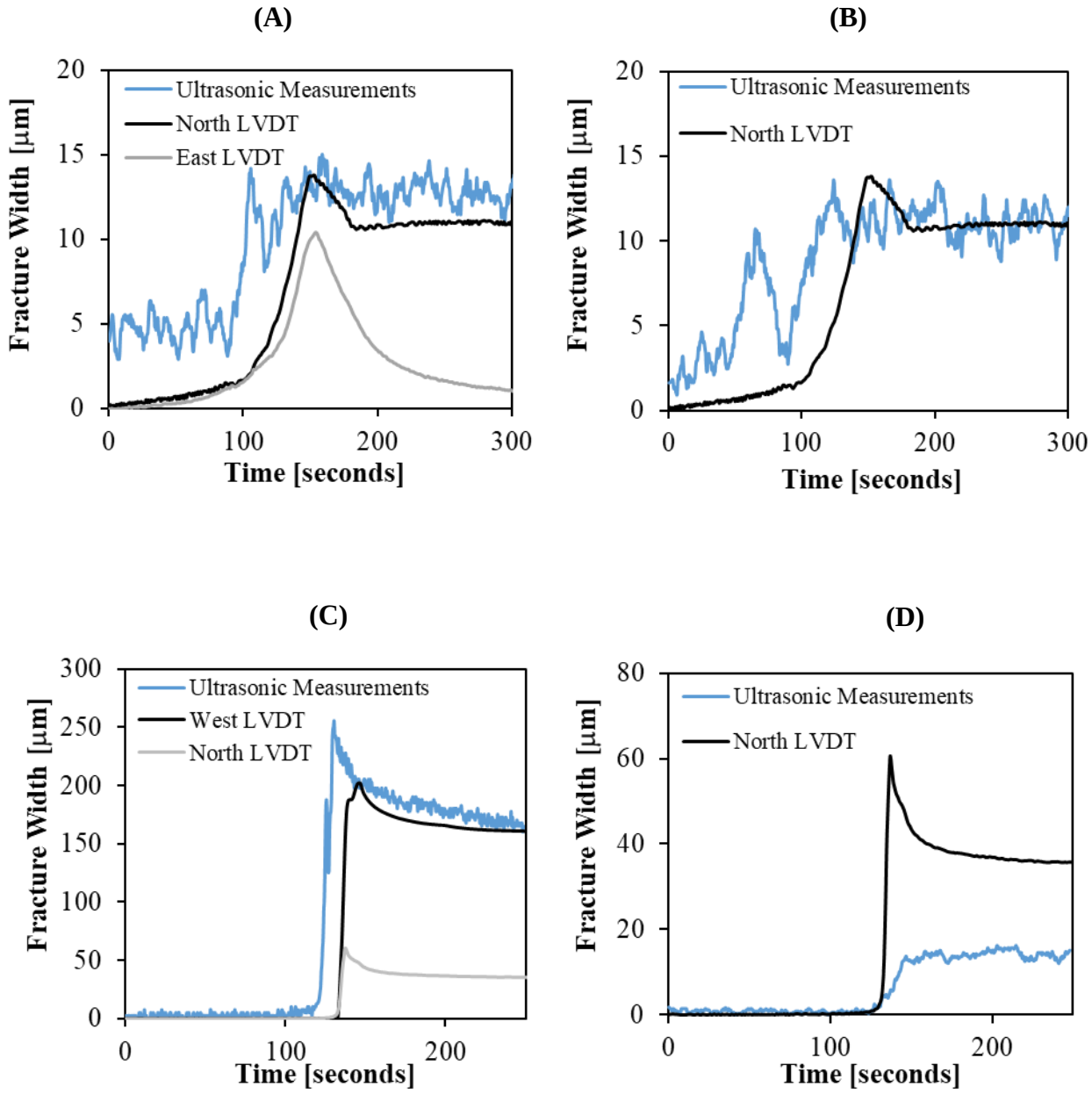

Figure A.11: Fracture width as a function of time calculated in a (A) large size specimen 67 mm from the borehole in the northeast direction (B) a large size specimen 40 mm from the borehole in the north direction (C) small size specimen 50 mm from the borehole in the northwest direction (D) small size specimen 67 mm from the borehole in the north direction.

The LVDTs served the purpose of validating the results obtained from ultrasonic monitoring. It can be observed that in general for both the calculated widths and the measured LVDT displacements that at the end of every experiment there was still some residual aperture

that was less than the maximum width. The residual aperture can be attributed to asperities along the fracture. Note that it was only possible to monitor the width of fractures where the propagating wave was approximately perpendicular to fracture surface.

It can be observed in Figure A.11 (D) that the calculated width is smaller in magnitude than the surface displacement measured by the LVDT. The reason for this is that the ultrasonic transducer and receiver are placed further away from the borehole than the LVDT (67 mm and 50 mm). The width of the fracture decreases as the distance from the borehole increases as it can be observed in figure 15. In contrast, for the remaining tests plotted in figure 10, the ultrasonic transducer and receiver were closer to the borehole than the corresponding LVDT. It can be observed that for all these tests the calculated fracture width is slightly larger than the surface displacement measured at the LVDT. In Figure A.11 (C) the LVDT displacement for the north LVDT is smaller than the calculated width using ultrasonic experiments, this can be explained by the fact that the LVDT is not in the same place where the ultrasonic measurements are taking place and the specimen is composed of a heterogeneous material so the geometry of the fracture can change with location.

Monitoring of fracture depth

The difference domain plots were used to calculate the length and depth of the hydraulic fractures at different distances from the borehole. The depth of the hydraulic fracture can be calculated by analyzing the shear waves that are reflected from the fracture interface. The arrival time of the reflected shear waves is measured at different distances from the borehole. Figure A.12 shows the calculated fracture depth compared to direct measurements of the fracture depth obtained through a post mortem analysis in which the specimen was cut open. A picture of the

specimen after it was cut open after is also shown in Figure 12 so that the fracture can be directly observed.

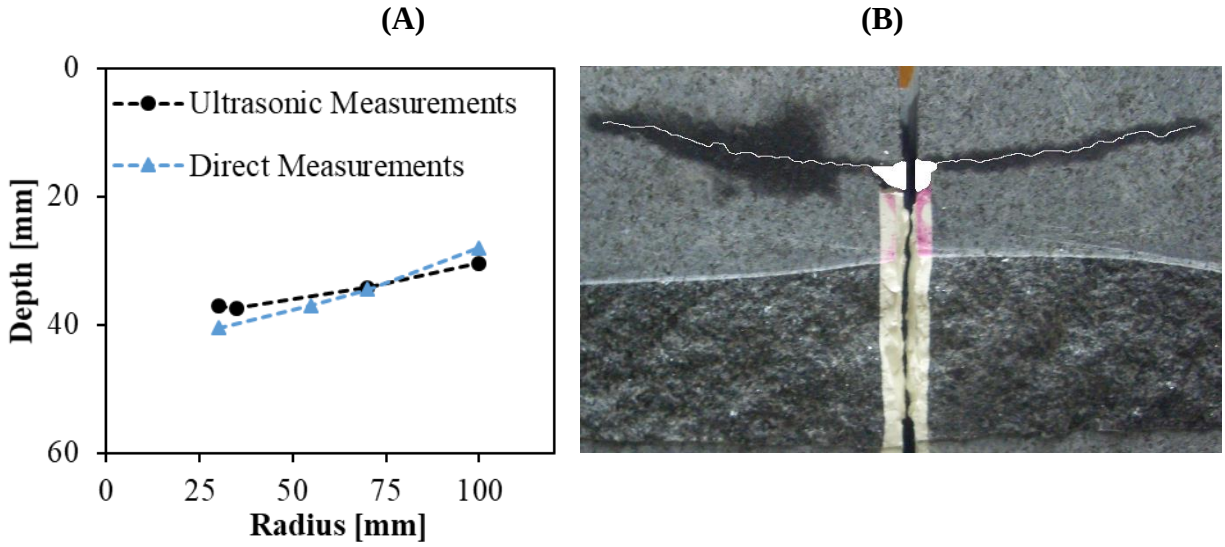

Figure A.12: (A) Length and depth of near-surface fracture from partially reflected S-wave signals for block large size block measured at three different distances from the center of the borehole. (B) The block cut open after the experiment where the fracture can be directly observed.

In the case where transducers on the side of the block are available, it is also possible to calculate the fracture depth by analyzing the wave diffractions that are caused by the fracture tip. The change in arrival time of diffracted waves is related to the change in position of the fracture tip, and by solving the system of equations (A.7) it is possible to calculate the fracture depth and the fracture radius. The configuration where a side transducer was present was used in two different tests with small size blocks. In both cases, the experiment ended shortly after the fracture crossed the line of sight of the second bottom transducer and the side receiver. Therefore, this transducer/receiver pair recorded only the arrival time of diffracted waves when the fracture was detected and no subsequent measurements to measure the change and arrival time were possible. The system of equations was solved for the instant where the fracture is first detected by the second transducer the side receiver pair using the initial arrival time for this

transducer/receiver pair and calculate the depth and radius of the fracture at for this moment. The radius and depth calculated for these two blocks were a radius of 98 mm and a depth of 33 mm and radius of 70 mm and a depth of 18 mm.

Monitoring of fracture length

It is assumed that the fracture has propagated through the line of sight of a transducer pair when these transducers detect dispersion and attenuation of P-waves (which are caused by the propagating hydraulic fracture). The transducer pairs are placed at different distances from the borehole, therefore when the transducer/receiver pair detects the fracture the radius at that moment is the distance from the borehole to the receiver/transducer pair.

The fracture radius was detected at different locations at different moments in time by analyzing the attenuation and dispersion of P-waves. As it will be explained in section 5, the radius calculated using ultrasonic monitoring is compared to the analytical solution for the radius of a penny shaped fracture (Equation A.11). It is expected that the radius for a near surface hydraulic fracture will be smaller and will propagate at a slower rate as a result of the fact that unlike in planar fractures, not all of the fracture propagation is radial. Figure A.13 (A) shows the analytical solution for the radius of a penny shaped hydraulic fracture compared with the radius calculated using ultrasonic measurements along the North-West direction of a large size block. Measurements in the same direction only were used in Figure A.13 (A) because the fracture is not symmetric as a result of the heterogeneities of ABG and the asymmetry in loading conditions so the radius is not necessarily equal at the same distance from the borehole in a different direction. The initial radius (t=0) used is set equal to the notch size plus the borehole radius. It is observed that the radius

predicted by the analytical solution for the radius of a planar fracture grows at a considerable faster rate and reaches a greater value than the radius of a near surface hydraulic fracture.

Figure A.13 (B) shows the expected propagation of a penny shaped hydraulic fracture in a large size block, assuming symmetric propagation. It is predicted that a penny shaped fracture would daylight through the sides of the block at approximately 80 seconds, while the near surface hydraulic experiment lasted approximately 15 minutes. Figure A.13 (C) shows how the near surface fracture advanced in a radial direction throughout the experiment. As it can be observed, the near surface hydraulic fracture propagates at a slower pace in the radial direction compared to a penny shaped fracture. This discrepancy is expected because in a planar fracture, by definition, all the propagation occurs in a radial direction. In contrast, near surface hydraulic fractures curve towards the surface, adding a component of propagation out of the plane and decreasing the amount of radial fracture growth.

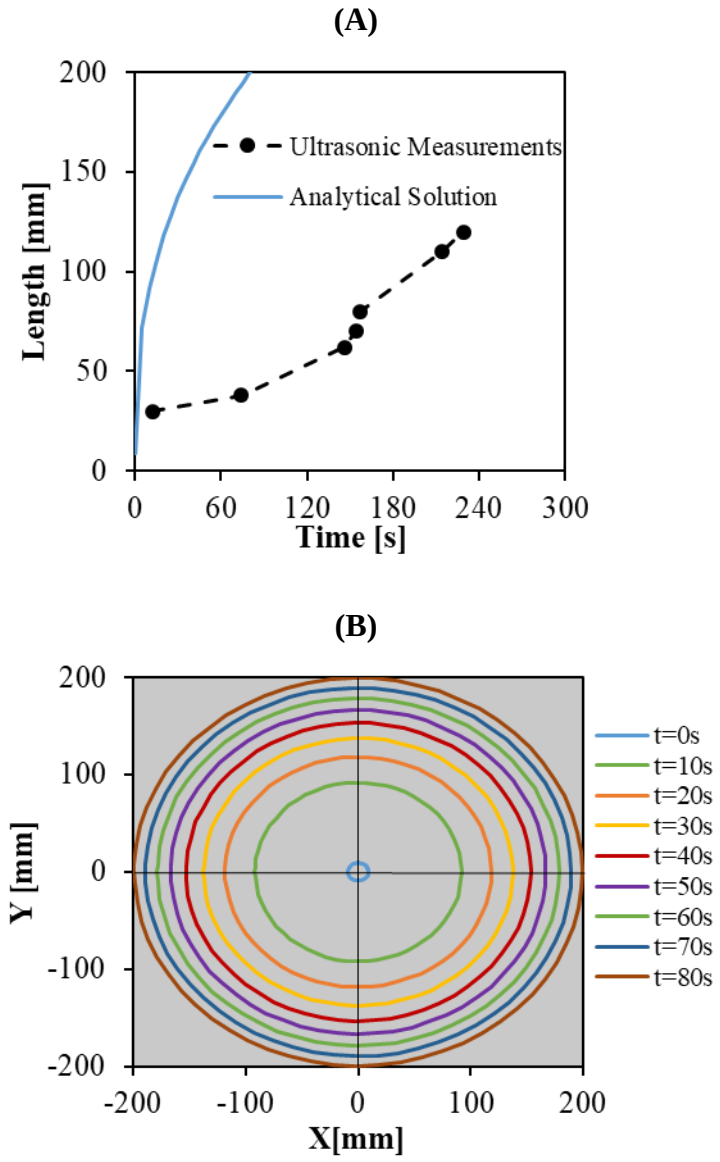

Figure A.13: (A)Length vs Time from ultrasonic measurements a large size block plotted along with the analytical solution for the radius as a function of time for a penny-shaped fracture (B) A large size block drawn to scale showing the predicted radius for a penny shaped hydraulic fractures at different moments in time. The radius at the beginning of the experiment (t=0s) is equal to the notch size plus the borehole radius. (C) A diagram of a large size block drawn to scale showing the locations of the transducer/receiver pairs and the evolution of the fracture. The blue line represents the predicted radius for a penny shaped fracture at that moment in time (as long as it is predicted to be inside the block). The white circles represent a transducer/receiver pair that has not yet detected the fracture at that location. The green circles represent a transducer/receiver pair for which the fracture has been detected at that location. The red circles represent a transducer/receiver pair that is detecting the fracture for the first time at that location at the given moment in time.

Figure A.13 (cont.)

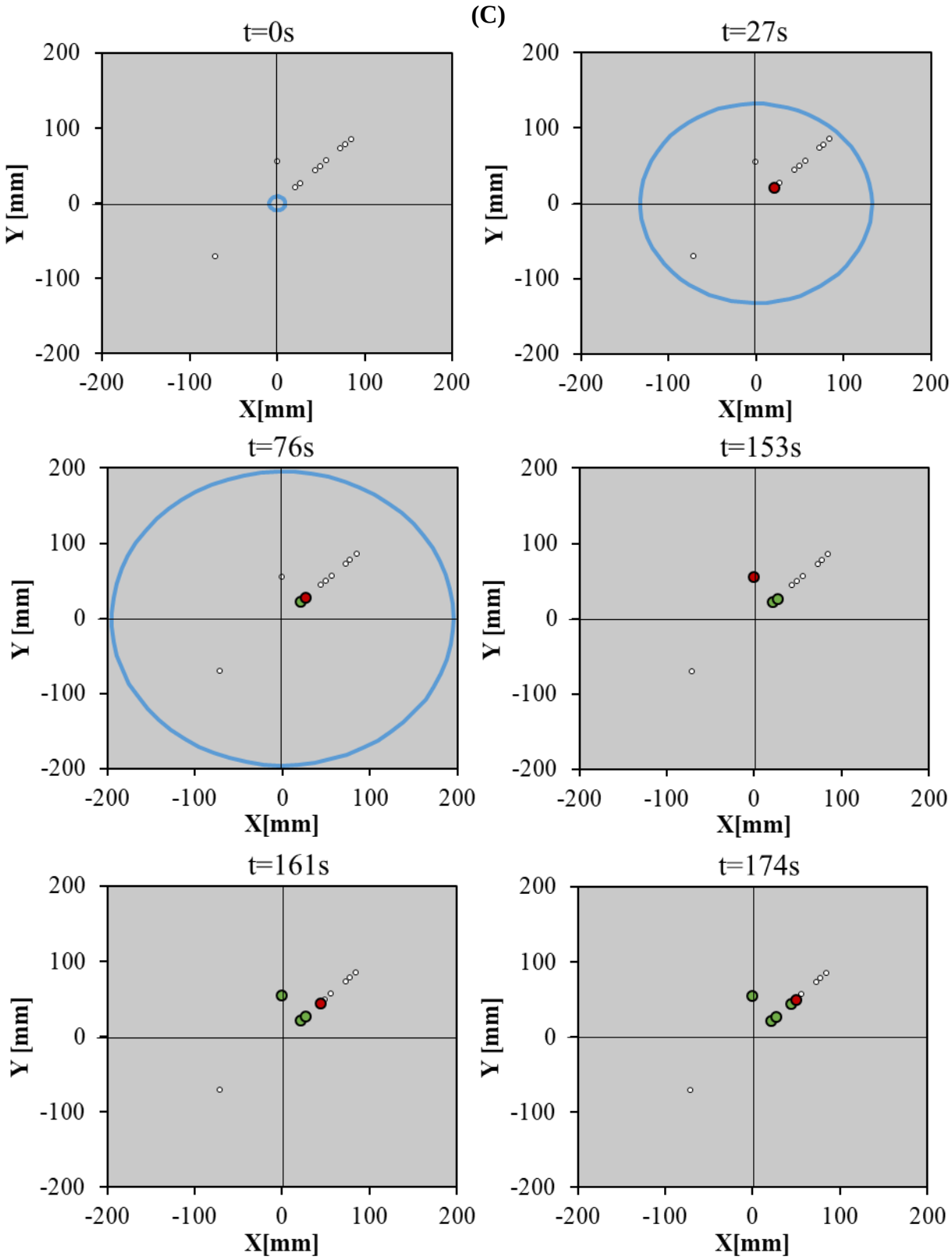

Figure A.13 (cont.)

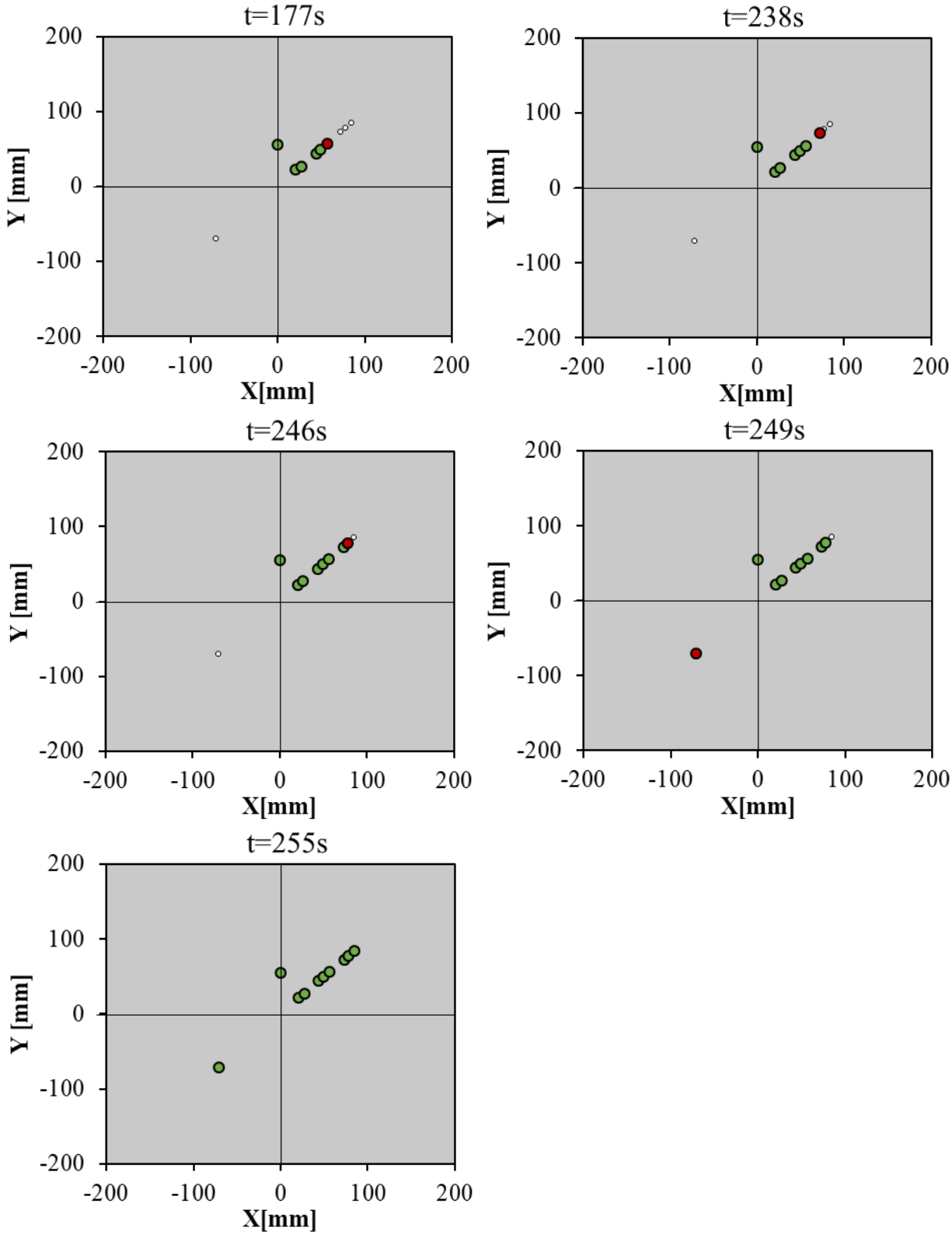

Discussion

It was observed that the saucer pan shape of the fractures in ABG was not symmetric as predicted in models for LEFM materials in Zhang et al (2002) and Bunger and Detournay (2005). The asymmetry of the fractures is caused by the heterogeneity of the rock and slight asymmetry in loading conditions. Preexisting defects or imperfections in the ABG matrix can cause the fracture to propagate in a random and asymmetric manner. An example of this can be seen in Figure 13.

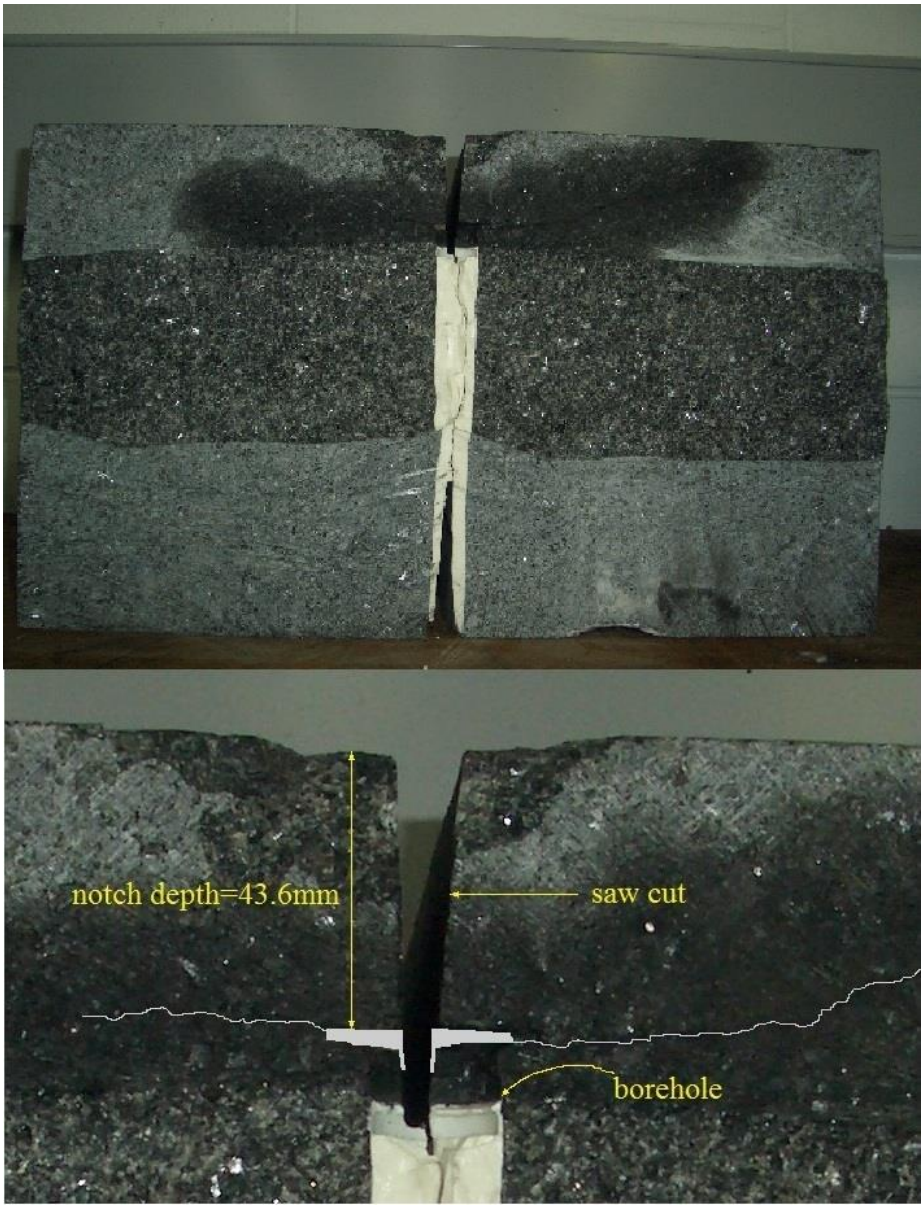

Figure A.14: Photo of a small size block that was cut open after the experiment for further analysis.

Figure A.15 shows the calculated fracture width as a function of time at different distances from the borehole. The points were the width was calculated are along radial line from the borehole because the hydraulic fractures in the ABG were found to be generally asymmetric so the purpose was to compare the fracture width on the same side. There was an error with the ultrasonic

measurements for the transducer placed at 70 mm from the borehole and data was not recorded from 125 to 160 seconds. It can be observed that the way the fracture width evolves over time is similar for the three distances but the width has a greater magnitude closer to the borehole. This can be explained by the fact that near the borehole there is less confinement so the local stiffness is reduced. In addition, near the borehole the pore pressure is greater and it decreases along the fracture further away from it.

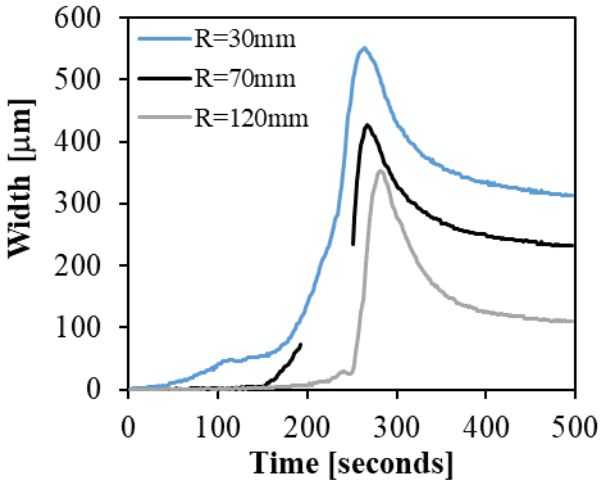

Figure A.15: Fracture width measured at 30, 70, and 120 mm from the borehole in the same direction in a large size specimen.

Comparison with an Analytical Model for a Penny-Shaped Fracture

The curved nature of near surface hydraulic fractures poses additional challenges for their characterization. As a result, unlike planar or penny-shaped hydraulic fractures, there is no existing analytical solution to describe the width and radius of a near surface hydraulic fracture as a function

of time. The observed results measured for the experiments with near surface hydraulic fractures are compared with a model describing the behavior of planar fractures. Detorunay (2016) provides a review of the mechanics of hydraulic fractures and Lecampion (2016) shows a good match for experimental and predicted results for planar hydraulic fractures in low permeable materials. The analytical solution for penny-shaped hydraulic fractures is derived from a mathematical model that assumes that the injection fluid is incompressible, that the leak-off of fluid from the fracture into the rock is negligible and that the fracture volume is a function of the pressure and the radius (Abé *et al*. 1976). All these assumptions are reasonable for the experimental set up and material that was used (ABG). Since the shape of near surface and penny-shaped hydraulic fractures is different, the analytical solution was used with caution, only with the purpose of comparison and in order to understand if the results were in the expected range of magnitudes.

The width of a planar fracture as a function of time is given by:

$$h = \frac{3^{0.2}}{2^{0.6} \cdot \pi^{0.2}} \cdot \left(\frac{\left(\sqrt{\frac{32}{\pi}} \cdot K_{IC} \right)^4 Q_o t}{E'^4} \right)^{0.2} \cdot \sqrt{1 - \frac{R^2}{100 \cdot t^{0.8}}} \qquad \text{(A.10)}$$

The radius of a planar fracture as a function of time is given by the following equation:

$$R = R_0 + \left(\frac{3}{2^{0.5} \cdot \pi} \right)^{0.4} \cdot \left(\frac{E' Q_o t}{\left(\sqrt{\frac{32}{\pi}} \cdot K_{IC} \right)} \right)^{0.4} \tag{A.11}$$

The analytical solution for the width of a planar fracture was compared with the measured results in experiments for a small and a large block, where the fracture was approximately planar (of low curvature), as a result of the high applied lateral stress, 28.44 MPa for the small block and 19.60 MPa for the large block. The time of fracture initiation was determined using the displacement measurements from the central LVDT (aligned with the borehole) as described in section 4.1. As expected, the measured results are slightly different than the analytical solution since the hydraulic fractures in the experiments were saucer pan shaped and not planar; the purpose of this exercise was to serve as a checking method and determine the feasibility of the calculated results. Figure 16 compares width calculated using ultrasonic measurements of the near surface hydraulic fracture propagated in large size block to the analytical solution for a planar fracture:

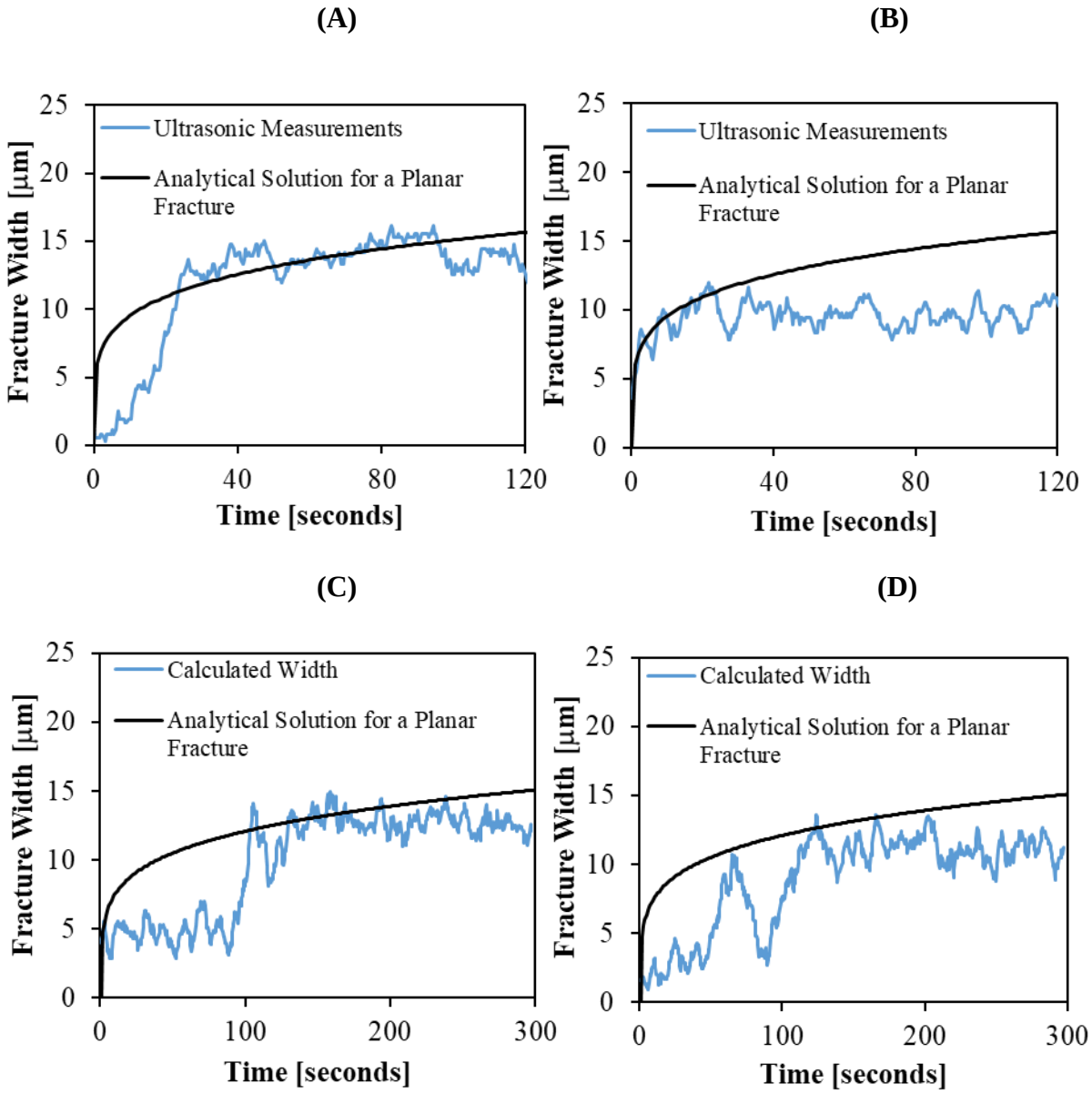

Figure A.16: Calculated width compared to the analytical solution for the width of a planar hydraulic fracture. The data is from tests (A) for a small size specimen measured at 67 mm from the borehole (B) for a small size specimen measured at 50 mm form the borehole (C) for a large size specimen measured at 40 mm from the borehole (D) for a large size specimen measured at 40mm form the borehole.

It can be observed that the calculated width and the analytical solution for the width of a near surface hydraulic fracture are in the same range and in general agreement, this shows that the fracture width calculated using ultrasonic measurements is reasonable as the magnitude of the

results is as expected. It is observed that the curve for the analytical solution of the fracture width is smoother than that obtained by the ultrasonic measurements, this phenomena can be caused by variation of the ultrasonic signal such as background and heterogeneities in the rock.

Figure A.13 compares the calculated radius using ultrasonic measurements of the near surface hydraulic fracture compared to the analytical solution for a planar fracture. The initial radius of the fracture (R_0) was assumed to be half of the diameter of the borehole plus the notch length.

As expected, the results do not match as a result of the curvature of the near surface hydraulic fracture. The radius of the penny-shaped fracture is expected to be larger as it is observed in Figure A.13. The reason is that while all the fracture propagation in a penny-shaped fracture is radial, near surface fractures also propagate towards the surface. Therefore, less of the propagation of a near surface hydraulic fracture is in the radial direction, resulting in a smaller radius. However, it can be observed that the results are in a similar range of magnitude which demonstrates that the calculated parameters using ultrasonic monitoring are within reasonable limits.

Conclusion

It is possible to obtain reliable information of a propagating hydraulic fracture in rock by analyzing the interaction of the fracture with ultrasonic waves, even when the hydraulic fracture is curving towards a free surface. The interactions between the hydraulic fracture and the ultrasonic waves can be used to calculate different geometric parameters of the fracture such as the width, depth and length. The results obtained for the width and depth where in the expected range and found to be in reasonable agreement when compared to LVDT displacement measurements on the

free surface and the analytical solution for penny shaped hydraulic fractures. It was observed that the radius of near surface is smaller and grows at a smaller rate than that of penny shaped fractures, as it was expected. In addition, LVDT displacement measurements aligned with the borehole on the free surface were used to detect the moment of fracture initiation, which was observed to happen when the maximum injection was reached both for small and large size blocks. The results can be used to better understand near surface hydraulic fractures in rock and the challenges that their curvature poses in order to develop more accurate models to describe them which are currently unavailable. Models for near surface hydraulic fractures in rock would be significantly helpful in advancing processes of application of near surface hydraulic fractures and better understanding certain geophysical processes.